

4D Monte Carlo Based Patient Dose Reconstruction Incorporating Surface Motion Measurements

by

Meaghan Shiha

A thesis submitted to the Faculty of Graduate and Postdoctoral Affairs in partial fulfillment of the requirements for the degree of

Master of Science

in

Physics (Medical Physics)

Ottawa-Carleton Institute for Physics
Department of Physics
Carleton University
Ottawa, Ontario

© 2021 Meaghan Shiha

Abstract

A framework was developed to assess the impact of respiratory motion on the dose delivered during radiotherapy using a previously validated 4D Monte Carlo-based dose reconstruction tool, 4Ddefdosxyznrc. As a surrogate for tumour motion, abdominal surface motion measurements were recorded during patient treatments using the RADPOS system. Motion traces, treatment log files and deformation vectors representing each patient's respiratory motion were used as inputs to the 4D dose reconstructions. Motion measurements were performed for 3 patients undergoing radiation therapy for non-small cell lung cancer, totalling 12 fractions. No statistically significant inter-fractional differences in 4D reconstructed dose metrics were found. A maximum difference of 2.0% in the GTV D98% was found between 4D calculations and the treatment planning system. This result is consistent with small abdominal displacements of 5.5 ± 1.4 mm, 5.4 ± 0.4 mm, and 0.40 ± 0.03 mm, respectively, observed for these 3 patients during treatments.

Acknowledgements

First and foremost, I would like to thank my supervisors, Dr. Emily Heath, and Dr. Joanna E. Cygler. I am incredibly grateful for the mentoring they have provided me throughout this project. Their thoughtful feedback over the last two years has been inestimable and has been critical in my development as a researcher.

I would also like to show appreciation to Sara Gholampourkashi, for the helpful discussions we have had and the advice she has given me with regards to this project.

Thank you to Dr. Robert MacRae for contouring the patient CT scans.

I want to acknowledge staff members at TOHCC including Steve Andrusyk and Chris Lambert as well as the radiation therapists working on Unit 9 for their patience and flexibility with regards to the collection of patient measurements during treatments.

I also want to thank Dal Granville for extracting the machine log files for each treatment fraction and Cathy Rose for taking the time to provide technical assistance for the treatment planning systems.

Finally, I would like to thank my family and friends for their continuing encouragement and unwavering support over the course of this project.

I also acknowledge the support of the Natural Sciences and Engineering Research Council of Canada (NSERC).

Ethics Statement

Ethics approval was provided for this project from the Carleton University Research Ethics Board-A (CUREB-B). The ethics protocol clearance ID is project # 110875.

Approval for this project was also granted from the Ottawa Hospital REB (OHSN-REB), protocol #20190030-01H. Written informed consent was collected from all patients that took part in this study. Data was collected and anonymized in accordance with the ethics protocols established by the Ottawa Hospital and Carleton University.

Statement of Originality

This thesis details work done by the author while completing their Master's in Physics (Medical) at Carleton University. The supervisors for this work, Dr. Emily Heath and Dr. Joanna E. Cygler provided their input throughout the project. Measurements were taken under the supervision of Dr. Joanna E. Cygler.

Parts of this work were presented in the form of poster presentations at two conferences:

Shiha M, Cygler J.E, MacRae R, Heath E. 4D Monte Carlo Assessment of the Impact of Inter- and Intra-Fractional Respiratory Motion Variation on Delivered Dose. Poster presented at: 2021 AAPM Meeting; July 25-29, 2021.

Shiha M, Cygler J.E, MacRae R, Gholampourkashi S, Heath E. 4D Monte Carlo Based Patient-Specific Dose Reconstruction Incorporating Surface Motion Measurements. Poster presented at: 2020 Joint AAPM/COMP Meeting; July 12-16, 2020.

Glossary

3D CRT	Three-dimensional conformal radiation therapy
A/P	Anterior/posterior
ABC	Active breathing control
CBCT	Cone-beam CT
CCC	Collapsed cone convolution
CCD	Charge-coupled device
CM	Component module
CPU	Central processing unit
CT	Computed tomography
CTV	Clinical tumour volume
DAO	Direct aperture optimization
DIBH	Deep-inspiration breath hold
DICOM	Digital imaging and communication in medicine
DVH	Dose volume histogram
ECUT	Electron cut-off energy
EGS	Electron gamma shower
Gamma index	Dose evaluation method that combines the distance to agreement and dose difference evaluations.
$\Gamma(r_m) = \sqrt{\frac{r^2(r_m, r_c)}{d_M^2} + \frac{\delta^2(r_m, r_c)}{D_M^2}}$	
GTV	Gross tumour volume

GTVn	Gross tumour volume nodes
HU	Hounsfield units
IMRT	Intensity modulated radiation therapy
ITV	Internal tumour volume
LBTE	Linear Boltzmann transport equation
Linac	Linear accelerator
L/R	Left/right
MFP	Mean free path
MIP	Maximum intensity projection
MLC	Multileaf collimator
MOSFET	Metal-oxide-semiconductor field-effect transistor
MU	Monitor unit
NRC	National Research Council
NSCLC	Non-small cell lung cancer
OAR	Organ at risk
PCUT	Photon cut-off energy
PTV	Planning tumour volume
S/I	Superior/inferior
SBRT	Stereotactic body radiotherapy
SCLC	Small cell lung cancer
SSD	Source to surface distance
TOHCC	The Ottawa Hospital Cancer Centre
TPS	Treatment planning system

VMAT	Volumetric modulated arc therapy
VMC	Voxel Monte Carlo
VSM	Virtual source model
XVMC	X-ray voxel Monte Carlo

Table of Contents

Abstract.....	i
Acknowledgements	ii
Ethics Statement.....	iv
Statement of Originality	v
Glossary	vi
Table of Contents	ix
List of Tables	xiii
List of Figures.....	xv
Chapter 1: Introduction.....	1
1.1 Lung cancer overview.....	1
1.2 Radiation therapy fundamentals	1
1.3 Linear accelerators.....	3
1.4 Radiation treatment process.....	6
1.5 Treatment delivery techniques.....	10
1.5.1 3D conformal radiation therapy (3D CRT)	10
1.5.2 Intensity modulated radiation therapy (IMRT)	11
1.5.3 Volumetric modulated arc therapy (VMAT).....	12
1.6 Motion compensation techniques	13
1.7 Motivation.....	14
1.8 Research goal.....	16
1.9 Thesis organization.....	17
Chapter 2: Respiratory motion during radiation therapy	18
2.1 Respiratory motion characteristics.....	18
2.2 Correlation between internal and external respiratory motion	20

2.3	Respiratory monitoring devices	21
2.3.1	Implanted fiducials	22
2.3.2	Tumour motion surrogates	22
2.3.3	Electromagnetic trackers	24
2.3.4	RADPOS 4D position sensor	25
2.4	Motion compensation techniques	27
2.4.1	Treatment planning techniques.....	27
2.4.2	Treatment delivery techniques	28
2.4.2.1	Respiratory gating.....	28
2.4.2.2	Breath-hold techniques	29
2.4.2.3	Abdominal compression	30
2.4.2.4	Real-time tumour tracking	31
Chapter 3: Dose Calculation Algorithms	33	
3.1	Overview of dose calculation algorithms	33
3.2	Monte Carlo Dose simulations	36
3.2.1	Monte Carlo fundamentals	36
3.2.2	XVMC Monte Carlo code	38
3.3	EGSnrc Monte Carlo code.....	39
3.3.1	Accelerator modelling with BEAMnrc	40
3.3.2	Dose calculations with DOSXYZnrc	41
3.4	Monaco TPS	42
3.5	4D dose calculation methods	43
3.5.1	Dose-mapping methods	43
3.5.2	Energy mapping and voxel-warping methods	45
3.6	4D dose reconstruction methods.....	46
3.7	The 4Ddefdosxyznrc reconstruction tool.....	50

Chapter 4: Application of 4D dose reconstruction to patients.....	53
4.1 Description of patient group	53
4.2 4D reconstruction framework	57
4.2.1 4D-CT Acquisition	58
4.2.2 Image Registration.....	59
4.2.3 Tumour volume and OAR contouring.....	60
4.2.4 Patient measurement setup	61
4.2.5 4Ddefdosxyznrc simulation parameters and input file generation.....	63
4.2.6 Dose metric comparison	70
Chapter 5: Results.....	72
5.1 Patient motion characteristics	72
5.1.1 Patient 1	72
5.1.2 Patient 2	76
5.1.3 Patient 3	79
5.2 Motion trace normalization.....	82
5.3 Comparison of DOSXYZnrc and Monaco TPS	86
5.3.1 Comparison of treatment plan dose calculations.....	86
5.3.2 Verification of Beam model	92
5.4 4D dose reconstructions.....	96
5.4.1 Patient 1	96
5.4.2 Patient 2	100
Chapter 6: Discussion and Conclusions	104
6.1 Discussion.....	104
6.2 Future work.....	109
6.3 Conclusion	110

Appendix.....	112
Bibliography	118

List of Tables

Table 4.1: Summary of treatment parameters for the patients recruited in this study. The tumour volumes cited are those which were contoured by a physician on the AVG-CT scan	53
Table 4.2: Calibration curve used to convert CT numbers in HU to mass density in g/cm ³	64
Table 4.3: Material composition and density data ^{145,146} used to define the dose calculation geometry	65
Table 4.4: Summary of Monte Carlo calculations completed in this work	65
Table 5.1: Patient 1, 3D position characteristics. The average 3D peak-peak displacement and average minimum position is presented, with the standard deviation, for each fraction	75
Table 5.2: 3D and A/P position characteristics measured for Patient 2. The average 3D peak-peak displacement and average minimum position are presented, with the standard deviation, for each fraction	79
Table 5.3: Comparison of dose metrics calculated by the TPS and with DOSXYZnrc on the AVG-CT. Volume dose metrics are scaled to the dose values per fraction, shown in brackets is the total treatment dose	91
Table 5.4: Comparison of dose metrics for the GTV, heart and esophagus. The Monaco and DOSXYZnrc calculations of the plan are compared to the 4D reconstructions, with uncertainties between 0.9% and 1.0%, for Patient 1, using the 3D norm	99
Table 5.5: Patient 2, 4D reconstructions using 3D norm. Average statistical uncertainty was 0.7% for the 4D reconstructions	102

Table 5.6: Patient 2, 4D reconstructions using AP norm. The average statistical uncertainty was 0.7% for the 4D reconstructions.	103
---	-----

List of Figures

Figure 1.1: Diagram of a medical linear accelerator showing the waveguide, target and collimation systems which are shaping the photon beam (shown in orange). Figure modified from Galvin and De Neve ⁴ , reprinted with permission from Wolters Kluwer Health Inc.....	3
Figure 1.2: Example of an MLC collimated treatment field. Figure reprinted from Bedford et al ⁵ licensed under CC BY 3.0	4
.....	5
Figure 1.3: Treatment room layout, the collimator and gantry rotation axis and couch shift directions are shown in red.	5
Figure 1.4: Example of workflow for the treatment of lung cancer at TOHCC.	7
Figure 1.5: The GTV, CTV, ITV and PTV contours as described in ICRU reports 50 and 62. ^{6,7}	8
Figure 1.6: Dose volume histogram generated by a treatment prescribed to deliver 6000 cGy to 95% of the PTV. The doses to the nearby OAR are also shown.	9
Figure 1.7: Comparison of beam arrangements for a 3D CRT (left) and VMAT treatment (right). Figure modified from Rauschenbach et al ⁹ , licensed under CC BY 3.0.	11
Figure 1.8: Differences in treatment fields used and dose distributions achieved using IMRT and VMAT treatment techniques. The threshold for the colour wash is 18 Gy (shown in dark blue). As demonstrated by the lack of dose above 18 Gy, the VMAT dose distribution demonstrates sparing of the contralateral lung. Figure reprinted from Storey et al. ¹⁴ licensed under CC BY 4.0	13

Figure 1.9: Depiction of the interplay between the motion of an organ represented by the star and the movement of the MLC. In this case the MLC move to the left and right and the organ moves in the vertical direction. The two stars represent the organ in two different phases of respiration. In the case of the filled star, no primary dose is delivered between t1 and t4. On the other hand, if the organ was in a respiratory phase represented by the open star, it would have received the full primary dose. While these two cases are exemplary of an extreme, they are shown to illustrate the possible implications of the interplay effect. Figure reproduced from Bortfeld et al. by permission of IOP Publishing.¹⁷ All rights reserved. 16

Figure 2.1: RADPOS system configuration as described by Cherpak et al.⁵⁷, reprinted with permission. 26

Figure 2.2: Comparison of the Bodyfix system (left) and the abdominal compression plate (right) used in the study by Han et al, reprinted with permission.⁷⁷ 31

Figure 3.1: Illustration of the components to be simulated in a dose calculation. The position of the jaws and MLC will vary for each patient and treatment type and are therefore considered to be patient dependent. Figure adapted from Chetty et al.⁸⁶, licensed under CC BY 3.0..... 33

Figure 3.2: Illustration of dose accumulation methods. Figures reprinted with permission from Chetty et al. ¹²³ 45

Figure 3.3: Flowchart illustrating the steps of the 4Ddefdosxyznrc reconstruction. Redrawn from Gholampourkashi.¹⁴¹ 51

Figure 4.1: GTV contour of Patient 1 outlined in pink, as seen on the average-CT image at the location of the treatment isocenter. 54

Figure 4.2: Tumor and node contours of Patient 2 in blue and pink respectively on the average-CT image at the location of the treatment isocenter.	55
Figure 4.3: The treated lymph nodes and contoured tumor volume for Patient 3, outlined in pink and blue respectively, on the average-CT image.....	55
.....	56
Figure 4.4: Lateral view of Patient 3, with tumor outlined in blue and location of the abdominal compression board, which minimizes patient motion during treatment, indicated by red arrow.	56
Figure 4.5: Outline of the 4D reconstruction framework. Steps in blue are those that would normally occur in the course of a patient's treatment, steps directly involving patients are filled with a darker hue. The steps outlined in orange are additional steps required for the 4D reconstruction.....	57
Figure 4.6: Example of deformation vectors generated for Patient 2 using the deformable multipass registration. The color wash indicates the magnitude of motion, the brightest areas denote larger magnitudes of motion, and the arrows indicate the direction of motion.	60
Figure 4.7: Schematic drawing of patient RADPOS measurement setup.	62
Figure 4.8: Patient setup without placement of RADPOS sensor. The hexapod frame is located at slot 'F'.....	62
Figure 4.9: On the left is a slice from the exhale phase CT of Patient 2, on the right is the same slice from the inhale phase. The change of the position, along the A/P direction, of the fiducial circled in red is measured and used to normalize the patient motion measured with RADPOS.....	69

Figure 5.1: Patient 1 motion measurements for 5 treatment fractions, labeled as Fx *, where * represents the fraction number. The fractions showing the largest position variation are labeled for the L/R and S/I positions.	72
Figure 5.2: Measured 3D position of the abdominal RADPOS sensor during each of the 5 fractions measured for Patient 1. Inter-fractional differences in minimum(exhale) position up to 46 mm are observed between fractions.....	75
Figure 5.3: Patient 2 motion measurements for 5 treatment fractions. The S/I traces are labeled where there are notable position variations. Changes in position from the first fraction up to 11 cm are noted in the S/I direction.	76
Figure 5.4: Measured 3D position of the abdominal RADPOS sensor during each of the 5 fractions measured for Patient 2. Inter-fractional differences in average minimum position of up to 29 mm are observed between fractions.	77
Figure 5.5: Measured A/P position of the abdominal RADPOS sensor during each of the 5 fractions measured for Patient 2. The average peak-peak displacement of all fractions was measured to be 10.0 ± 1.2 mm.	78
Figure 5.6: Motion components measured for all fractions for Patient 3, treated with abdominal compression. The fractions are labeled for the L/R and S/I position where notable position variations are observed.	80
Figure 5.7: A) Patient 3 ‘R’ position traces. B) Example of a 4D reconstructed dose distribution for Patient 3. The minimum threshold of the colorwash is set to 1 Gy, all doses above 20 Gy are shown in red. In such a treatment, the maximum dose would not typically exceed 2.5 Gy	81

Figure 5.8: Example of the normalization of a single 3D motion trace, Fx 2. In the upper plot is the 3D position measured during treatment. The lower graph shows the same trace after baseline adjustment and normalization to the peak-peak displacement observed during the first treatment fraction	83
Figure 5.9 Normalized motion traces for all fractions for Patient 1 using the 3D norm. Traces were adjusted to their individual baseline and normalized to the peak-peak displacement observed during the first treatment fraction.....	84
Figure 5.10: Demonstration of the different normalization schemes used for Patient 2. A) Using the 3D displacement, all motion traces were normalized to the peak-peak displacement measured during the first treatment fraction (3D norm). B) The A/P position traces were normalized to the motion amplitude measured from 4D-CT images (AP norm).	85
Figure 5.11: Isodose lines shown at isocenter for the prescription plan calculated on the AVG-CT, for Patient 1 calculated in Monaco (left) and DOSXYZnrc (right). Isodoses are given as a percentage of the prescription dose of 2 Gy. The GTV is shown outlined in blue.....	87
Figure 5.12: The upper plot shows a comparison of the DVH for the OAR, and GTV as calculated in Monaco (solid line) and DOSXYZnrc (dotted line) on the AVG-CT for Patient 1. The lower plot presents a detailed view of the differences in the DVHs for the tumour volumes between Monaco (solid line) and DOSXYZnrc (dashed line).....	88
Figure 5.13: Isodose lines shown at isocenter for the prescription plan of Patient 2 calculated on the AVG-CT in Monaco (left) and DOSXYZnrc (right). Isodoses are given	

as a percentage of the prescription dose of 2 Gy. The GTV and GTVn are shown outlined in blue.....	89
Figure 5.14: The upper plot shows a comparison of the DVH for the OAR, and GTV as calculated in Monaco (solid line) and DOSXYZnrc (dotted line) on the AVG-CT for Patient 2. The lower plot presents a detailed view of the differences in the DVHs for the tumour volumes between Monaco (solid line) and DOSXYZnrc (dashed line).....	90
Figure 5.15: MLC opening width frequency in clinical patient plans. The openings are calculated at the treatment isocenter.	92
Figure 5.16: Comparison of profiles from measurements, DOSXYZnrc and Monaco in the cross-line direction (patient L/R) at depths of 1.6 cm (A), 5 cm (B) and 10 cm (C). The DOSXYZnrc and TPS simulations were completed with a 0.5% uncertainty.	94
Figure 5.17: Comparison of profiles from measurements, DOSXYZnrc and Monaco in the in-line direction (patient S/I) at depths of 1.6 cm (A), 5 cm (B) and 10 cm (C). The DOSXYZnrc and TPS simulations were completed with a 0.5% uncertainty.	95
Figure 5.18: Isodose distributions calculated with the 4D reconstruction (accumulated on the exhale-CT) for Fx1 (right) compared to the DOSXYZnrc simulation on the exhale-CT (left), for Patient 1.....	96
Figure 5.19: In A, DVHs for GTV, esophagus and heart are shown for Patient 1. The Monaco and DOSXYZnrc calculations of the plan on the exhale phase are compared to the 4D reconstructions for each fraction (3D norm). The 4D reconstructions are labeled by their fraction number (ex. Fx 1). In B, a detailed view of the DVH for the GTV is shown.....	98

Figure 5.20: Isodose distributions for Patient 2, calculated with the 4D reconstruction for Fx1 (right) using the 3D norm compared to the DOSXYZnrc simulation on the exhale-CT (left). 100

Figure 5.21: In A, DVHs for GTV, esophagus and heart are shown for Patient 2. The Monaco and DOSXYZnrc calculations of the plan on the exhale phase are compared to the 4D reconstructions for each fraction. Reconstructions using the 3D norm are shown with the round marker and A/P norm are shown with the star. The 4D reconstructions are labeled by their fraction number (ex. Fx1). In B, a detailed view of the DVH for the GTV is shown. 101

Chapter 1: Introduction

1.1 Lung cancer overview

Currently, cancer is the leading cause of death for Canadians.¹ An estimated 225 800 Canadians were diagnosed with the disease in 2020.¹ Overall, the most commonly diagnosed cancer is lung cancer, projected to affect nearly 30 000 Canadians in 2020.¹ While overall the five year net survival from cancer has increased to about 63%, survival from lung cancer remains lower at about 19%.² In fact, lung cancer presently accounts for about one-quarter of cancer deaths.³ Lung cancer can occur in the cells of the lungs or the bronchus. There are two main types: small cell lung cancer (SCLC) and non-small cell lung cancer (NSCLC). The large majority of lung cancers are diagnosed as NSCLC, which is further divided into 3 types: adenocarcinoma, squamous cell carcinoma, and large cell carcinoma.

1.2 Radiation therapy fundamentals

Lung cancer treatment options primarily include surgery, radiation therapy and chemotherapy. While surgery offers a greater chance of disease management, few patients are generally eligible for such treatments. Radiation therapy offers the possibility of both curative treatment and palliative care for patients who are unable to undergo surgery.³ In radiation therapy treatments, the goal is to deliver the prescription dose to the tumour while sparing the maximal amount of healthy tissue. In external beam radiation therapy, the patient is irradiated using an external source of photons, electrons, protons, or heavy ions. In the case of photon beams, typical energies used are between 4 and 18 MeV, with 6 MV being the preferred energy for treatment of lung tumours. Energy is

transferred from the photons to the medium during ionization events resulting from the interactions of the photons with the atoms in the medium. Cancer cells are killed, either directly or indirectly, by the interactions of the ionizing radiation in the target tissue. The dose delivered to the tumour is specified in terms of the energy absorbed per unit of mass. The SI unit of dose is the gray (Gy), where 1 Gy is equal to 1 J/kg.

$$D(\text{Gy}) = \frac{\text{Energy}(J)}{\text{Mass}(kg)} \quad (1)$$

The total dose to be delivered to the tumour is typically divided among several treatment sessions referred to as treatment fractions. The fractionation schedule and prescribed dose varies with cancer type and stage. Stereotactic body radiotherapy treatment (SBRT) uses a hypo-fractionated schedule. In this case, higher doses are delivered per fraction resulting in longer treatment delivery times for each fraction, but the overall treatment course is shorter. For NSCLC patients, non-SBRT treatments are typically delivered over 20-33 fractions, while SBRT treatments are delivered over 3-8 fractions.

1.3 Linear accelerators

In external photon beam radiotherapy, dose is delivered by high-energy photons produced in a linear accelerator.

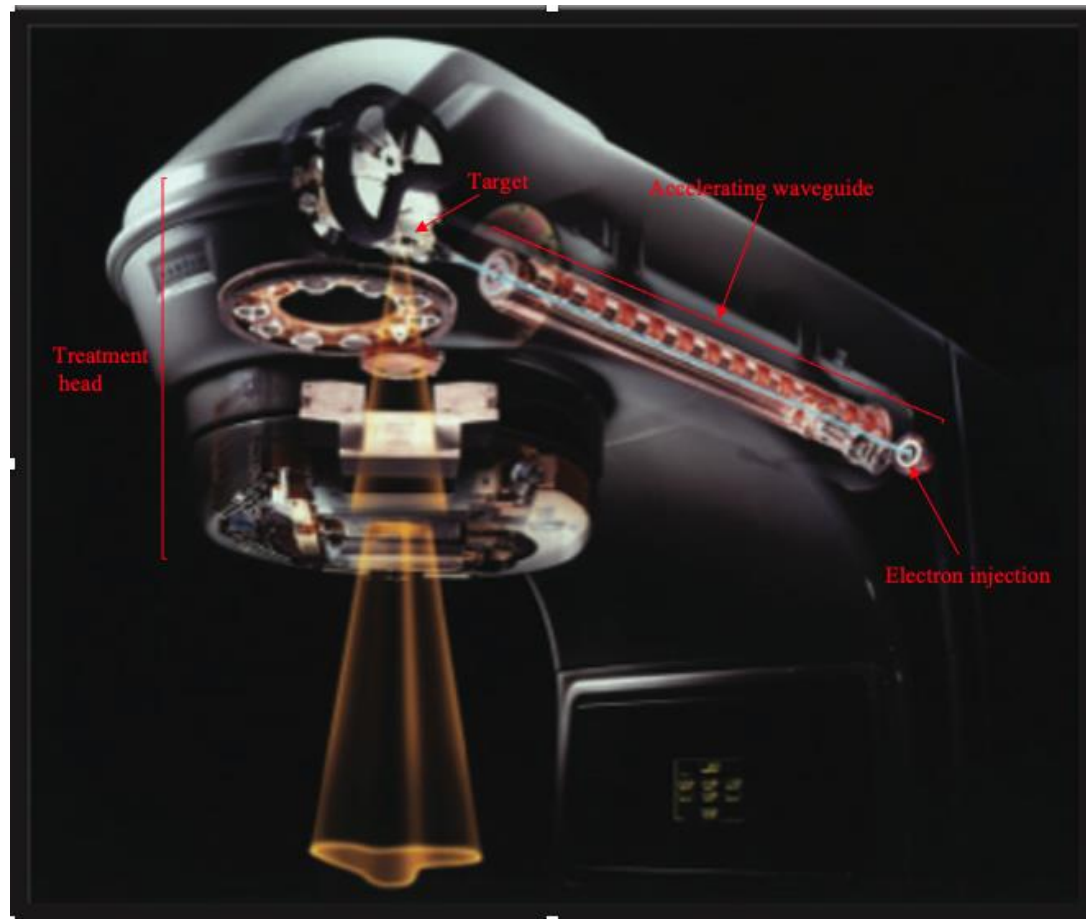


Figure 1.1: Diagram of a medical linear accelerator showing the waveguide, target and collimation systems which are shaping the photon beam (shown in orange). Figure modified from Galvin and De Neve⁴, reprinted with permission from Wolters Kluwer Health Inc.

The photon beam formation begins with an electron injection system in which an electron gun emits electrons from a heated cathode into the waveguide as can be seen in Figure 1.1. The electrons are accelerated in the waveguide by means of high energy radiofrequency electromagnetic fields produced by either a klystron or magnetron. The

electron beam emerging from the waveguide is then steered towards a heavy metal (high Z) target using a bending magnet. When the electrons interact with the target, a portion of their energy is converted into bremsstrahlung photons. The photon beam emanating from the target enters the treatment head and is filtered and collimated to match the treatment specifications. Modern linear accelerators typically have 3 collimation systems. The first is a fixed primary collimator which defines the maximum angular spread of the photon beam. The second collimation system is the multileaf collimator (MLC). The MLC consists of a set of 2 leaf banks which allow for the shaping of irregular fields. The system is composed of 80-120 leaf pairs (one in each bank) which can be individually controlled and positioned. An example of an MLC defined field is shown in Figure 1.2. The third collimation system is the jaws which consist of one or two pairs of tungsten blocks. The jaws can be used to define rectangular field shapes. In some linac designs, such as the Elekta Synergy, there is only one jaw pair which moves orthogonally to the MLC direction.

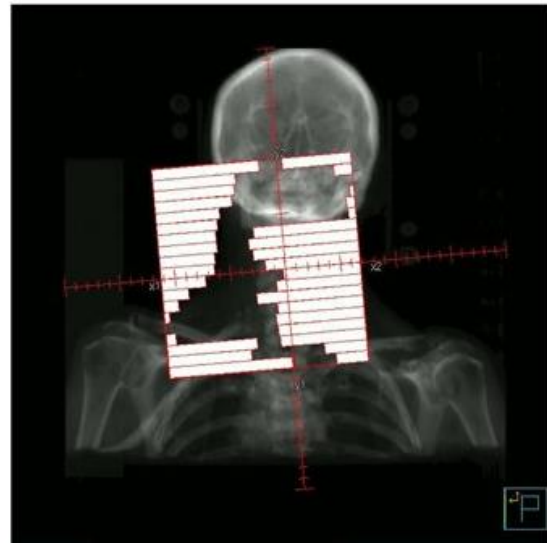


Figure 1.2: Example of an MLC collimated treatment field. Figure reprinted from Bedford et al⁵ licensed under CC BY 3.0.

The linear accelerator head and waveguide are mounted on a gantry which can rotate around the patient to deliver treatment at multiple angles as can be seen in Figure 1.3. The duration of each treatment is specified in terms of the number of monitor units (MU) required to deliver the prescribed dose. Monitor units are a measure of the linear accelerator output; 1 MU is equivalent to 1 cGy absorbed in water under reference conditions. Modern linacs have on-board kV imaging systems, which consist of a kV x-ray source and a flat-panel detector. X-ray projection images obtained with these systems can be used to guide the patient setup prior to treatment.

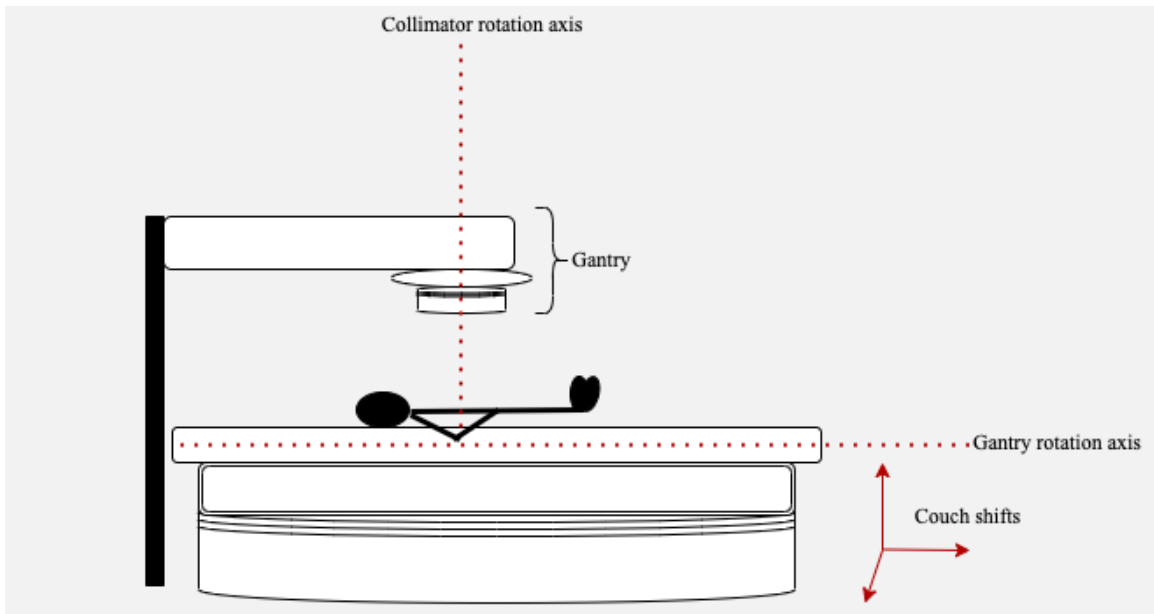


Figure 1.3: Treatment room layout, the collimator and gantry rotation axis and couch shift directions are shown in red.

1.4 Radiation treatment process

The typical radiation therapy process for NSCLC patients is shown in Figure 1.4. After the type of cancer and the appropriate type of treatment are determined, the patient is sent to the imaging suite for 4D-CT acquisition. During 4D-CT acquisition, a set of volumetric images of the patient at different respiratory phases is acquired. This scan is performed with the patient lying in the same supine position on the CT couch as they will be treated in. If the patient presents with a lower lung lobe tumour, the amount of tumour motion needs to be assessed on the 4D-CT images to determine if the patient will be treated with abdominal compression to minimize respiratory motion. If it is decided that abdominal compression is an appropriate measure to take, then another 4D-CT is acquired with the compression board and the patient is subsequently treated with the compression board. The acquired CT images are sent to the oncologist and planners for delineation of the tumour and organs at risk (OARs). OARs are healthy tissues in close proximity to the target whose radiation sensitivities may limit the treatment of the target.

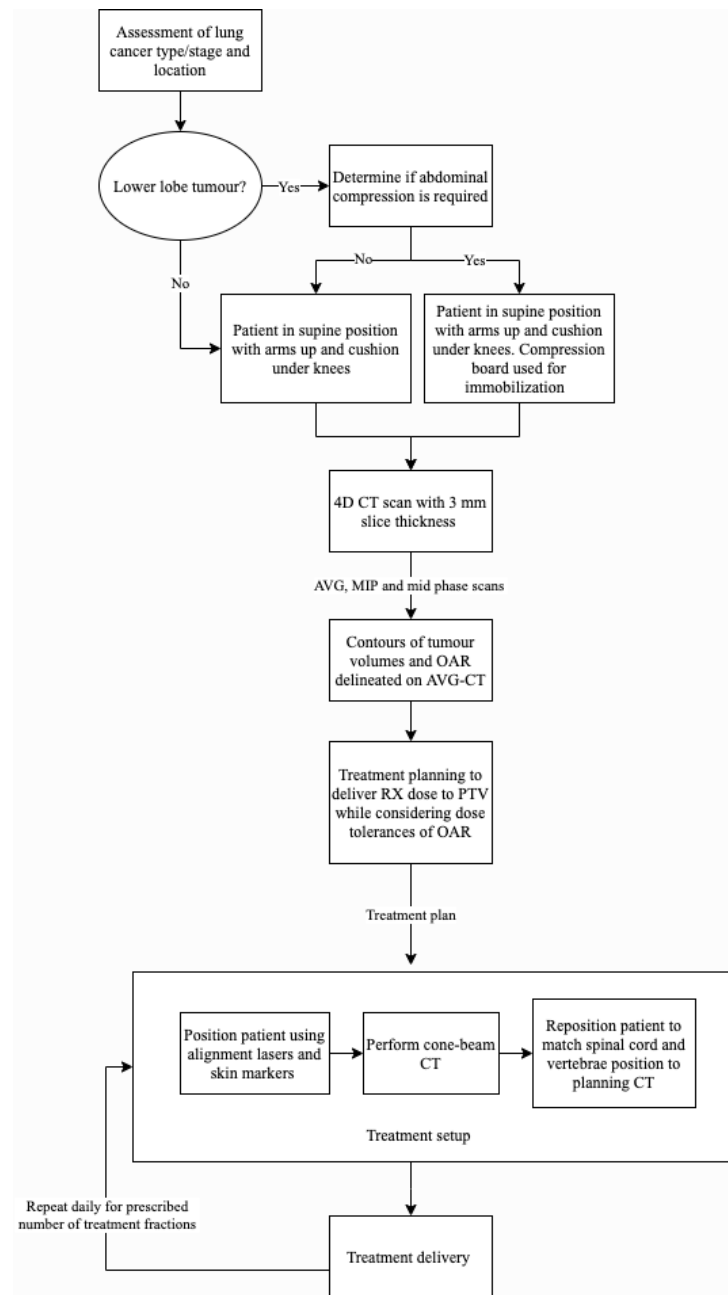


Figure 1.4: Example of workflow for the treatment of lung cancer at TOHCC.

Tumour delineation begins with the gross tumour volume (GTV) which is contoured by a physician and encompasses the visible portion of the tumour. A small margin is applied to the GTV to create the clinical target volume (CTV) which encompasses the tumour and any microscopic disease. In the case where the tumour is subject to motion, for

example due to respiration, the internal target volume (ITV) may be created by expanding the CTV to incorporate the motion of the tumour relative to the patient's own anatomy.

From the ITV, an expansion is added to create the planning target volume (PTV). The PTV margin is applied to account for any uncertainties in the treatment setup, target motion and variability in treatment delivery and is specific to the treatment type. The target volumes specified by the ICRU are outlined in Figure 1.5. While ideally only the PTV would be irradiated, nearby tissues often receive non-negligible radiation doses due to limitations in treatment delivery.⁶ At TOHCC, the ITV is defined by contouring the GTV on the maximum intensity projection (MIP) CT images. To this, an additional margin is added to form the CTV. The MIP is explained in more detail in section 2.3.1.

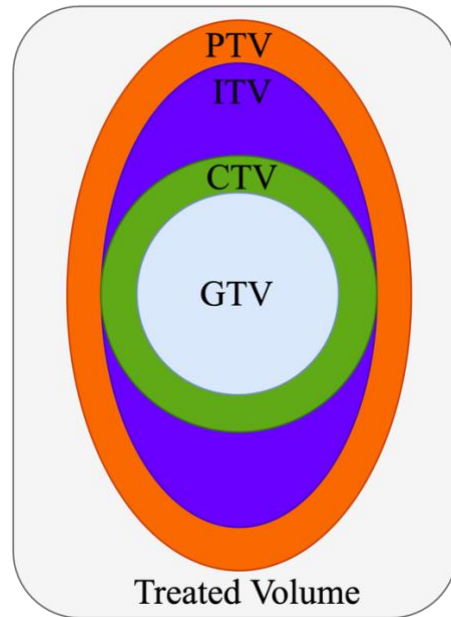


Figure 1.5: The GTV, CTV, ITV and PTV contours as described in ICRU reports 50 and 62.^{6,7}

After tumour and OAR delineation, a treatment plan is designed which delivers the prescribed dose to the PTV while ensuring that the dose to OARs is below the allowed

thresholds. The dose to be delivered to the PTV to achieve adequate tumour control is site specific and depends on the treatment technique, fractionation schedule and limiting factors such as dose constraints on nearby organs at risk (OARs). Dose thresholds for OARs are organ specific as sensitivity to radiation varies for different tissue types. The dose to the treated volume may be expressed as the volume receiving a percentage of the prescription dose, for example the V50% is the volume receiving 50% of the prescription dose. Alternatively, the dose may be expressed as the dose received by a certain percentage of the volume. The D90% is commonly used to express the dose received by 90% of the treated volume. The mean dose (Dmean) and the maximum dose (Dmax) received by a volume may also be used to express the amount of dose received. Doses to contoured structures may be presented as a dose volume histogram (DVH). A dose volume histogram is a representation of the radiation dose received by a given volume fraction of the target or OAR. An example of a DVH for a treatment prescribing 6000 cGy to 95% of the PTV is shown in Figure 1.6.

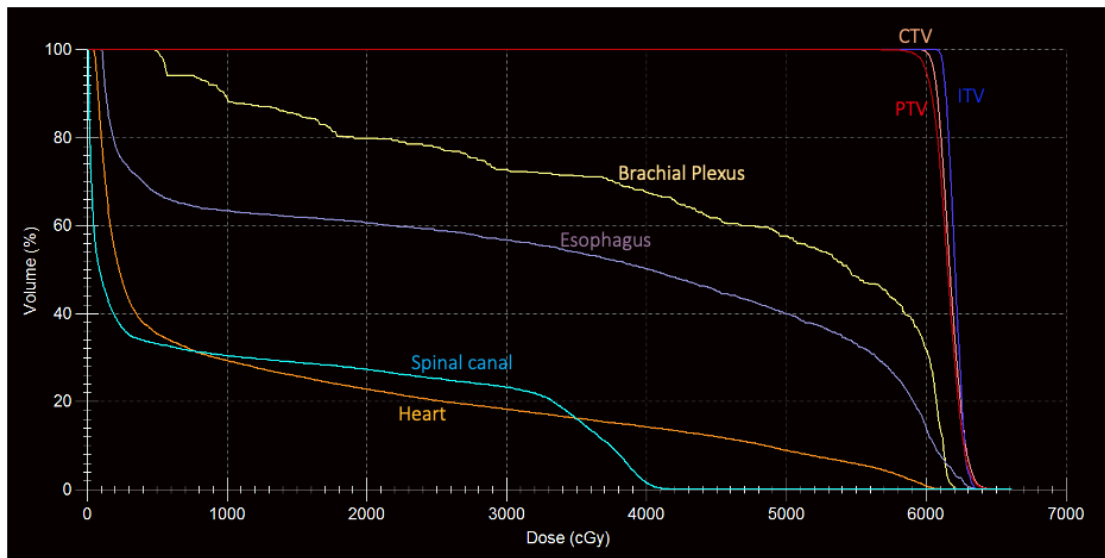


Figure 1.6: Dose volume histogram generated by a treatment prescribed to deliver 6000 cGy to 95% of the PTV. The doses to the nearby OAR are also shown.

Prior to each treatment the patient lies on a treatment couch and is positioned with the aid of alignment lasers. These lasers are matched to markers on the patient's surface tattooed at the time of CT image acquisition. Afterwards the patient may be repositioned by matching the position of the spinal cord and vertebrae in the planning CT image to images obtained with a cone-beam CT that are taken by the on-board image system of the linac. Treatments are repeated daily for the prescribed number of treatment fractions which is typically between 30 and 33 fractions.

1.5 Treatment delivery techniques

The type of treatment that is prescribed to the patients varies based on cancer type, stage, and the intent of the treatment. Commonly used treatment techniques are 3D conformal therapy, intensity modulated radiation therapy, and volumetric arc therapy.

1.5.1 3D conformal radiation therapy (3D CRT)

In 3D conformal treatments, multiple static radiation beams, incident from various coplanar angles, are used. An example of such an arrangement can be seen in Figure 1.7. The shape of each beam aperture is conformed to the outer contour of the target volume in a plane perpendicular to the beam direction (also known as the beam's eye view).⁸ In this method, a forward planning technique is used. In forward planning, the preliminary beam configurations including beam shapes and weights are set by the treatment planner. The resulting dose distribution is then calculated by the treatment planning system (TPS) for the predetermined beam arrangement, to determine the number of monitor units of

radiation delivered in the treatment. The beam arrangement may then be adjusted iteratively to achieve the desired dose distribution.

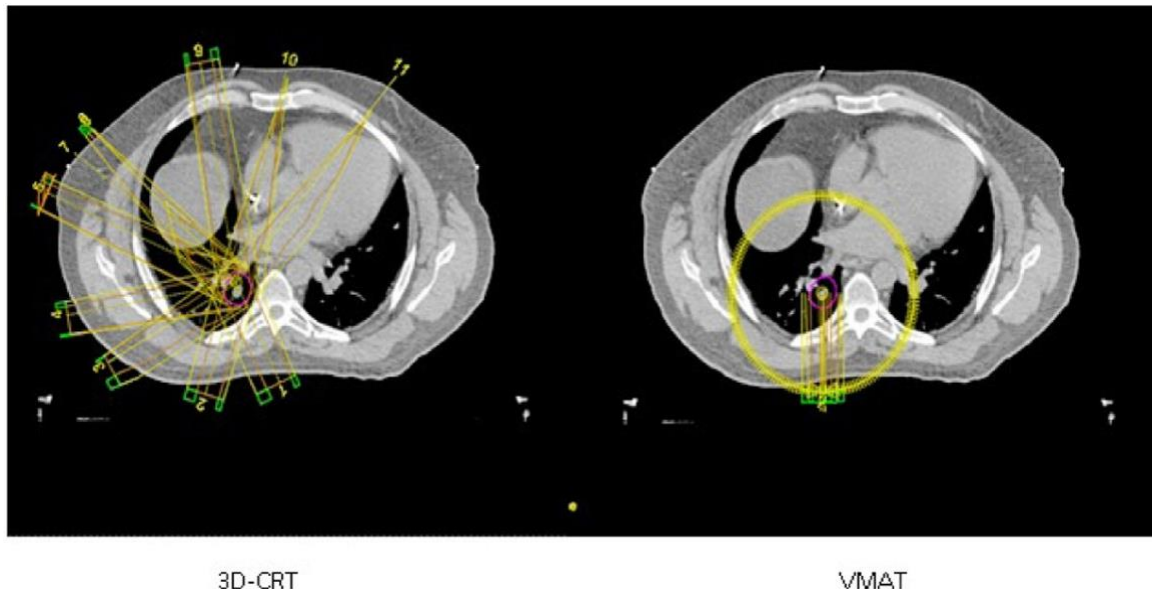


Figure 1.7: Comparison of beam arrangements for a 3D CRT (left) and VMAT treatment (right).

Figure modified from Rauschenbach et al⁹, licensed under CC BY 3.0.

1.5.2 Intensity modulated radiation therapy (IMRT)

In intensity modulated radiation therapy (IMRT), the beams have non-uniform intensities. This intensity modulation is achieved by moving the MLC leaves in and out of the beam during delivery. IMRT allows an increased level of tumour dose conformality compared to 3D conformal therapy.^{10,11} To plan IMRT treatments, an inverse planning technique is used. In inverse planning, the dose-volume constraints are set for the OARs and for the target. Then the TPS optimizes the 2D fluence map for each beam to best match these parameters. After the fluence map has been optimized, it needs to be converted into a set of deliverable MLC openings. After this beam sequencing is finished, a final dose

calculation will be performed to determine the number of MUs per treatment fraction. Since the MLC sequencing step inevitably leads to degradation of the plan quality from the initial, undeliverable, optimized fluence, modern TPS use direct aperture optimization (DAO) methods¹² where the positions of the MLC leaves defining the apertures are optimized to meet the specified dose-volume constraints.

1.5.3 Volumetric modulated arc therapy (VMAT)

Volumetric modulated arc therapy (VMAT) is an extension of IMRT where the gantry rotates around the patient in an arc while delivering intensity modulated treatments. An example of a VMAT arc is shown in Figure 1.7.

During VMAT treatments, modulation of the gantry speed, beam shape and dose rate occurs throughout the treatment arc. VMAT offers benefits over IMRT since treatment delivery times are generally shorter due to the continuous delivery. The shortened treatment time is beneficial because it can reduce intra-fractional patient motion and increase patient position reproducibility.¹¹ VMAT planning requires the use of direct aperture optimization¹³ in order to constrain the MLC openings, MU rate and gantry rotation speed to values that are practically achievable. A comparison of dose distributions and beam configurations achieved using VMAT and IMRT techniques are shown in Figure 1.8. In the case shown, the use of the VMAT technique allows for the sparing of the contralateral lung from doses above 18 Gy, as compared to the IMRT case.¹⁴

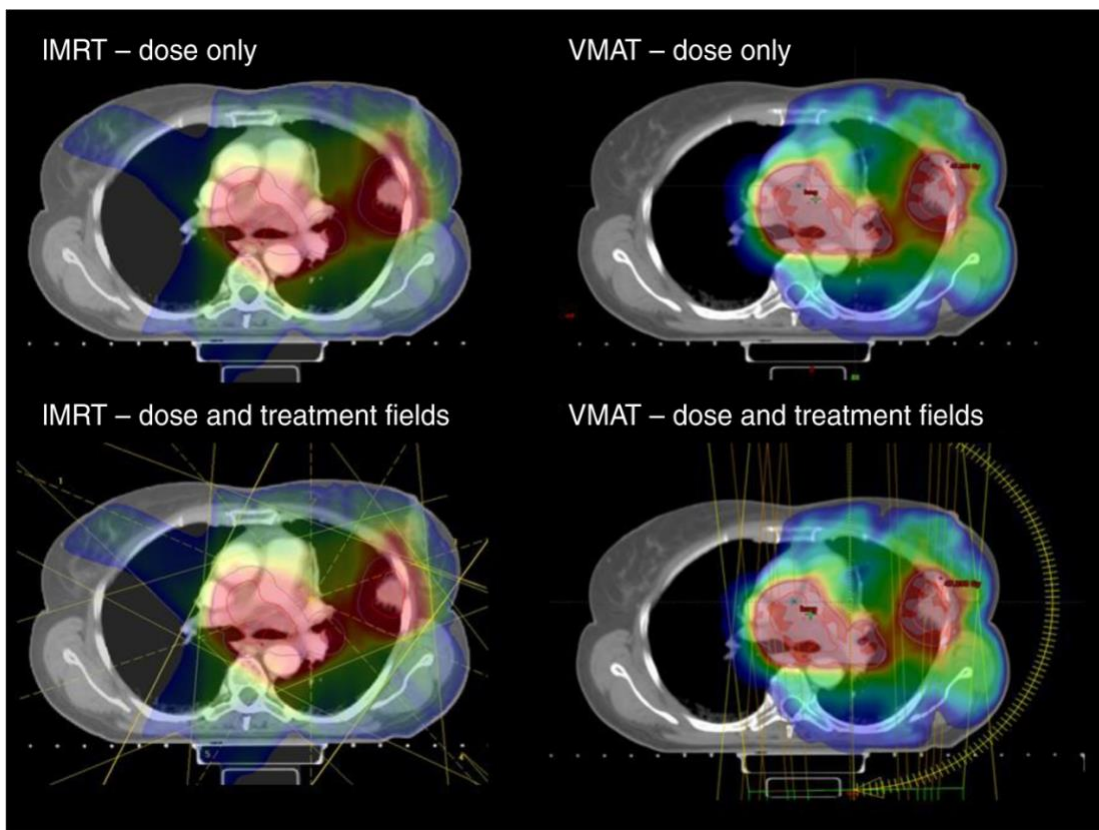


Figure 1.8: Differences in treatment fields used and dose distributions achieved using IMRT and VMAT treatment techniques. The threshold for the colour wash is 18 Gy (shown in dark blue). As demonstrated by the lack of dose above 18 Gy, the VMAT dose distribution demonstrates sparing of the contralateral lung. Figure reprinted from Storey et al.¹⁴ licensed under CC BY 4.0.

1.6 Motion compensation techniques

When any of the aforementioned treatment methods are used, possible tumour motion must still be considered. Respiratory motion is of particular concern when treating tumours in the lung. Breathing motion compensation techniques may include respiratory gating, breath-hold, and tumour tracking techniques. In gated treatments, the respiratory pattern of the patient is monitored, and the treatment is delivered only when the patient is in a predetermined portion of the respiratory cycle. In breath-hold treatments, treatment

delivery occurs only while the patient's breath is held. Tumour tracking treatments can be performed with ExacTrac system on a linac or the CyberKnife system. In these treatments, the tumour is tracked, and its position is predicted such that the trajectory of the beam is continuously updated to follow the tumour motion path.

1.7 Motivation

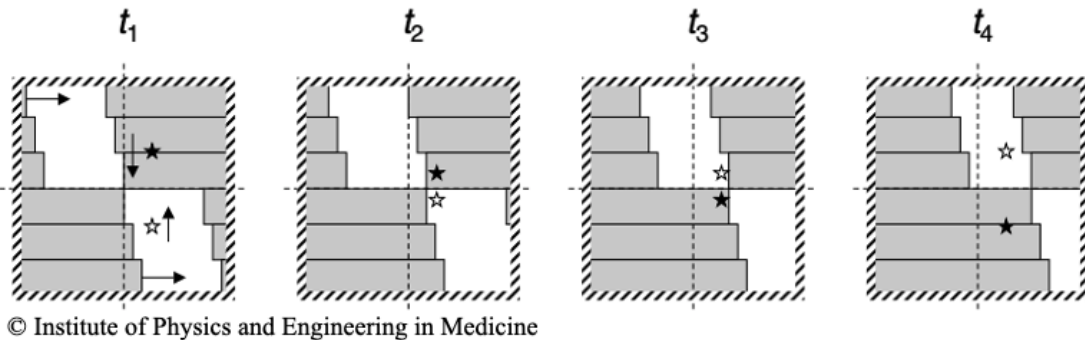
The goal of any treatment technique is to allow for sufficient dose delivery to the target, while sparing normal healthy tissue. However, this is made more difficult in sites where the tumour is subject to large amounts of motion due to respiration or other involuntary movements. Respiratory motion is an example of intra-fractional motion, as it occurs during the treatment delivery. Inter-fractional motion describes changes in the tumour position between treatment fractions. Inter-fractional changes are the result of patient setup errors, tumor shrinkage and internal tumour position shifts.

In the treatment of lung cancer, intra- and inter-fractional motion are compensated for during the treatment planning process by employing additional margins to create the PTV. Tumour motion is uniquely accounted for in the creation of the ITV based on the tumour motion observed during the planning session. While necessary to ensure adequate tumour coverage, the addition of generalized treatment margins is less than ideal as it increases the irradiation of healthy tissue.¹⁵

In addition, respiratory motion is subject to change and shows daily variations. The respiratory motion observed during the treatment planning phase may not always

represent what will be presented during treatment.¹⁶ Because of this, margins applied to the tumour based on treatment planning images may be insufficient or excessive leading to an underdosing of the tumour or the unnecessary irradiation of sensitive tissues. Furthermore, the actual dose delivered to the tumour while the patient is breathing may differ from what is planned by the TPS where dose is calculated on a static geometry. When radiation treatments are delivered to a target undergoing respiratory motion, the resulting dose distribution is a blurring of the static dose distribution calculated by the TPS.¹⁵ The blurring occurs over the path of the tumour's motion. In addition to the blurring, the dose delivered may be further altered from the planned dose distribution due to the interplay effect.¹⁷ The interplay effect is an additional distortion of the dose distribution observed when target motion occurs in the presence of MLC motion.¹⁷ A visualization of this effect is shown in Figure 1.9.

Even when motion mitigation techniques are used, the interplay and blurring effects may lead to the introduction of uncertainties in the delivered dose. The effect of motion on the dose delivered to the patient cannot be known until the treatment delivery is reconstructed considering the patient's motion at the time of treatment.



© Institute of Physics and Engineering in Medicine

Figure 1.9: Depiction of the interplay between the motion of an organ represented by the star and the movement of the MLC. In this case the MLC move to the left and right and the organ moves in the vertical direction. The two stars represent the organ in two different phases of respiration. In the case of the filled star, no primary dose is delivered between t1 and t4. On the other hand, if the organ was in a respiratory phase represented by the open star, it would have received the full primary dose. While these two cases are exemplary of an extreme, they are shown to illustrate the possible implications of the interplay effect. Figure reproduced from Bortfeld et al. by permission of IOP Publishing.¹⁷ All rights reserved.

1.8 Research goal

The goal of this study is to develop a workflow to reconstruct the dose delivered to patients undergoing VMAT treatments for the radiotherapy of NSCLC and to compare them to the planned dose from the treatment planning system. Using surface motion measurements acquired during each treatment fraction and treatment delivery log files generated by the linac, the doses to the patients were reconstructed using a novel 4D Monte Carlo dose calculation tool, 4Ddefdosxyznrc. This previously validated 4D reconstruction tool can model dose delivery under conditions of anatomical motion and

deformation using the real-time beam delivery information, and accounting for both the dose blurring and interplay effects of respiration.

1.9 Thesis organization

In chapter 2, the topic of motion during radiation therapy is covered in detail. The characteristics of respiratory motion are explained and the correlation between internal and external respiratory motion is reviewed. That chapter also includes a review of motion management techniques in radiation therapy and respiratory monitoring devices. In chapter 3, common dose calculation algorithms are presented, including Monte-Carlo based methods, and 4D dose calculation algorithms which include the effects of respiration are reviewed. In chapter 4, the application of the 4Ddefdosxyznrc user-code to a patient cohort for dose reconstruction is explained in detail and the results of these reconstructions are shown in chapter 5. In the final chapter, a discussion of the results and limitations of the study are presented.

Chapter 2: Respiratory motion during radiation therapy

2.1 Respiratory motion characteristics

Internal organ motion due to respiration is most notable in the lungs and organs in the upper abdomen, including the liver, kidneys and pancreas.¹⁵ As the diaphragm contracts during respiration, the chest cavity is expanded along the superior-inferior (S/I) direction and the abdomen is forced outwards in the anterior-posterior (A/P) direction.^{15,18} During quiet respiration, organ motion is predominantly in the (S/I) direction.^{15,19} Tumours in the thorax and upper abdomen, including the lung and liver, are subject to this respiratory motion and have also been shown to move along the S/I direction.^{15,20–22} This tumour motion can contribute to positional and dosimetric uncertainty that may require an increase in treatment margins.

While tumour motion is highly patient specific, it has been shown in multiple studies that unattached lower lobe tumours tend to move more than mid or upper lobe tumours.^{21,23} In a fluoroscopy-based tumour tracking study which visualized fiducials implanted in tumours, the observed motion in the S/I direction for lower unattached tumours was 12 ± 6 mm compared to 2 ± 2 mm for upper-lobe and attached tumours.²¹ In the same study, 6 of the 20 patients exhibited time trends in the baseline (exhale) position of the tumour during treatment beam delivery.²¹

Studies using external and internal surrogates for respiratory motion have also shown intra-fractional changes in exhale position in addition to inter-fractional changes in exhale position, respiratory period and daily displacement.^{16,24,25} In a fluoroscopic study,

diaphragm motion was tracked on a weekly basis following patients' treatments.²⁴ The diaphragm position was tracked in two ways: with respect to a bony reference point on the spine and with respect to the treatment isocenter.²⁴ While the diaphragm position remained relatively stable throughout each measurement session, the daily mean position of the diaphragm showed inter-session variability. For the position relative to the isocenter, the average change in the daily mean position for all patients was 0.38 ± 6.28 mm.²⁴ This was referred to as an inter-fractional 'shift' in the respiratory trace and was attributed to set-up errors and physiological changes in the patient lung volume.²⁴ For the 10 patients studied, the diaphragm excursion during respiration ranged from 5.59-47.6 mm.²⁴ In a study of chest-wall motion it was shown that over the full treatment course the total extent of the chest-wall motion had a median value of 15.2 mm with a range of 5.5-26.7 mm for the 11 patients studied.²⁵ This motion included both the breathing amplitude and changes to the exhale baseline position.²⁵ The authors found that the measured motion amplitude from a single treatment session corresponded to about half of the total motion extent of the chest-wall throughout the total course of treatment as the inter-fractional variation in baseline position dominated the full motion extent.²⁵

In another external motion study, the RADPOS system (described in 2.3.4) was used to measure inter- and intra-fractional changes in respiratory period and amplitude for 10 patients undergoing treatment for lung cancer.¹⁶ In this study the position of the patient's abdomen was tracked during radiation therapy treatments and the anterior-posterior (A/P) displacement of the abdomen was chosen as the surrogate for tumour motion. The RADPOS sensors were placed at the same location of the Bellows belt used during 4D-

CT. At the time of CT simulation, tattoos were placed on the patient surface to mark the RADPOS sensor locations for measurements during the treatment delivery. This study found that large inter-fractional changes in amplitude could occur and that for more than half of patients, the amplitude and period of respiration measured during treatments differed significantly when compared to measurements made during the 4D-CT acquisition. This was also true of the respiratory period. Maximal inter-fractional differences in average daily amplitude and respiratory period of 1.4-8.6 mm and 0.2-1.8 s were noted. While there was inter-patient variability in the changes of daily average amplitude and period, for one patient very large intra-fractional variations in amplitude and period of 24.1 mm and 11.9 s were observed.

2.2 Correlation between internal and external respiratory motion

The inference of tumour and organ motion based on external surrogates is an important step in many treatments that account for respiratory motion. External surrogates offer a non-invasive approach to assess respiratory motion without the use of implanted fiducials. The correlation between external surrogates and internal anatomy has been studied for various organs and tumours including liver tumours, lung structures, lung tumours and the diaphragm.²⁶⁻³⁵

During normal respiration the rib cage expands in the anterior direction while the diaphragm moves in the inferior direction. Consequently, studies have found good correlation between surface abdominal motion and the internal motion of the lung and tumour along the S/I direction.^{27-29,31} This correlation has been shown to vary from

fraction to fraction as the tumour-surrogate relationship depends heavily on the breathing pattern which can vary between treatments.³⁵ This correlation is also highly patient-specific and is difficult to predict based on patient demographics and characteristics.^{27,34} Many studies that investigated the correlation between lung and tumour motion with external surrogates have also noted a phase difference between the motion of the external surrogate and the internal target.^{28,29,31,32,35} These phase differences could be due to hysteresis which has been previously documented in tumour tracking studies.^{21,27} Hysteresis is a phenomenon where the path followed by the tumor is different in inhale and in exhale phases. This is attributed to the differences in the inflating and deflating lung volume at the same pressure.¹⁵ Lung volume changes have shown to have improved correlation with lung tumour motion over external surface motion. This is likely due to the fact that less of a phase difference is observed between lung volume changes and tumour motion as compared to differences with surface motion.²⁹ The correlation between lung volume measurements with tumour motion has been shown to display inter-fractional variations.²⁹

2.3 Respiratory monitoring devices

Respiratory monitoring devices are used in treatments which require tumour motion monitoring such as breath-hold, respiratory gating and tracking treatments (described in Section 2.4.2). These devices are also used in numerous studies which investigate inter- and intra-fractional tumour and organ motion. They may also be used during the treatment planning phase.

2.3.1 Implanted fiducials

Lung tumour localization and tracking can be achieved by the use of implanted fiducial markers.^{36–43} Fiducials are small metal markers, often made of gold, that are implanted in or around the location of a tumour to allow it to be visualized by a fluoroscopic imaging system. The fiducials are typically implanted in the lung tumour or in a nearby bronchi using a bronchoscope. In this method a fiducial is pushed through a catheter that is inserted into the bronchi and visualized with a fiberscope camera.^{38,41} Implantation can also occur under fluoroscopic, electromagnetic or ultrasound guidance.^{42,43} Fiducials have been shown to migrate after implantation and their position relative to the tumour can vary from fraction to fraction as the tumour decreases in volume and changes shape over the treatment course.³⁸ The stability of the position of implanted fiducial markers has been shown to depend on the location of implantation. Markers implanted in the lower lobe and placed peripherally as opposed to centrally were shown to be more stable than those in the upper lobe.⁴³ This method offers direct tracking of the tumour position, but, it is a more invasive method that may lead to complications due to fiducial implantation. External surrogates offer a less invasive approach to monitor respiratory motion.

2.3.2 Tumour motion surrogates

The Phillips Bellows belt (Philips Medical Systems, Cleveland, OH) is a pneumatic belt which is used as an external surrogate to measure respiratory motion. The Bellows belt has a rubber air-filled bellows which deforms with the patient's breath resulting in a change in pressure which is converted to a signal by a pressure transducer.^{44–46} This signal is displayed as a respiratory trace and a breath rate.^{44–46} The Bellows belt can be

used during 4D-CT acquisition to correlate the respiratory motion with the scan acquisition. For lung cancer patients undergoing treatment at TOHCC, the Bellows belt is used during 4D-CT acquisition at the treatment planning stage to tag and sort CT images into 10 respiratory phases ranging from full inhale to full exhale.

In the ABC system, described in more detail in section 2.4.2.2, lung volume changes measured with spirometry are used to track patient respiration.⁴⁷

Another external surrogate tracking system that can be used with 4D-CT is the Varian RPM system (Varian Medical Systems, Palo Alto, CA). This system consists of a plastic block which is placed on the patient's abdomen. The block has infrared reflecting dots that are recorded by a CCD camera with an infrared filter. This camera tracks the movement of the reflective markers as they move with the abdomen during respiration.^{48,30} The RPM system is also used during subsequent treatments where breath-hold or gating are used to manage respiratory motion.

Other optical positioning systems are used to minimize inter-fractional position changes by mapping the surface position of the patient. These systems include the AlignRT (VisionRT Ltd., London, UK) and the C-Rad Sentinel system (C-Rad AB, Uppsala, Sweden).⁴⁹ The AlignRT is a surface imaging system that uses multiple cameras and a speckle projection to obtain a 3D surface model of the patient that is registered to a reference image.^{49,50} The registration is then used to calculate the repositioning needed to realign the patient to the reference position.^{49,50} The C-Rad is a laser camera system that

functions as both a 3D and 4D tracking system of the patient surface. In this system, a narrow line laser is swept over the patient and is viewed by a camera to determine the 3D location of the points on the patient's surface.^{49,51} Similar to the AlignRT system, the surface location map is then registered to a reference map to allow for the detection of position changes and setup errors.^{49,51} The C-Rad system also allows for real-time position detection that can be used to assess surface motion throughout treatment.⁵¹

2.3.3 Electromagnetic trackers

Electromagnetic position sensors offer advantages over other methods in that no direct line of sight to the area being tracked is required and they don't increase the radiation dose to the patient. These sensors are relatively simple and low cost compared to other tracking systems. In these systems, an electromagnetic field of known properties is generated by a transmitter and the response of a tracker to this field is monitored and converted to a position signal.

The Calypso System (Varian Medical Systems, Palo Alto, CA) is a commonly used electromagnetic position sensor which can be implanted in and around the area of a tumour for tracking.⁵²⁻⁵⁴ This is a wireless transponder system, and does not require a wired connection to the tracker. This system is typically used for prostate although it has been studied for implantation in the lung.⁵⁴⁻⁵⁶ In this system, the implanted transponders, also referred to as 'beacons' are excited by a magnetic field generated in the tracking system. The excited transponders then emit a signal which is detected by a sensor array

and interpreted by a tracking algorithm. Implantation of beacons is an invasive procedure, which is a major disadvantage of Calypso System.

A general drawback of electromagnetic position trackers is their sensitivity to electrical background noise and interference from conductive materials. Electrical noise can create time varying electromagnetic fields which can alter the response of the detectors causing unwanted fluctuations in the position measurements.

2.3.4 RADPOS 4D position sensor

The RADPOS system (Best Medical Canada, Ottawa, ON) is a combined electromagnetic position sensor and MOSFET dosimeter.⁵⁷ In this work, the RADPOS detector was used as an external surrogate for respiratory motion to measure the respiratory motion of patient's during radiation treatment. This system has been previously evaluated and tested in the clinical environment.^{16,57} The position sensor is 8 mm in length and is mounted on a wire along with the MOSFET sensor. The position probe is connected to a 3D-Guidance preamplifier and the system position tracker. The tracker is also connected to the transmitter which produces the pulsed magnetic field sensed by the position probe.⁵⁸ A schematic of the system is given in Figure 2.1.

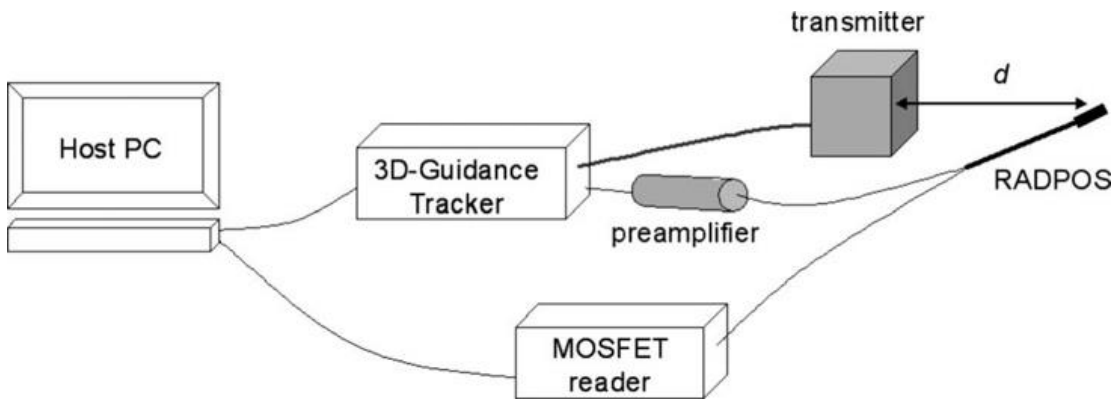


Figure 2.1: RADPOS system configuration as described by Cherpak et al.⁵⁷, reprinted with permission.

The noise of the RADPOS position measurements was found to be within 0.21 ± 0.07 mm over the period of an hour and was stable for the duration of that measurement. The system performed similarly when tested in the treatment room with the radiation beam turned on. The accuracy of the position measurements along the in-plane, cross-plane and depth axes was also studied and it was found that the optimal range for position measurements are 150-470 mm, ± 215 mm and ± 100 mm in the in-plane, cross-plane and depth directions for an origin defined 200 mm away from the transmitter in the in-plane direction.⁵⁷ The effect of interference from nonmagnetic (austenitic) stainless steel, aluminum, lead, brass, acrylic, lexan and polystyrene on position measurements was found to be minimal when the material was placed further than 200 mm from the detector.⁵⁷ In general, the ferromagnetic and conductive properties of the material were the major determinants of the disturbance it would cause to the field produced by the transmitter.⁵⁷ It was also concluded that for the optimal accuracy and the least amount of interference, the transmitter should be placed away from any electrical devices and placed such that there are no interfering materials between the detector and transmitter.⁵⁷

2.4 Motion compensation techniques

2.4.1 Treatment planning techniques

Treatment planning techniques can be used to account for the excursion of the tumour due to respiration during treatment delivery. One of the methods used to obtain CT images for treatment planning in the presence of respiratory motion is the 4D respiratory correlated CT, 4D-CT.^{15,59} In 4D-CT acquisition, the CT data at each slice are obtained continuously for multiple respiratory phases. To obtain these data, the patient is scanned in axial cine mode or in helical mode with a low pitch.^{15,59,60} During the scan, the patient wears a surface motion monitoring system which correlates the scan acquisition to the patient's respiratory motion. Using this respiratory signal, the images obtained at each slice position are binned according to either the respiratory phase or amplitude of the measured respiratory signal.^{32,46} The result of this scan are multiple volumetric image sets representing the anatomy of the patient at different phases of the patient's respiratory cycle.

The maximum intensity projection (MIP) image set is a volumetric CT image set which displays the maximum intensity in each voxel throughout all phases in the 4D-CT set.^{61–63} The MIP yields a full tumour-motion-encompassing volume, a projection of the full excursion of the tumour during respiration.¹⁵ Because the MIP accounts for the intra-fractional motion of the tumour at the time of 4D-CT, at TOHCC, a patient specific ITV can be generated by contouring the tumour on the MIP image set.⁶³ A common protocol is to use the MIP to derive the ITV contour and then use the average intensity projection CT scan, AVG-CT, for dose calculation.^{64,65} The AVG-CT is the image set calculated by

taking the mean image intensity at each voxel in the 4D-CT volume. This image set shows the blurred path of the tumor throughout the 4D-CT scan. Calculating the dose on this image set has been shown to produce results comparable to what would be achieved by a 4D dose calculation.⁶⁵

Another approach is the mid-ventilation approach. The mid-ventilation CT image set is the CT image set which is reconstructed to display the anatomy at its time-averaged position over all of the binned respiratory phases from 4D-CT.^{66,67} It has been shown that treatment plans for lung tumours calculated on the mid-ventilation scan had good agreement with those calculated on the AVG-CT.⁶⁶

2.4.2 Treatment delivery techniques

The goal of these motion compensation techniques is to either reduce the motion of the tumour and its surrounding anatomy during radiation delivery or to adapt the treatment to compensate for the effects of tumour motion. This is important as it allows to reduce treatment margins during planning and spare the maximal amount of healthy tissue while maintaining sufficient tumour coverage.

2.4.2.1 Respiratory gating

Respiratory gating is a treatment delivery method wherein the patient respiration is monitored, and radiation is delivered only during a certain portion of the respiratory cycle, which is termed the gating window. If the tumour is being tracked, the gating window generally corresponds to a particular tumour location.⁶⁸ In the more common case where an external surrogate is being used to represent respiratory motion, the gating

window corresponds to a particular phase of the respiratory cycle.^{69,70,45} In gated treatments, the motion of anatomy during radiation delivery is effectively restricted to a small range within the gating window which is selected at the time of planning.^{69,70,71}

2.4.2.2 Breath-hold techniques

Breath-hold methods are also used to limit the amount of organ and tumour motion during treatment delivery. In these controlled breathing treatments, the patient holds their breath during the treatment delivery. In deep inspiration breath-hold, DIBH, the patient's breath is held during deep inspiration.^{69,72-74} Not only does this immobilize the lungs and lung tumours but it also increases the volume of the lung which can potentially decrease the amount of lung tissue receiving a high dose of radiation.^{72,74} In DIBH, respiration is monitored with a spirometer or an external surrogate such as RPM and the patients are coached so they are achieving the same inspiration level during treatment as at the time of planning CT.

The DIBH method can be implemented using the Active Breathing Control system, ABC.^{47,75} In this system the patients' breath is temporarily held during beam delivery.^{47,75} When the patient's respiration is at a predetermined volume, direction of the airflow through the device is blocked and the patient's breath is held for a duration that has been determined to be comfortable for the patient.^{47,75} The radiation is delivered only during the breath-hold period. It has been shown that using the ABC system, peripheral tumours were effectively immobilized during the breath-hold in a reproducible inter-fractional position.⁷⁵ However, breath-hold methods may not always be well tolerated by patients,

especially by lung cancer patients who may have compromised lung function,, In such cases, gated treatments with external tracking may be more suitable options.^{49,75}

2.4.2.3 Abdominal compression

At TOHCC, in addition to immobilization devices, an abdominal compression plate is used to restrict the respiratory motion of patients who display lung tumour motion greater than 5 mm. The plate is secured to an arched frame that is attached to the treatment couch. A screw connecting the plate to the frame is tightened to apply pressure to and compress the patient's abdomen.^{76,77} In a fluoroscopic study of the effect of abdominal compression on tumour immobilization, abdominal compression reduced the mean respiratory tumour motion exhibited by the study group from 12.3 to 7 mm.⁷⁸ In another study that compared immobilization using the Bodyfix system (Medical Intelligence, Elekta, Schwabmunchen, Germany) and the Abdominal Compression Plate (Medical Intelligence, Elekta, Schwabmunchen, Germany), it was found that both significantly decreased the overall lung tumour motion compared to the motion observed during free breathing.⁷⁷ The Bodyfix system consists of vacuum cushion, cover sheet, vacuum pump and pads. The vacuum cushion which is placed under the patient molds to the patient and is reused for all fractions reducing motion and increasing position reproducibility. Pads are then placed on the patient's abdomen and chest for abdominal compression. For increased immobilization a plastic cover sheet is then placed over the patient and a vacuum pump is used to remove the air between the sheet and the patient. The Bodyfix and Abdominal Compression Plate systems are shown in Figure 2.2.

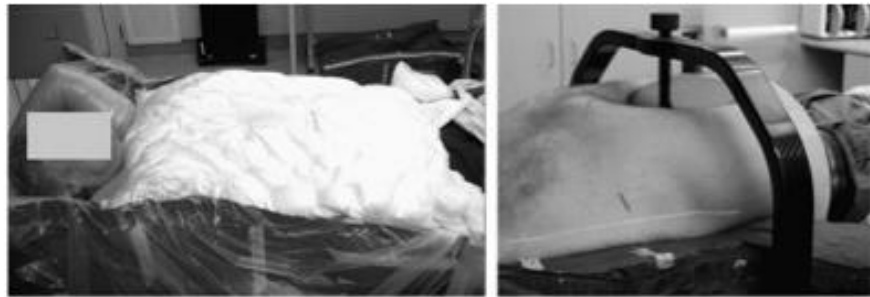


Figure 2.2: Comparison of the Bodyfix system (left) and the abdominal compression plate (right) used in the study by Han et al, reprinted with permission.⁷⁷

2.4.2.4 Real-time tumour tracking

Real-time tumour tracking during delivery is another method that can be used to compensate for respiratory motion during radiation therapy.^{79–81} The most commonly used system is CyberKnife system (Accuray Inc., Sunnyvale, CA, USA). It is a stereotactic radiosurgery system that consists of a linac mounted on a robotic arm that actively compensates for motion during radiation therapy. The tumour is visualized in real-time throughout the treatment by diagnostic x-rays units mounted in the treatment room and the respiratory motion is tracked via an external surrogate on the patient surface. Unlike in gating, breath-hold, and compression treatments, the patient breathes normally throughout the treatment. In these treatments, the beam follows the internal tumour motion by continuously measuring and updating an internal-external motion correlation model. This model allows for the beam trajectory to be adapted and move to the prediction target position. Because of the continuously updated correlation model between the external surrogate and internal motion and the adaptation of the treatment beam, treatments with CyberKnife do not depend on regular breathing and are able to account for inter- and intra-fractional changes in internal-external correlation, baseline

position, breathing phase and amplitude.⁸⁰ For visualization of the tumour with X-ray imaging, typically implantation of fiducials into and/or around the tumour is required and therefore the need for stable and non-migrating fiducial markers is required, making this method more invasive than those that use only an external surrogate for tumour motion. Additionally, these treatments are longer in time than treatments on conventional linacs, with typical treatments taking between 60 and 90 minutes.⁸⁰ Other image guided radiation therapy systems include, the ExacTrac system (ExacTrac, Brainlab, Feldkirchen, Germany)⁸² and the Vero4DRT gimbaled linac system (MHI-TM2000; Mitsubishi Heavy Industries, Ltd., Japan, and BrainLAB, Feldkirchen, Germany).^{83,84}

Chapter 3: Dose Calculation Algorithms

3.1 Overview of dose calculation algorithms

The accuracy of dose calculation tools is of critical importance in the treatment planning process.⁸⁵ The dose calculation process can be divided into 2 steps: the modeling of the treatment beam and the calculation of the dose delivered by said beam to the patient (or any geometry of interest).

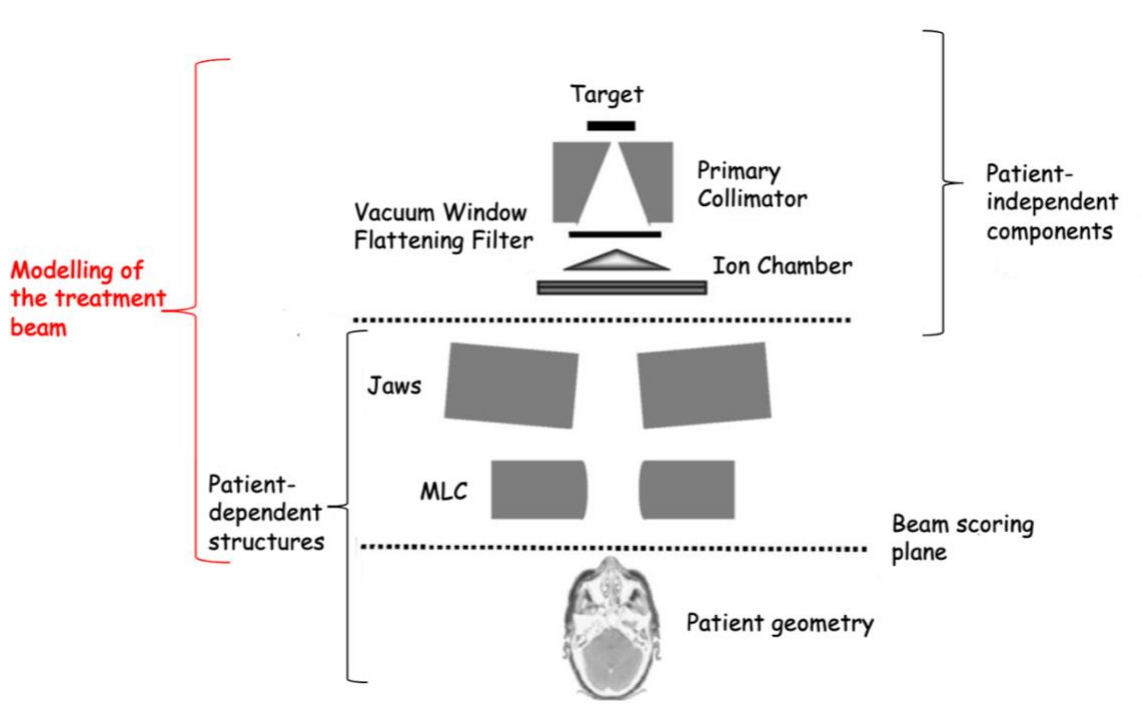


Figure 3.1: Illustration of the components to be simulated in a dose calculation. The position of the jaws and MLC will vary for each patient and treatment type and are therefore considered to be patient dependent. Figure adapted from Chetty et al.⁸⁶, licensed under CC BY 3.0.

Instead of an explicit model of the linear accelerator, dose calculation algorithms used in treatment planning systems often employ source models for modelling of the treatment beam.^{87,88} In this case, the linac beam is described by its phase space which provides particle energy and fluence information from 3 sources: photons emerging from the

target, those that are scattered from primary beam collimation devices and contamination electrons.^{87,88} The source model parameters are determined from fitting to measured dose distributions and/or from Monte Carlo simulations of the treatment head.⁸⁷⁻⁸⁹ Various algorithms exist in treatment planning systems to calculate the dose delivered to a medium by an external photon beam. Commonly used dose calculation algorithms are convolution/superposition, pencil-beam, linear Boltzmann and Monte Carlo methods. Convolution/superposition and pencil beam algorithms are both examples of kernel based algorithms used for dose calculations.⁹⁰ Kernels represent the distribution of energy deposition due to secondary particles emerging from an interaction of a primary photon with given energy at a point in the dose calculation geometry. In homogeneous infinite media, kernels are assumed to be invariant; these kernels are often calculated with Monte Carlo algorithms. In convolution/superposition algorithms, the distribution of energy released by primary photons in the volume per unit mass is convolved with the kernel describing the energy spread from each primary interaction.^{91,92} To account for inhomogeneities, kernels are corrected according to the density of the medium. This method is widely used in treatment planning systems and an example is the collapsed cone convolution algorithm (CCC).⁹³

Pencil beam algorithms are computationally simpler. In these algorithms the beam is divided into several small beamlets. A pencil-kernel corresponding to the superposition of point kernels along the direction of each beamlet is then convolved with the cross-sectional primary photon fluence to calculate the dose from each beamlet.^{92,94} Dose calculations in the lung are more complicated due to tissue inhomogeneities, particularly

near the lung-tumour boundary. Pencil beam algorithms have worse dose calculation accuracy in regions of low density, such as the lung.⁹⁵ In these regions there can be lateral electronic disequilibrium, which is unaccounted for in pencil beam algorithms.⁹⁵ These inaccuracies have shown to increase with decreasing field size and beam energy.⁹⁵ In a 2004 study of a single beam incident on a water-lung phantom, dose distributions from a pencil beam based TPS and a Monte Carlo code were compared to film measurements.⁹⁵ In the lung regions of the phantom, dose differences of up to 15% were observed between the pencil-beam dose calculations and the film measurements.⁹⁵ On the other hand, a Monte Carlo code was able to accurately calculate the dose distribution in the lung and near the water-lung interface.⁹⁵ Therefore, when calculating the dose to the lung, a pencil-beam algorithm is not generally recommended as it has been shown to significantly overestimate the dose to targets in the lung.^{96,97} This has been shown for single beams⁹⁸, IMRT⁹⁹ and stereotactic treatment plans.¹⁰⁰

Recently, dose calculation algorithms that solve the linear Boltzmann transport equations (LBTE methods) have gained popularity. LBTEs describe the change in fluence of a beam as it travels through a medium. These equations can be solved numerically for photons and electrons to calculate the total fluence in the medium. From this fluence, the absorbed dose can be calculated.¹⁰¹

Monte Carlo simulations are considered the most accurate dose calculation algorithms and are the preferred technique for modelling the transport of radiation through matter.

In Monte Carlo simulations, the interactions of ionizing particles with matter are explicitly simulated. Probability functions describing known physical processes are used to describe possible interaction types and products. Because of its statistical nature, the computation times for Monte Carlo dose calculations are often longer than the other methods described above and therefore are often implemented in planning systems as a final dose calculation step only. The Monte Carlo method is described in more detail in section 3.2.

3.2 Monte Carlo Dose simulations

3.2.1 Monte Carlo fundamentals

Monte Carlo methods for dose calculation are considered to be the most accurate, specifically in heterogeneous media.⁸⁶ These methods explicitly track the transport of particles through a medium by use of random number generation and the sampling from probability distributions that govern the known physical interaction processes. For example, when a photon, with energy E , is incident on a medium the probability that it will not interact over a distance x is described by the attenuation law

$$p(x) = e^{-\mu(E)x} \quad 3.1$$

where $\mu(E)$ is the linear attenuation coefficient at energy E . The linear attenuation coefficient describes the probability that a particle with energy E will interact in a medium over a very short distance. The inverse of the linear attenuation coefficient yields the mean free path (MFP). The mean free path specifies the average path length between interactions.

$$MFP(E) = \frac{1}{\mu(E)} \quad 3.2$$

The probability that a photon will have undergone an interaction after travelling a distance s can be calculated with the cumulative probability distribution function that follows from equation 3.1.

$$P(s) = \int_0^s \mu(E) e^{-\mu(E)x} dx = 1 - e^{-\mu(E)s} \quad 3.3$$

Where the probability of an interaction after travelling a distance of 0, $P(0)$, is 0 and the probability of an interaction after travelling an infinite distance, $P(\infty)$ is 1.

To randomly sample the path length, s , traveled by a photon until an interaction, a random number between 0 and 1, ε , will be sampled from a uniform interval and applied to the above probability distribution.

$$\varepsilon = 1 - e^{-\mu(E)s} \quad 3.3$$

$$s = \frac{-1}{\mu(E)} \ln(1 - \varepsilon) \quad 3.4$$

In this interaction, the photon can undergo either Compton scattering, the photo-electric effect, Rayleigh scattering or pair production. The probability of each interaction is given by the interaction cross-section for each process. The type of interaction is sampled by the generation of another random number and the energy and direction of all emerging particles are sampled according to the known cross-sections. The process continues and repeats for all emerging particles until they leave the geometry of interest or fall below a

set energy cut-off. Because of the statistical nature of this process a large number of particle histories are simulated to reduce the uncertainty in the scored dose. Each particle history includes the total travel of an initial particle through the geometry and the tracking of all secondary particles that are created. The energy deposited to each voxel from each history is then scored and the dose is calculated by dividing this energy by the mass of the voxel's mass.

Charged particles can undergo many small, mostly elastic, scattering events before they fall below the set energy cut-off. This is often too computationally intensive to simulate explicitly. Therefore, many Monte Carlo transport codes use the ‘condensed history’ technique.^{102,103} In this technique, the scattering events resulting in small energy transfers, referred to as ‘soft’ collisions, are condensed into one step. This step is modeled as a continuous energy loss and only scattering or bremsstrahlung events that result in the emission of a secondary electrons or photons above certain energy thresholds are modeled explicitly.

3.2.2 XVMC Monte Carlo code

The XVMC code utilizes multiple approximations to facilitate faster calculations than a traditional Monte Carlo code. This decrease in calculation time allows it to be used more easily in clinical settings. This algorithm is based on the VMC (Voxel Monte Carlo) code, which applied approximations to the traditional Monte Carlo method to speed up electron dose calculations.¹⁰⁴ The XVMC code extends this method to also be applicable to photons beams. One of the main increases in efficiency comes from an initial beam

tracing model.¹⁰⁵ This model pre-calculates the number of Compton and pair-production interactions in each voxel from the primary beam, the resulting particles from these interactions are then simulated explicitly.¹⁰⁵ The XVMC code does not rely on a material assignment in each voxel to determine radiation transport parameters. Instead, the photon attenuation coefficients and the electron stopping and scattering powers are derived by adjusting the coefficients for water according to the electron density of the voxel.¹⁰⁵ The lack of material assignment saves times during the calculation by reducing the look-up of transport parameters. Additionally, the transport of electrons in the simulation is sped up by the use of a simplified multiple scattering model compared to what is used in general purpose Monte Carlo codes such as EGS.¹⁰⁴ The code also uses a technique that re-uses electron tracks to save time during calculations. The electron path through homogenous water is simulated, this path is then applied at multiple location in the dose calculation geometry by correcting the path lengths, energies and scattering angles of particles in the original path according to the electron density of the media.^{105,106} An added increase in efficiency comes from the immediate discarding of bremsstrahlung photons after their production as their contribution to dose is negligible.^{104,105}

3.3 EGSnrc Monte Carlo code

There are several popular Monte Carlo codes that can be used to model the transport of radiation through matter including: EGS¹⁰⁷, PENELOPE¹⁰⁸, GEANT¹⁰⁹ and MCNP¹¹⁰. The Electron-Gamma-Shower system, EGS¹⁰⁷, is one of the most widely used systems in medical physics for the Monte Carlo transport of electron and photons.⁸⁶ The EGSnrc system is an improvement on the original EGS code and supports the transport of

particles with energies of the order of keV up to those with GeV energies. The system is tailored for medical physics applications and is maintained by the Ionizing Radiation Standards Group at the National Research Council of Canada (NRC). The EGSnrc code is divided into the main EGSnrc code and various user codes. Briefly, a user code specifies the geometry (HOWFAR, HOWNEAR) and scoring options (AUSGAB) for the simulation.¹⁰³ All of the radiation transport is modelled in the main EGSnrc code. Several user codes are available to be used with the EGSnrc system, including BEAMnrc¹¹¹ and DOSXYZnrc¹¹² which can be used to simulate an external photon beam generated by a linear accelerator and the resulting dose deposition to a patient, respectively.

3.3.1 Accelerator modelling with BEAMnrc

The BEAMnrc code was developed as part of the OMEGA project tasked with developing an electron beam treatment planning system using Monte Carlo techniques.¹¹¹ It is a code that can simulate the production of radiation beams emanating from linear accelerators.¹¹¹ In the BEAMnrc code, a model of the linear accelerator in question is built from component modules, CMs.¹¹¹ These are pre-defined geometries which operate independently of each other and are used to define the components of the linear accelerator such as the MLC, jaws, flattening filters, etc.¹¹¹ The properties of the component modules are specified in an input file and the machine model is built by combining all of the specified CMs.¹¹¹ The output of a BEAMnrc simulation is typically a phase space file specifying the type, energy, direction and weight of all particles at a user-defined scoring plane. This phase space file may then be used as input to a subsequent Monte Carlo simulation where the dose distribution from the accelerator

beam is calculated. Alternatively, the BEAMnrc accelerator model can be used as a particle source for the dose calculation simulation.¹¹¹

3.3.2 Dose calculations with DOSXYZnrc

DOSXYZnrc¹¹² is another EGSnrc user code that can be used to calculate the dose delivered to a rectilinear voxelized phantom. In this code the density and material of every voxel in the phantom can be specified in an egsphant file. DOSXYZnrc simulates the transport of incident particles through the phantom and the energy deposition by those particles is scored in each voxel. The radiation incident on this phantom can be from a monoenergetic beam, phase-space data from an independent BEAMnrc simulation or from a virtual source model. The recently added DOSXYZnrc source 21¹¹² allows for the synchronization of the DOSXYZnrc and BEAMnrc simulations without the use of an intermediate phase-space file.^{112,113} In this case, the full BEAMnrc treatment head simulation is used as a source for the DOSXYZnrc simulations every time a new particle is required.²² These particles are sampled from the previously mentioned beam scoring place specified in the accelerator model. Using source 21 allows for the synchronization of continuously changing parameters in DOSXYZnrc such as a gantry, collimator and couch rotation, source to axis distance and isocentre location with the dynamic MLC and jaws in the BEAMnrc simulation.^{112,114} The BEAMnrc and DOSXYZnrc simulations are synchronized with the MU fraction index. The MU fraction index, which lies between 0 and 1, is randomly sampled for each incident particle history to determine the position of the dynamic components in the accelerator model and is passed to DOSXYZnrc where it is subsequently used to sample the dynamic DOSXYZ parameters.

3.4 Monaco TPS

At TOHCC, the Monaco (Elekta AB, Stockholm, Sweden) TPS is used for patient dose calculations. This TPS employs a virtual source model (VSM) for treatment beam modelling. The Monaco VSM employs three particle sources each defined as having a gaussian spatial distributions.^{87,106} The particles emerge from the virtual source model at a scoring plane where they are sampled and transmitted through the beam modifiers (jaws and MLC).The transmission of these particles through the jaws and MLC is modelled by transmission probability distributions. These filters only determine transmission, they do not alter the particle energies or direction, nor do they generate any secondary particles.^{87,106} At this point the particles are tracked in the patient geometry using either a Monte Carlo algorithm or a CCC calculation. The Monte Carlo code used is the XVMC (X-ray Voxel Monte Carlo) algorithm¹⁰⁵ described in detail in section 3.2.2.

In Monaco, dose optimization performed prior to the final calculation is done with a finite pencil beam algorithm. The finite pencil beam kernels are derived from broad beams; the main principle is that a beamlet can be seen as the difference of two broad beams with a small change in a single beam parameter.^{106,115} The shape of the finite pencil beams is described by an analytical function whose parameters are fit according to dose profiles derived from broad beam Monte Carlo calculations.^{106,115} To account for inhomogeneities in the medium, correction factors are included in the function parameters.¹⁰⁶ After dose optimization, the final dose calculation is performed with either the XVMC or a CCC dose calculation algorithm. Dose calculations are performed on the

phase averaged CT scan, AVG-CT. As a result of this, the clinical treatment planning calculations do not explicitly account for temporal changes of the patient's anatomy, which are considered only by the creation of the ITV margin.

3.5 4D dose calculation methods

The BEAMnrc/DOSXYZnrc source 21 combination allows for the simulation of a dynamic beam delivery on a static patient geometry. In the case where the patient geometry is changing due to respiratory motion, a 4D dose calculation method is required.

A 4D dose calculation method should account for the following effects of respiratory motion on the dose distribution: the blurring of the dose distribution, the interplay between organ motion and the motion of the dynamic components of the linac such as the MLC, and the distortion of dose distributions at interfaces between structures where local deformations can cause changes in density.¹¹⁶ To model all of these effects a 4D method must calculate the dose on multiple instances (e.g. respiratory phases) of the patient anatomy and then combine these dose distributions to obtain a cumulative dose distribution.

3.5.1 Dose-mapping methods

To account for the motion and deformation of anatomy during irradiation, the dose at each respiratory phase can be calculated and mapped back to a reference geometry using a weighting factor that accounts for the relative amount of time spent in that phase.¹¹⁷ To map the dose back to the reference geometry, deformable image registration algorithms

are often used to model the geometric transformation of the anatomy from the reference phase to the various respiratory phases used for calculations.^{118–122} An image registration algorithm determines the geometric transformation that optimizes the alignment between a secondary image and a reference image. This registration can be rigid, which assumes only the translation and rotation of anatomy, or deformable, which allows for the morphing of the image grid to account for deformation of the anatomy.¹²³ The output of a deformable image registration is a 3D set of deformation vectors for each voxel of the image.

In the case where there is a lot of deformation of the anatomy, it may be difficult to map the center of a voxel in the secondary image set to the center of a voxel in the reference due to changes in the voxel shape and size. In this case interpolation methods can be used to map the dose back to the reference. In this method, when accumulating the dose at a point in the reference geometry, its mapped location is found in the secondary image set using the deformable registration and the dose to that point is interpolated from neighboring voxels.^{117,123} This method has been reported in several studies.^{124–126} However, in regions with steep dose gradients and large deformations, this interpolation method may lead to inaccuracies.^{124,126} Illustrations of commonly used dose mapping methods are shown in Figure 3.2.

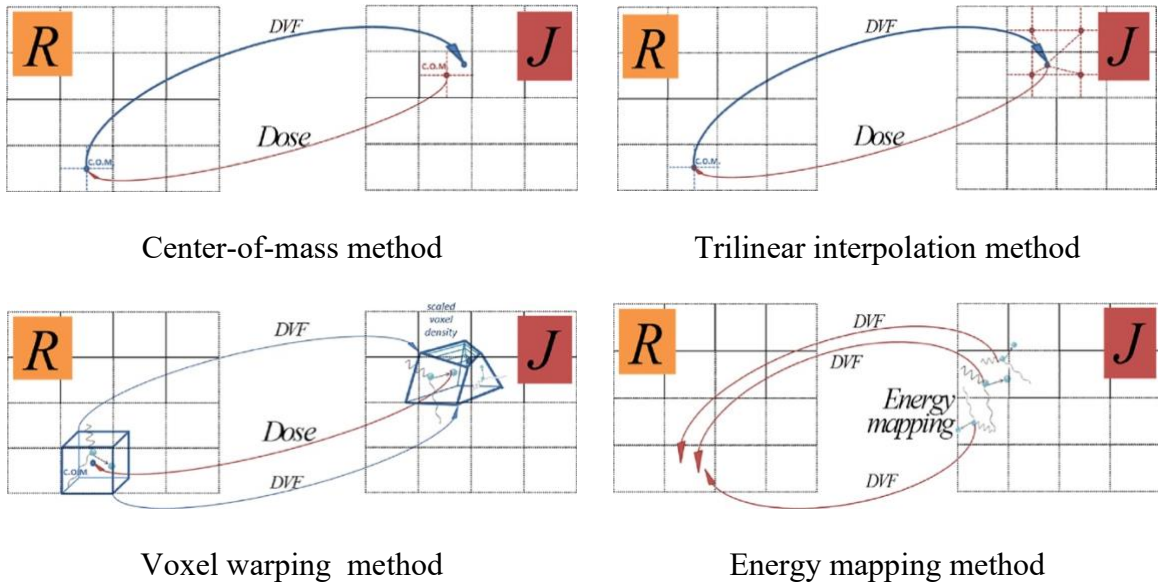


Figure 3.2: Illustration of dose accumulation methods. Figures reprinted with permission from Chetty et al.¹²³

3.5.2 Energy mapping and voxel-warping methods

To mitigate the inaccuracies observed with dose-mapping and interpolation methods, voxel warping and energy mapping methods have been proposed.^{127–129} In energy mapping methods, energy, instead of dose, is mapped from the secondary to the reference phase. Energy deposition calculations occur on a standard rectilinear grid in the secondary phase and the energy deposited in each voxel is mapped back to the reference phase using the deformation vectors from a deformable image registration.¹²⁸ The dose is then calculated using the mapped energy and the mass of the reference voxel.¹²⁸

Another energy conserving method, called the voxel warping method (or direct voxel tracking), was proposed by Heath et al¹²⁶ and implemented in a modified version of the

DOSXYZnrc user code called defDOSXYZnrc. Instead of mapping the dose to a reference grid from a secondary image set, the reference calculation grid is warped according to the deformation vectors that describe respiratory motion at each phase of the respiratory cycle. The dose deposition is then calculated on the warped calculation grid. This method uses a calculation grid of irregular dodecahedron voxels as opposed to a rectilinear grid and the densities of the deformed voxels are adjusted to ensure that mass is conserved.¹²⁶

3.6 4D dose reconstruction methods

Up to this point, the discussion has included only methods that model dose deformation and blurring, however, to model the full effects of motion during radiation treatment the real-time interplay between target motion and the dynamic components of the linear accelerator must be accounted for.

In a study by Litzenberg et al, a dose reconstruction method was proposed that would account for the effects of patient motion during IMRT treatments by synchronizing real-time patient position measurements and machine configuration data.¹³⁰ In this method, the time point during beam delivery is sampled during a Monte Carlo simulation and is used to determine the machine configuration and patient position at that instance, the particle is then transported under these conditions.¹³⁰ The real-time position was measured with the Calypso electromagnetic positioning device and the machine configuration data (MLC positions) was extracted from machine log files.¹³⁰ It should be noted that this method simulated only rigid translations of the patient.

Another dose reconstruction method by Belec et al¹³¹ used the energy mapping method to model dose delivery from VMAT treatments in the presence of continuous organ motion. A randomly generated time variable represented by the cumulative number of MU delivered was generated to sample the position of the dynamic components in the linear accelerator for each particle history in the simulation.¹³² Continuous deformation of anatomy was accounted for by using the time variable to also sample the density of each voxel in the calculation grid at that point based on deformable image registration vectors. The calculation was then carried out on the modified grid and the energy was mapped back to the reference phase.¹³¹

Poulsen et al.¹³³ validated a 4D dose reconstruction method that incorporates delivery information from log files and target motion in a lung phantom. During treatment, tumor motion was tracked with either internal fiducials or with an external surrogate such as the RPM system. The start of treatment was synchronized to the start of the motion measurements and the motion was recorded throughout the treatment. Post treatment, log files were extracted which contained gantry and MLC position data as well as information on the number of MUs delivered at each control point. The motion trace of the target was divided into position bins and sub beams were constructed which represented the portion of the treatment delivery which occurred while the target was in each position. The isocenter of each sub-beam was then shifted to model the change in position of the target and all beams were combined in the TPS.¹³³

Other dose reconstruction methods that recalculate all or part of a treatment on different respiratory phases based on a measured respiratory trace and accumulate them on a reference phase have been proposed.^{134–137} In a study by Chan et al¹³⁴ real time beam tracking data were used to reconstruct the dose delivered to lung cancer patients during Cyberknife SBRT treatments. To model the beam movements during treatments, the planned treatment beam segments were shifted in the TPS according to the tracking data and the plan was recalculated on all of the breathing phases from 4D-CT. Then the doses from all of the phases were accumulated on a reference phase using a deformable image registration¹³⁴. When comparing calculations done with a Monte Carlo code, changes in the volume of the GTV receiving the prescribed dose differed from the static planning calculation by an average of $5.2 \pm 8.8\%$.¹³⁴

A method that divided beam delivery according to the phases of the respiratory cycle was used by both Rao et al¹³⁵ and by Zou et al¹³⁶ in retrospective studies of lung cancer patients. It should be noted that the Rao study used treatment plans to calculate 4D distributions, while the Zou study used beam information from delivery log files to reconstruct the doses delivered. 4D doses were calculated by associating times in each planned beam segment with a respiratory phase and determining the number of monitor units delivered while the target was in each phase^{135,136}. Subsequently, new plans were created on each respiratory phase that modeled the beam delivery that occurred while the target was in each phase of motion.^{135,136} The doses from each plan were then accumulated on a single reference phase using deformation vectors.^{135,136} No motion measurements were taken during treatments, instead the respiratory traces measured

during planning CT were used for the simulations.^{135,136} It should be mentioned that the assumption that motion does not vary significantly during treatment from what was observed during planning CT is not always valid. Changes in respiratory motion during treatments has been shown by several researchers.^{16,24,25} The Rao study compared the 3D to the 4D dose calculations and showed that there was, on average, a 1% reduction in dose to the GTV.¹³⁵ The Zou study showed a 5% average reduction in the V105% of the PTV and a less than 1.5% reduction in the PTV V95% and V90% when considering the 4D reconstructed doses.⁵³

Recently, a workflow was published by Freislederer et al¹³⁷ that combined measured patient breathing traces and machine log files to reconstruct the dose delivered to patients for each treatment fraction. The prescribed dose to these patients was 40.5 Gy to the 65% isodose line over 3 fractions for 4 of the 5 patients studied and to the 80% isodose line for the fifth patient. Motion traces were acquired during each treatment fraction using the laser-based surface scanning C-RAD system.¹³⁷ These motion scans were synchronized during measurements to the beam- on- time of the treatment.¹³⁷ The breathing traces were then sampled and divided to correlate to the different respiratory phases from the planning 4D CT.¹³⁷ Using the log files, the treatment was divided according to the delivery that occurred while in each respiratory phase. Then individual plans were created and dose was calculated for each respiratory phase.¹³⁷ The doses were then accumulated on the exhale phase using dose mapping. This study showed only small differences in target coverage in a VMAT plan when comparing the 4D calculated doses to the doses planned on the average-CT (mean change in D98% of 0.8 ± 1.8 Gy).

3.7 The 4Ddefdosxyznrc reconstruction tool

In this work, the 4DdefDOSXYZnrc user code was used to reconstruct the dose delivered to patients during radiation therapy delivery. The 4DdefDOSXYZnrc user code is a modification of the previously mentioned defDOSXYZnrc code.¹²⁹ In 4DdefDOSXYZnrc, the previously mentioned source 21²⁷ is used to synchronize the dynamic collimator and gantry settings of the linear accelerator for each incident particle to the respiratory phase of the patient at that time.¹³⁸ This code has been experimentally verified in both rigid¹³⁹ and deforming¹⁴⁰ phantoms. Using the voxel warping method from the defDOSXYZnrc code, the 4DdefDOSXYZnrc code simulates a continuously deforming patient anatomy.

Figure 3.3 shows the main steps of how 4DdefDOSXYZnrc models dynamic delivery using log files and a respiratory trace. For each incident particle, the MU index that is sampled to specify the machine parameters also specifies the deformation of the anatomy at that point. The respiratory trace is normalized yielding scaling factors that are used to scale a single set of deformation vectors that describe the respiratory motion between the exhale and inhale state. The minimum scaling factor corresponds to the reference phase and the maximum is assigned to the phase the deformation was performed to. The scaled deformation vectors are then used to warp the dose calculation geometry and the energy deposition of the current particle history is scored in the deformed geometry.

In the first experimental verification of 4D dose reconstructions using the 4DdefDOSXYZnrc code a rigidly moving phantom, the Quasar respiratory motion

phantom (Mobus Medical, London, ON, Canada), was used. The lung insert in the phantom contained a 3 cm diameter sphere to mimic a lung tumour.¹³⁹ The phantom simulated 1-dimensional sinusoidal respiratory motion of the tumour. A static field and VMAT treatment were delivered to the phantom. The dose delivered to the tumour was measured with Gafchromic film and the RADPOS sensor which were both placed in the centre of the tumour during beam delivery.¹³⁹ During irradiation the motion of the tumour was measured with the RADPOS system and the motion trace was used in the 4Ddefdosxyznrc simulation.¹³⁹

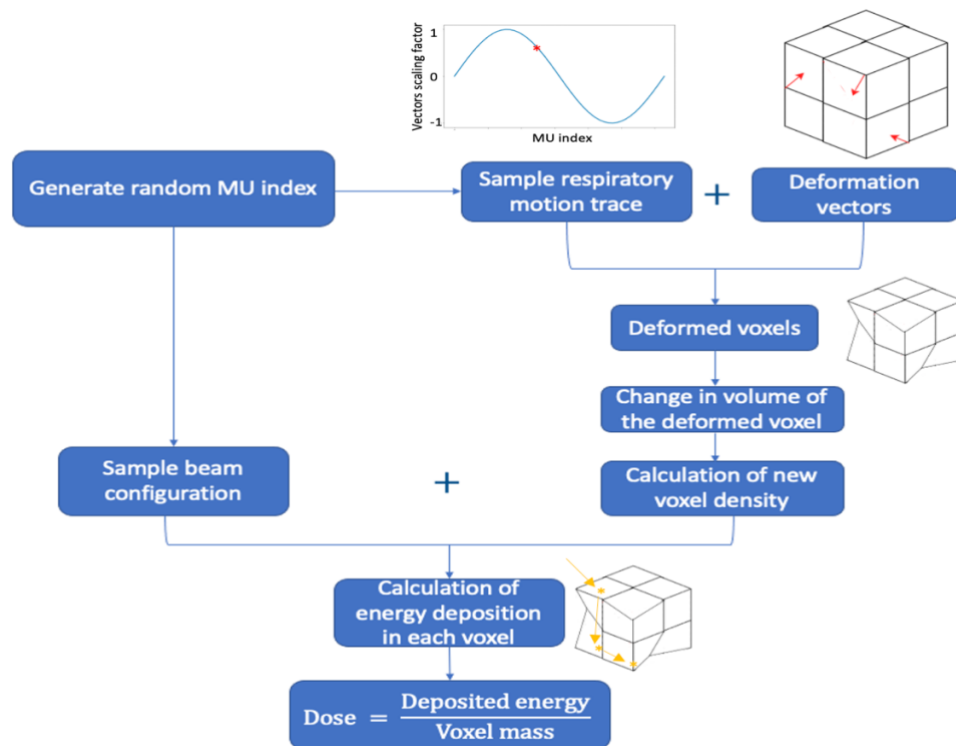


Figure 3.3: Flowchart illustrating the steps of the 4Ddefdosxyznrc reconstruction. Redrawn from Gholampourkashi.¹⁴¹

The simulated dose agreed with both the film and RADPOS measurements within experimental uncertainties in the case of both the static and VMAT fields.¹³⁹

In the follow up study, a deformable phantom was developed to more accurately replicate lung motion for the purpose of validating the 4Ddefdosxyznrc dose reconstruction in a deforming anatomy.¹⁴⁰ In contrast to the previous Quasar study, a deformable image registration was applied to the end-of-inhale and end-of-exhale CT image sets to represent the respiratory motion and was used to deform the voxels of the exhale phase during the simulation.¹⁴⁰ The image registration vectors were calculated in Velocity AI (Varian Medical Systems, Palo Alto, CA, USA) which employs a modified B-spline algorithm for the calculation of image registration vectors. The results of the 4Ddefdosxyznrc calculation were compared for static and VMAT plans. The reconstructed doses agree with both film and RADPOS measurements.¹⁴⁰

Chapter 4: Application of 4D dose reconstruction to patients

4.1 Description of patient group

This study was approved by both the Ottawa Hospital and Carleton University research ethics boards and consent was given by all study participants prior to the collection of any data or measurements. The consent form signed by patients prior to their enrollment in the study can be found in the Appendix. Three patients were recruited for this study and will be referred to as Patients 1, 2, and 3. A description of the treatment parameters for each of these patients is described in Table 4.1 and a coronal views of each patient's CT scan are shown in Figures 4.1-4.3.

Table 4.1: Summary of treatment parameters for the patients recruited in this study. The tumour volumes cited are those which were contoured by a physician on the AVG-CT scan.

Patient #	Tumour location	Tumour volume/ cm^3	Treated lymph node volume/ cm^3	Fractional dose/cGy	Number of treatment fractions	Total prescribed dose/cGy	Total number of VMAT arcs
1	Right lobe	802.480	No lymph nodes treated	200	28	5600	2
2	Upper right lobe	8.483	48.590	200	30	6000	3
3	Left lobe	87.159	24.210	200	30	6000	2

All three patients were treated according to the TOHCC curative standard #3, for locally advanced/ radical non-small cell lung cancer. This treatment protocol consists of a VMAT treatment planned on the average-CT scan, wherein 200 cGy are prescribed to be delivered per fraction. The number of prescribed fractions for each patient varied based

on prior treatments and ranged from 28 to 30 daily fractions. The treatments consisted of multiple arcs ranging from 2-3, depending on the patient. Patient 3 was treated with abdominal compression during treatment, which can be seen on the lateral CT slice shown in Figure 4.4.

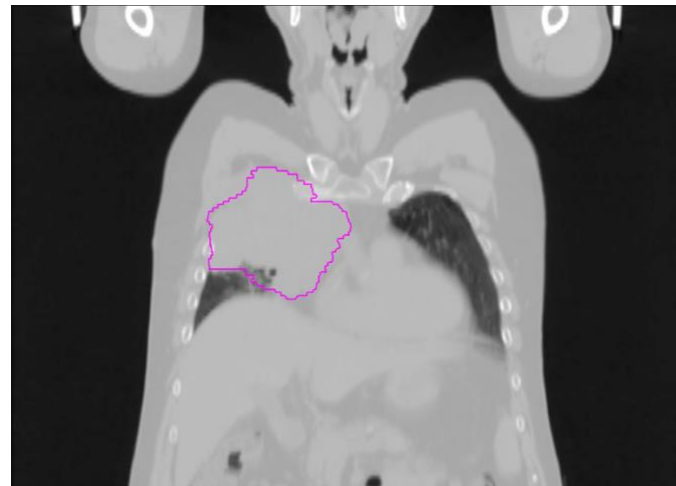


Figure 4.1: GTV contour of Patient 1 outlined in pink, as seen on the average-CT image at the location of the treatment isocenter.



Figure 4.2: Tumor and node contours of Patient 2 in blue and pink respectively on the average-CT image at the location of the treatment isocenter.

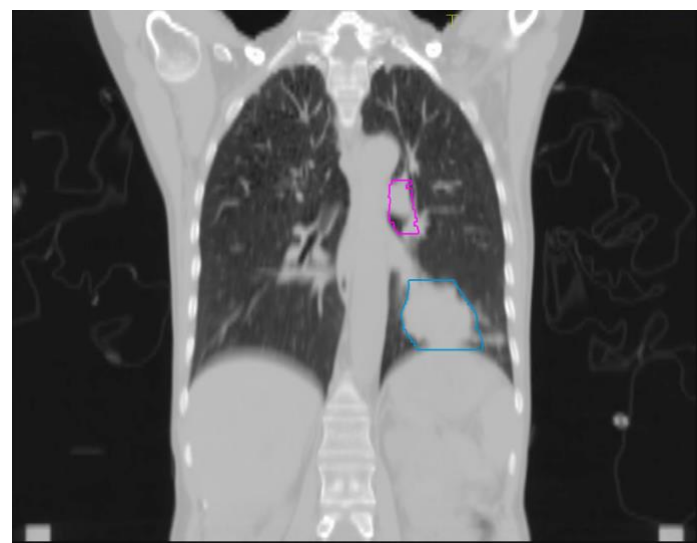


Figure 4.3: The treated lymph nodes and contoured tumor volume for Patient 3, outlined in pink and blue respectively, on the average-CT image.

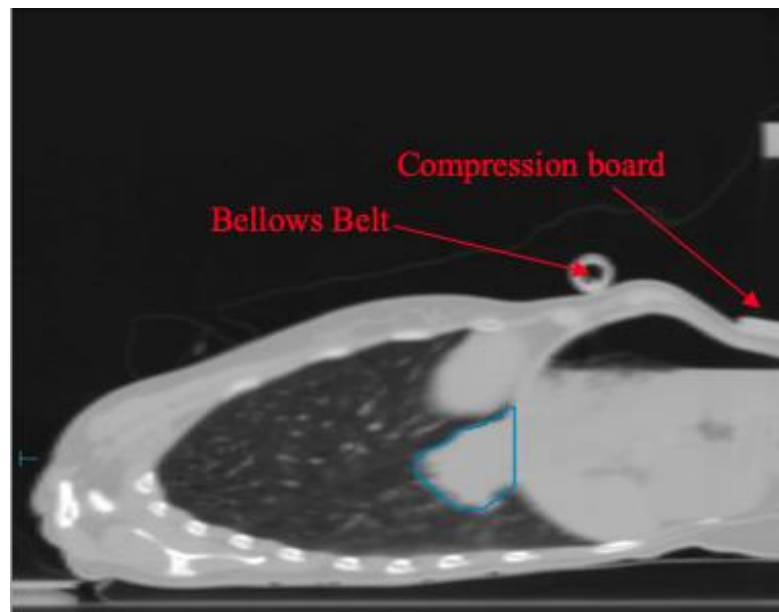


Figure 4.4: Lateral view of Patient 3, with tumor outlined in blue and location of the abdominal compression board, which minimizes patient motion during treatment, indicated by red arrow.

4.2 4D reconstruction framework

The key steps in the reconstruction process are outlined in Figure 4.5

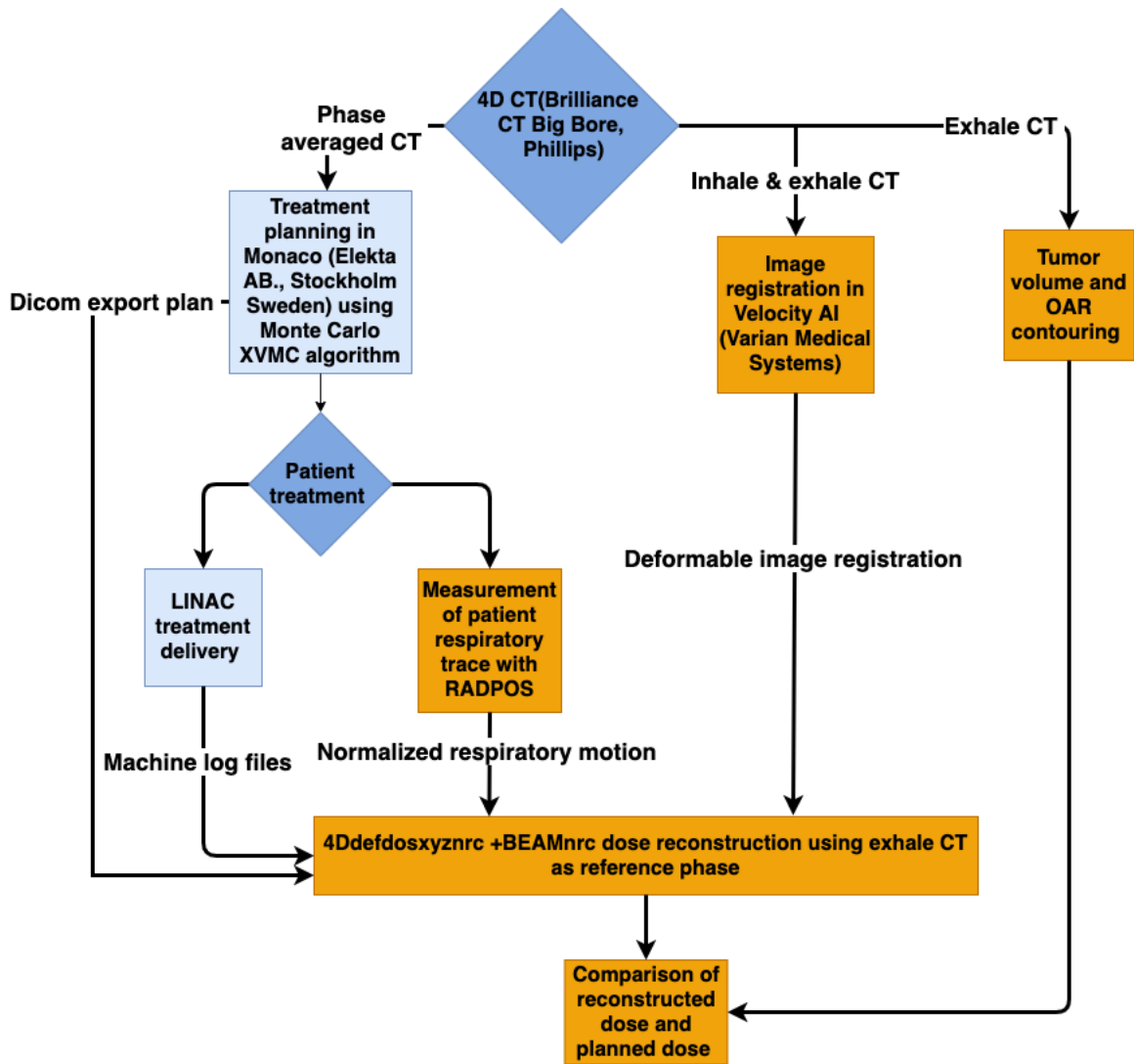


Figure 4.5: Outline of the 4D reconstruction framework. Steps in blue are those that would normally occur in the course of a patient's treatment, steps directly involving patients are filled with a darker hue. The steps outlined in orange are additional steps required for the 4D reconstruction.

4.2.1 4D-CT Acquisition

The typical patient treatment planning process would begin with a 4D-CT scan acquisition. For the patients in this study, the Big Bore helical CT scanner (Brilliance CT Big Bore, Phillips, Amsterdam, Netherlands) was used for 4D-CT acquisition. Patients were imaged in the head-first supine position using a helical acquisition with a peak kilovoltage of 120, a pitch factor of 0.08 and a rotation time of 0.44 s. The scan covers the region from the jaw to the bottom of the liver and has a slice spacing of 3 mm as per the TOHCC planning standard. Before the scan acquisition the patients are fitted with the Philips Bellows pneumatic belt (Philips Medical Systems, Cleveland, OH) to measure the movement of the patient's surface throughout the scan and correlate this respiratory motion to the scan acquisition. Based on this measured surface motion the images are sorted into 10 respiratory phases (0%-100%) where 0% corresponds to the end-of-inhale phase. At the location of the Bellows belt, a tattoo was placed on the patient's abdomen to mark the location for the RADPOS sensor which would be used for the motion measurements during treatments. For Patients 1 and 2 this was on the abdomen superior to the umbilicus. Due to the use of the compression board for Patient 3 this tattoo was placed on the left side of the patient at the level of the Bellows belt.

4.2.2 Image Registration

The 4D reconstruction process begins with an extraction of the CT images from the treatment planning 4D-CT. The CT images are binned according to respiratory phase into 10 image sets ranging from 0% to 100%. The end of inhale and end of exhale phases are identified for use in the image registration process, these phases are generally labeled as the 0% and 50% phases respectively. A deformable image registration¹⁴² is performed between these two phases in Velocity AI 3.2.1 (Varian Medical Systems, Inc., Palo Alto, CA, United States of America). Velocity employs a B-spline algorithm. This algorithm starts with superimposing a sparse grid of control nodes over the two images to be registered. The algorithm then warps the positions of these control nodes and interpolates the displacements of the other image points. The similarity of the two images is assessed by calculating their mutual information. This procedure is repeated until the mutual information is maximized.¹⁴³ Two deformable registration settings were used in this work, the first is an extended deformable multipass registration, which consists of consecutive registrations at 6 progressively finer resolution steps. The second is a coarser, multipass registration, which uses only 3 resolution steps. The 6-pass extended registration was initially applied to all the patient image sets. However, the use of the finer resolution registration when applied to the second patient yielded discontinuities in the deformation vectors used in the 4D simulation and therefore the coarser 3-pass registration was used instead. Discontinuities in the deformation vector field imply that individual deformation vectors overlap which leads to a tearing and inverting of the geometry to which they are applied. Discontinuities in the DVFs were detected by computing the Jacobian determinant of the DVFs.¹⁴⁴ The deformation vector fields

resulting from the registrations were exported as binary data files and downsampled in both the left-right and the anterior-posterior directions to a voxel size of $3 \times 3 \times 3 \text{ mm}^3$ to match the resolution of the dose calculation grid used in the TPS. An example of the deformation vectors for Patient 2 are shown in Figure 4.6.

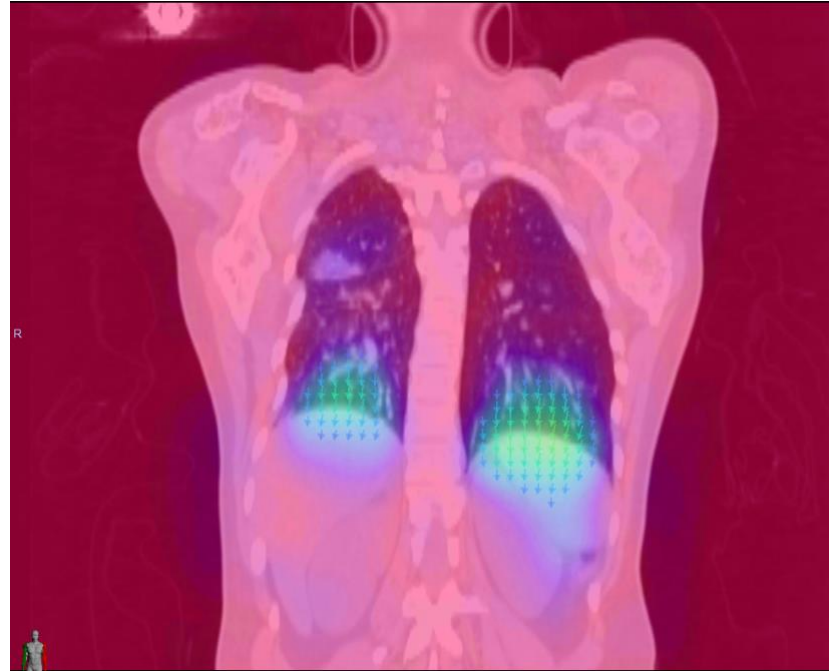


Figure 4.6: Example of deformation vectors generated for Patient 2 using the deformable multipass registration. The color wash indicates the magnitude of motion, the brightest areas denote larger magnitudes of motion, and the arrows indicate the direction of motion.

4.2.3 Tumour volume and OAR contouring

The GTV and organs at risk are typically contoured by the physician on the AVG-CT. The AVG-CT is the CT scan representing the average image intensity at each voxel from the 10 phase-binned image sets⁶¹. In the case where lymph nodes were treated, the tumour and the nodes were contoured separately, as GTV and GTVn, respectively. A 5 mm margin is added to the GTV and GTVn to create the CTV.

For this work, the exhale CT images were also sent to a radiation oncologist to be contoured for use in the analysis of the reconstructions and comparison to the TPS planned dose. The physician contoured the GTV, GTVn (when lymph nodes were treated), the esophagus, bronchi proximal, the liver, the heart and both lungs in addition to the patient's external. A 5 mm margin was added to the GTV only to create the CTV. This was also done on the AVG-CT such that the same two volumes were being compared when considering the dose metrics.

4.2.4 Patient measurement setup

Respiratory motion measurements with RADPOS were taken at the time of patient treatment. A schematic drawing of the RADPOS measurement setup is shown in Figure 4.7. Prior to the measurements the clock of the computer on which RADPOS measurements were recorded was synchronized with the time.windows.com internet time server to match the time server used on the linac. During patient setup, the RADPOS detector was taped at the location of the tattoo made during 4D-CT. The receiver of the RADPOS detection system was placed on a plastic stand attached to the treatment couch at the 'E' location and the hexapod frame was placed at location 'F' on the couch as can be seen in Figure 4.7.

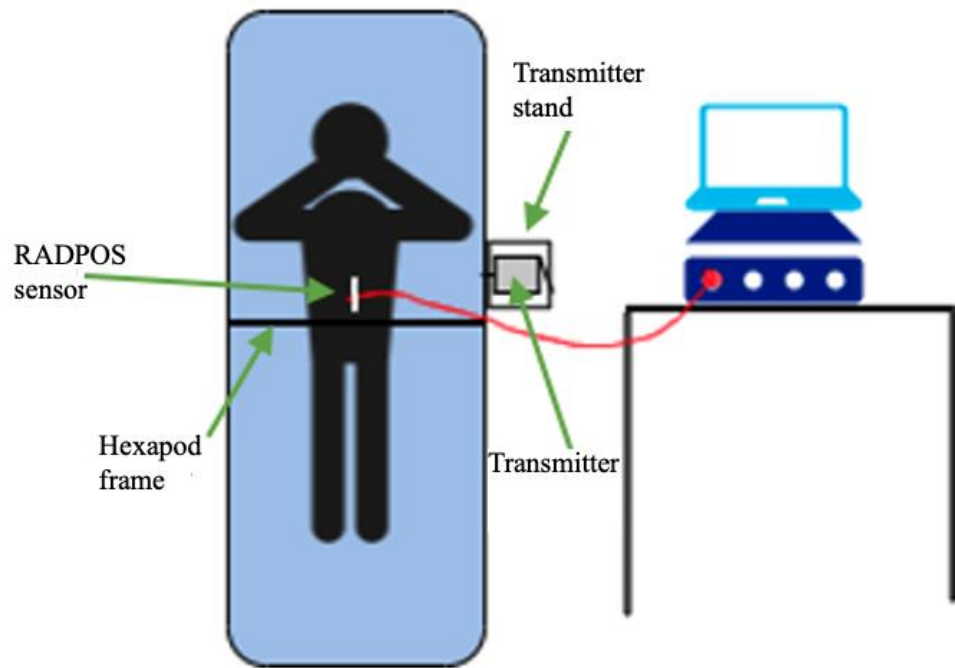


Figure 4.7: Schematic drawing of patient RADPOS measurement setup.



Figure 4.8: Patient setup without placement of RADPOS sensor. The hexapod frame is located at slot 'F'.

After the sensor was secured to the patient abdomen and the receiver placed on the treatment couch, the gantry of the LINAC was rotated to ensure that it would clear the RADPOS system. The RADPOS measurements were started at the end of the patient setup and the patient position was sampled at a frequency of 100 ms (10 Hz) throughout the treatment. The individual RADPOS measurements provide the X, Y and Z components of the sensory displacement measured relative to a point in the RADPOS transmitter.

4.2.5 4Ddefdosxyznrc simulation parameters and input file generation

After treatment, the corresponding machine log files were extracted and decoded using the open source pymedphys python library (<https://github.com/pymedphys/pymedphys>). These log files contain treatment delivery information including delivered monitor units, multi-leaf collimator and jaw positions and gantry angle at a resolution of 0.04s. For each control point in the treatment delivery these settings were synchronized with the measured patient motion using the beam off time encoded in the machine log files. The beam start time is calculated by subtracting the length of the treatment time from the beam off time which is recorded in the log file as the ‘UTC time’. The point in the motion measurements corresponding to this time is located and the ‘delay time’ between the start of the motion measurements and the beam on time is calculated. For each control point in the log file the ‘elapsed time’ in the log file corresponds to the ‘delay time’ + ‘elapsed time’ in the motion measurements file. A python script was used to read the measured patient position at the time of each control point in the log file by applying this

time synchronization method. The DICOM RTPlan file was also required to get the treatment isocenter coordinates.

The dose calculation geometry was generated from the exhale CT set. The Hounsfield units stored in the exhale CT DICOM files were converted to mass density using the calibration curve for the Big Bore CT (Brilliance CT Big Bore, Phillips, Amsterdam, Netherlands) which is shown in Table 4.2.

Table 4.2: Calibration curve used to convert CT numbers in HU to mass density in g/cm³

CT Number (HU)	Mass density (g/cm ³)
-1024	0.010
-706	0.280
-535	0.400
-99	0.900
10	1.000
208	1.090
467	1.280
1234	1.690
3520	2.600
5750	3.500
8000	4.380
16000	7.500

An in-house software, ct_tools, was used to convert CT images to egsphant files. A nine material assignment scheme consisting of; air, lung- blood filled, adipose 2, muscle 2, heart- blood filled, cartilage, ribs, and cortical bone was used to define the inside of the external contour. The outside of the patient was defined as air with exception of the treatment couch. A density override was performed to define the inside of the treatment couch as foam with an external carbon fiber frame with densities of 0.080 g/cm³ and

0.408 g/cm³ respectively. This was done to maintain consistency with the protocol used for planning in the clinical TPS. The compositions and mass densities used to define the patient are found in Table 4.3.

Table 4.3: Material composition and density data^{145,146} used to define the dose calculation geometry.

Medium	Mass density (g/cm ³)	Elemental composition				
		H	C	N	O	Other elements
Air (ICRU 700)						
Lung – Blood filled	0.26	10.3	10.5	3.1	74.9	Na(0.2), P(0.2), S(0.3), Cl(0.3), K(0.2)
Adipose 2	0.95	11.4	59.8	0.7	27.8	Na(0.1), S(0.1), Cl(0.1)
Muscle 2	1.05	10.2	14.3	3.4	71.0	Na(0.1), P(0.2), S(0.3), Cl(0.1), K(0.4)
Heart- Blood filled	1.06	10.3	12.1	3.2	73.4	Na(0.1), P(0.1), S(0.2), Cl(0.3), K(0.2), Fe(0.1)
Cartilage	1.1	9.6	9.9	2.2	74.4	Na(0.5), P(2.2), S(0.9), Cl(0.3)
Ribs	1.41	6.4	26.3	3.9	43.6	Na(0.1), Mg(0.1), P(6.0), S(0.3), Cl(0.1), K(0.1), Ca(13.1)
Cortical bone	1.92	3.4	15.5	4.2	43.5	Na(0.1), Mg(0.2), P(10.3), S(0.3), Ca(22.5)

Static Monte Carlo simulations of the treatment plan were completed using a combination of the BEAMnrc/EGSnrc and DOSXYZnrc/EGSnrc user codes on the AVG- and exhale-CT. A summary of all static and 4D reconstructions completed is given in Table 4.4.

Table 4.4: Summary of Monte Carlo calculations completed in this work.

Simulation Type	Usercode	CT images used for .egsphant file	Source of Simulation Parameters
Static- Clinical plan	DOSXYZnrc	AVG-CT	DICOM RT Plan
Static- Exhale	DOSXYZnrc	Exhale-CT	DICOM RT Plan
4D	4Ddefdosxyznrc	Exhale-CT	Log File + RADOS trace

For each control point in the treatment plan the gantry and collimator angle, MLC and jaw openings and the cumulative monitor units were read in from the DICOM RTPlan file.¹⁴⁷ The gantry, couch and collimator angles were transformed from the DICOM to the BEAMnrc coordinate system according to the transformations outlined in Zhan et al.¹⁴⁷ A previously validated BEAMnrc model⁸⁷ of the 6 MV beam of the Elekta Infinity linac with Agility MLC was used. The DOSXYZnrc source 21, which uses a BEAMnrc linac model as the particle source was used. This source allows for the synchronization of the BEAMnrc and DOSXYZnrc simulations by sampling the relevant simulation parameters based on a randomly generated monitor unit index between 0 and 1. In this case, the SYNCMLCE and SYNCMLCQ component modules were used to model the dynamic MLC and jaws of the linac and allow for the synchronization of the MLC and jaw positions in the BEAM simulation with the gantry angle in DOSXYZnrc. The Monte Carlo plan simulations were performed on the AVG-CT to be consistent with the clinical plans.

The 4D reconstructions were completed using the 4DdefDOSXYZnrc/EGSnrc user code. Like the DOSXYZnrc simulations, source 21 was used to synchronize the beam motion with the patient motion. The same BEAMnrc model was used for DOSXYZnrc and 4DdefDOSXYZnrc simulations. Accelerator parameters such as MLC and jaw openings and gantry and collimator angles were read in from the machine log files. The gantry and collimator angles were transformed to the BEAMnrc coordinate system using the previously mentioned transformation described by Zhan et al.¹⁴⁷ MLC and jaw opening

were calculated using the geometric relationship describing field sizes at different distances from the source.

To generate the input files for the 4D reconstructions, log files, patient motion traces (from RADPOS) and the deformation vectors are required. The motion measurements are synchronized and resampled to the log file resolution using the previously mentioned method. The respiratory motion amplitude at each time point is normalized and is written in the 4Ddefdosxyz input file. Ideally, the motion traces from RADPOS should be normalized to surface motion measured during the 4DCT acquisition in order to scale the deformation vectors obtained from registration of the 4DCT exhale and inhale images. The surface motion at the time of 4DCT was measured using the Bellows belt. However, a calibration coefficient to convert the Bellows trace data to centimeters was not available.

Instead, two different normalization approaches were investigated: (1) 3D normalization; and (2) A/P normalization, which are described in the following paragraphs. The two different strategies were investigated to test the sensitivity of the reconstruction to the normalization method.

The 3D normalization, called ‘3D norm’, involved normalizing the 3D displacement for each fraction to the average peak-to-peak amplitude of the 3D displacement measured on the first fraction. For each fraction trace, the 3D displacement, $R(i)$, at a given timepoint was calculated from the measured LR, AP and SI components at the same timepoint.

$$R(i) = \sqrt{AP(i)^2 + LR(i)^2 + SI(i)^2} \quad (4.1)$$

Using Python's built-in peak-finding algorithm, the peaks and valleys in the R trace for each fraction were identified. The peak-to-peak displacement for each respiratory cycle was calculated from adjacent peaks and valleys and the average value ($\overline{\Delta R_{PP}^{Fx_1}}$) for the first fraction trace was calculated. The average of the minima ($\overline{R_{min}^{Fx_X}}$) was also calculated and subtracted from each fraction (Fx_X) trace prior to the normalization to remove the inter-fraction position offsets. A more detailed discussion of the reasoning for this is provided in section 5.1.1. The vector scaling factor (R_{norm}) for a given fraction X is then given by equation 4.2:

$$R_{norm}^{Fx_X}(i) = \frac{R(i) - \overline{R_{min}^{Fx_X}}}{\overline{\Delta R_{PP}^{Fx_1}}} \quad (4.2)$$

For the A/P normalization, called 'AP norm', only the A/P component of the RADPOS displacement was used and it was normalized to the A/P displacement of the fiducials on the patient's surface measured from the inhale and exhale phases of the 4D CT, as shown in Figure 4.9. This was only implemented for Patient 2 because the 4D-CT scan for Patient 1 did not span inferior enough to view the Bellows belt in the CT images. Similar to the 3D-norm method, the peaks and valleys in the AP component of the RADPOS trace were identified for each fraction. The average of the minima ($\overline{AP_{min}^{Fx_X}}$) was also calculated and subtracted from each fraction trace prior to the normalization by the 4DCT amplitude (ΔAP_{4DCT}). The vector scaling factor ($AP_{norm}^{Fx_X}$) at each timepoint were calculated from equation 4.3:

$$AP_{norm}^{Fx_X}(i) = \frac{AP(i) - \overline{AP_{min}^{Fx_X}}}{\overline{\Delta AP_{4DCT}}} \quad (4.3)$$

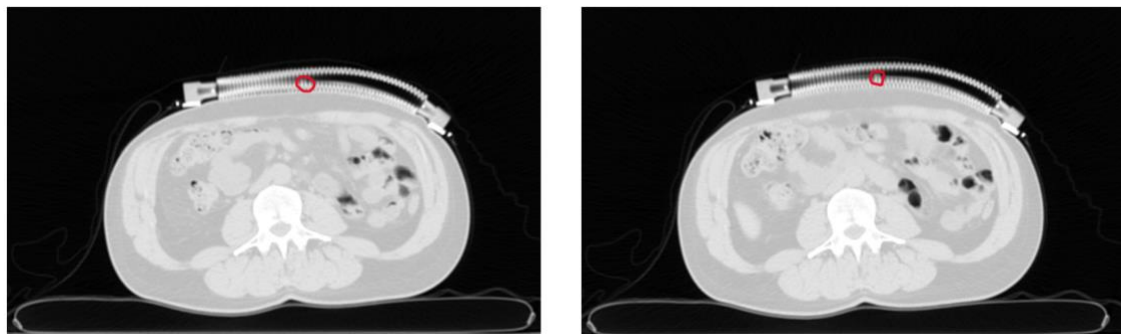


Figure 4.9: On the left is a slice from the exhale phase CT of Patient 2, on the right is the same slice from the inhale phase. The change of the position, along the A/P direction, of the fiducial circled in red is measured and used to normalize the patient motion measured with RADPOS.

All Monte Carlo simulations were executed on the Carleton Research Computer Cluster which is composed of 644 Intel Xeon cores with a speed of 3.00 GHz. For all of the simulations, the electron transport cut-off energy, ECUT was set to 1.011 MeV and the photon transport cut-off energy, PCUT was set to 0.05 MeV, to maintain consistency with the dose calculation performed in Monaco. The boundary crossing algorithm was set to ‘EXACT’. The Bound Compton scattering parameter was turned off, treating Compton scattering with Klein-Nishina coefficients and the photon cross sections used were from the XCOM database. All other settings were consistent with the default setting for DOSXYZnrc.¹¹²

The uncertainty for each simulation was calculated using the method recommended in the AAPM TG 105 report.¹⁴⁸ The uncertainty reported is the root mean square of the uncertainty of the dose in voxels with more than 50% of the maximum dose. The number of histories varied for each simulation and was adjusted to achieve an uncertainty less than or equal to 1%. For the 4D reconstructions, a separate simulation was performed for

each individual beam in the treatment and the resulting 3ddose files were summed to model the full reconstruction. After summing the individual beams, the dose in the couch structure was zeroed in the summed 3ddose files. For Patients 1 and 2 the total number of histories simulated for the 4D reconstructions were 300 million and 240 million respectively.

4.2.6 Dose metric comparison

Analysis of the 3ddose distributions was done using CERR, the Computational Environment for Radiological Research¹⁴⁹. Prior to importing into CERR, the dose in the couch structure was zeroed. The exhale CT images and DICOM structure sets were imported into CERR. The .3ddose files from the Monte Carlo simulations were read by CERR. The dose distributions were transformed from DOSXYZnrc to RTOG coordinate systems before being imported into the program. For the 4D reconstructions, the calculated dose from the Monte Carlo simulations was converted to absolute dose according to equation 4.4. The dose for each voxel calculated in 4Ddefdosxyznrc/DOSXYZnrc is normalized to the calibration dose which was calculated for a 10x10 cm² beam incident on water at an SSD of 100 cm and multiplied by the number of monitor units (MU_{del}) delivered. For the 4Ddefdosxyznrc simulations, the delivered MU was extracted from the log files. For the DOSXYZnrc simulations of the plan, the number of monitor units cited in the DICOM RTPlan file was used instead.

$$D(Gy) = \frac{\left(\frac{dose}{primaryhistories} \right)_{4Ddefdosxyz/DOSXYZ}}{\left(\frac{dose}{primaryhistories} \right)_{DOSXYZ \text{ calibration simulation}}} \times 1 \frac{cGy}{MU} \times MU_{del} \times 1 \frac{Gy}{cGy} \quad (4.4)$$

In CERR, the dose volume histograms for the GTV, heart and esophagus were calculated and were exported as text files for analysis. In this work, the D98%, D2%, D50% and V2 Gy (GTV), V.91 Gy, V1.36 and D0.03cm³ Gy (heart) and V1.51 Gy, V1.06, and Dmean (esophagus) of the reconstructed were calculated for comparison with the planned dose metrics from the clinical TPS. For the planned dose calculations using DOSXYZnrc, clinically relevant dose metrics for all OAR and target volumes were compared to the TPS.

Chapter 5: Results

5.1 Patient motion characteristics

5.1.1 Patient 1

The motion components measured for each treatment fraction for Patient 1 are shown in Figure 5.1. The A/P motion was the dominant direction of the respiratory motion.

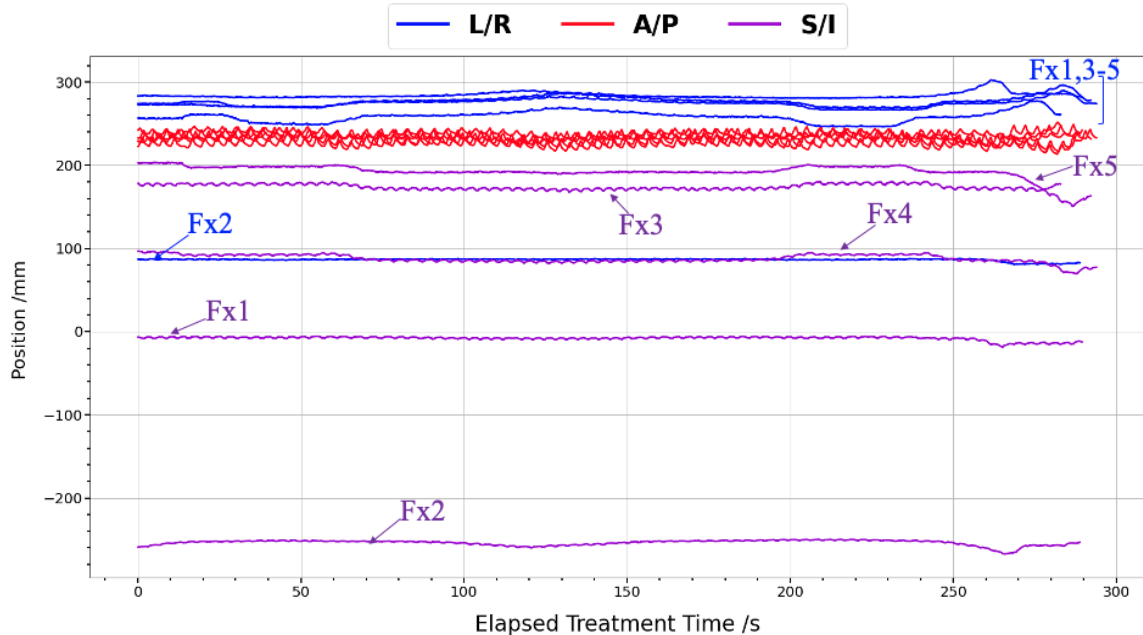


Figure 5.1: Patient 1 motion measurements for 5 treatment fractions, labeled as Fx *, where *
represents the fraction number. The fractions showing the largest position variation are labeled for
the L/R and S/I positions.

While the average A/P position is relatively similar between fractions, significant changes in the S/I and L/R position can be seen between fractions. An inter-fractional difference of 45 cm can be seen in the S/I position between fractions 2 and 5. In the L/R position, shifts up to 20 cm were observed. The position measurements are made relative to a point inside the RADPOS transmitter. The transmitter is placed on a shelf that is reproducibly secured to the treatment couch. Therefore, its position along the A/P axis is

fixed. The RADPOS shelf is only slightly larger than the actual transmitter. However, there is some room for variations in the placement of the transmitter while on the shelf, on the order of less than 0.5 cm. While an effort was always made to center the transmitter on the shelf, small variations in the S/I and L/R position could occur if the transmitter wasn't centered properly. Another explanation for the observed L/R and S/I shifts are inter-fractional differences in the position of the sensor placed on the patient abdomen. Although care was taken to position the sensor to the abdomen in a reproducible way, there were difficulties in securing the sensor due the hair on the patient's abdomen. Additionally, a sheet is placed over the patient prior to treatment. The movement of this sheet may also disturb the RADPOS sensor, inadvertently rotating or shifting the sensor from its intended position. Furthermore, although the location of the RADPOS sensor was marked with a tattoo, any changes in the patients position relative to the transmitter could change the location of the sensor relative to the transmitter. If the patient was rotated or their abdomen was skewed from the center of the couch, variations in the L/R and S/I position on the order of cm would not be improbable. The patient setup is focused on the treated area and the alignment lasers are used to align the patient near the treatment isocenter located on the patient's chest. The RADPOS sensor is placed inferior to this region, on the abdomen. Therefore, variations in the patient position at the location of the RADPOS sensor is not unlikely.

A plot of the 3D, or 'R', position traces measured during each treatment fraction are shown in Figure 5.2. The shifts in the L/R and S/I position are the dominant cause of the shifts in the average minimum position of the 'R' trace. The inter-fractional differences in

both the peak-peak displacement ($\overline{\Delta R_{PP}^{FxX}}$) and the average minimum ($\overline{R_{min}^{FxX}}$) position of the traces can be seen in Table 5.1. The mean of the fraction averaged minimum positions is also reported in Table 5.1. A shift in the minimum position of up to 46 mm was measured between fractions. The mean of the fraction average peak-peak amplitude ($\overline{(\Delta R_{PP}^{FxX})}$) was 5.5 ± 1.4 mm. This patient also presented inter-fractional variations in the fraction average peak-peak amplitude calculated for each fraction. Respiration is highly individual, and inter-fractional changes in respiratory amplitude have been observed by other researchers²⁵, including Cherpak et al¹⁶ who noted variations in amplitudes of up to 8.6 mm between fractions. While the exact reason for these changes is unknown, changes in amplitude could arise from stress and anxiety, pain or difficulty breathing. The respiratory traces seen in Figure 5.2 also display intra-fractional baseline ‘drifts’. These are low frequency changes in the minimum position (exhale points) of the traces. Similar drifts have been reported in lung tumour tracking studies.^{21,150} In the Seppenwoolde study²¹, this was postulated to be due to either changes in patient position or the level of respiration of the patient. For this reason, the drifts were not removed as it is possible they are in fact indicative of respiratory changes.

Table 5.1: Patient 1, 3D position characteristics. The average 3D peak-peak displacement and average minimum position is presented, with the standard deviation, for each fraction.

Patient 1	Fx1	Fx2	Fx3	Fx4	Fx5	Average
Average 3D peak-peak displacement (mm)	6.7 ± 1.4	4.1 ± 0.3	5.2 ± 0.4	7.3 ± 0.9	4.3 ± 0.6	5.5 ± 1.4
Average minimum position (mm)	366.8	353.6	395.2	366.3	399.9	376.4 ± 20.1

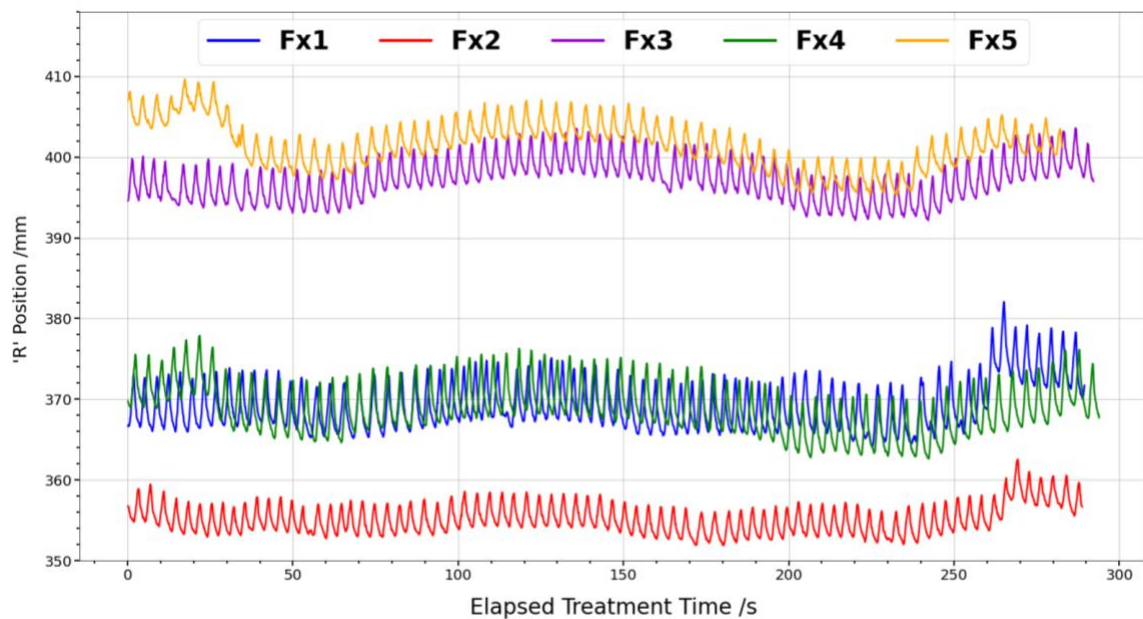


Figure 5.2: Measured 3D position of the abdominal RADPOS sensor during each of the 5 fractions measured for Patient 1. Inter-fractional differences in minimum(exhale) position up to 46 mm are observed between fractions.

Because only 3 patients were recruited for the study and only 2 had measurements viable for the reconstructions, the Patient 1 ‘R’ traces were still used in the 4D dose reconstructions but the offsets in average position were compensated for in the

normalization process subtracting from each trace its own average minimum position

($\overline{R_{min}^{Fx_X}}$). This was done under the assumption that the large inter-fractional offsets in position were due to the RADPOS sensor positioning and changes in patient positioning outside of the target region. Therefore, they should not be modeled in the 4D reconstruction as they were not representative of a change in tumour position.

5.1.2 Patient 2

The inter-fractional position variations for Patient 2 were smaller than for Patient 1 as can be seen from Figure 5.3. Changes in the S/I position up to 11 cm are noted between fractions.

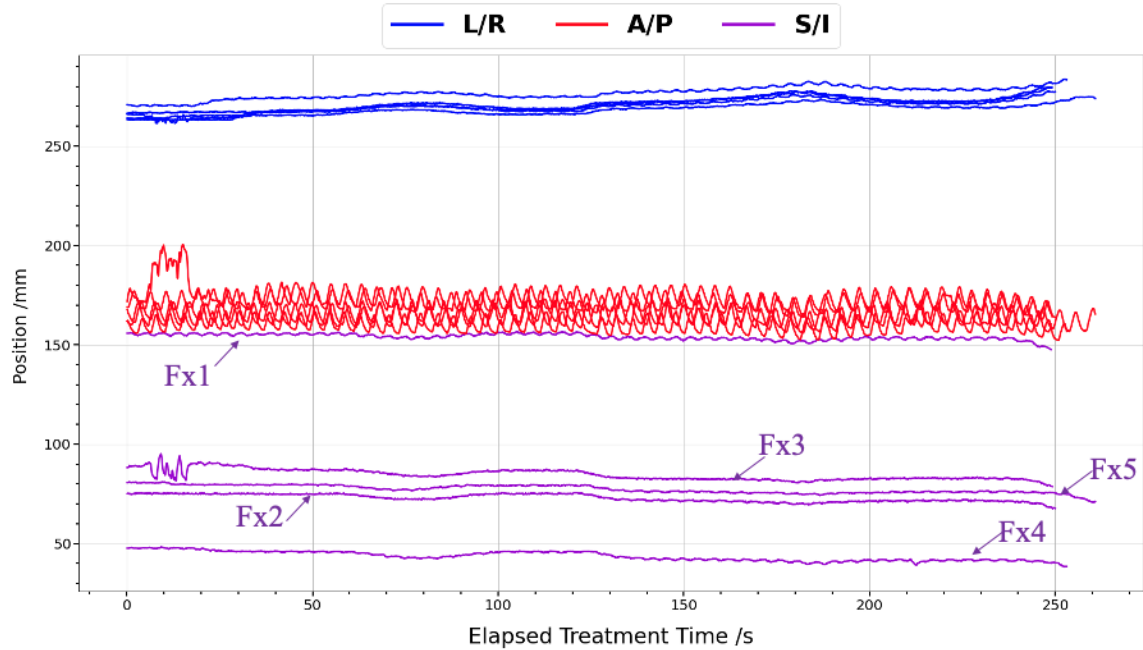


Figure 5.3: Patient 2 motion measurements for 5 treatment fractions. The S/I traces are labeled where there are notable position variations. Changes in position from the first fraction up to 11 cm are noted in the S/I direction.

The ‘R’ position traces for Patient 2 are shown in Figure 5.4 and motion characteristics are given in Table 5.2. For this patient, the mean of average peak-peak amplitude

$(\overline{\Delta R_{PP}^{Fx_X}})$ was 5.4 ± 0.4 mm across all fractions. A second normalization was performed using the A/P motion traces which are shown in Figure 5.5. The mean of average peak-peak displacements along the A/P direction was 10.0 ± 1.2 mm. There were also inter-fractional changes in the average minimum position of the A/P position of up to 13.2 mm. In fraction 3, there is a sharp irregularity in the A/P position, which dominates the R position trace in the first 30 seconds of the treatment. While the exact cause of this change is not known, it is possible that it was due to an abrupt involuntary movement such as a cough, yawn or sneeze which could abruptly change the position of the abdomen.

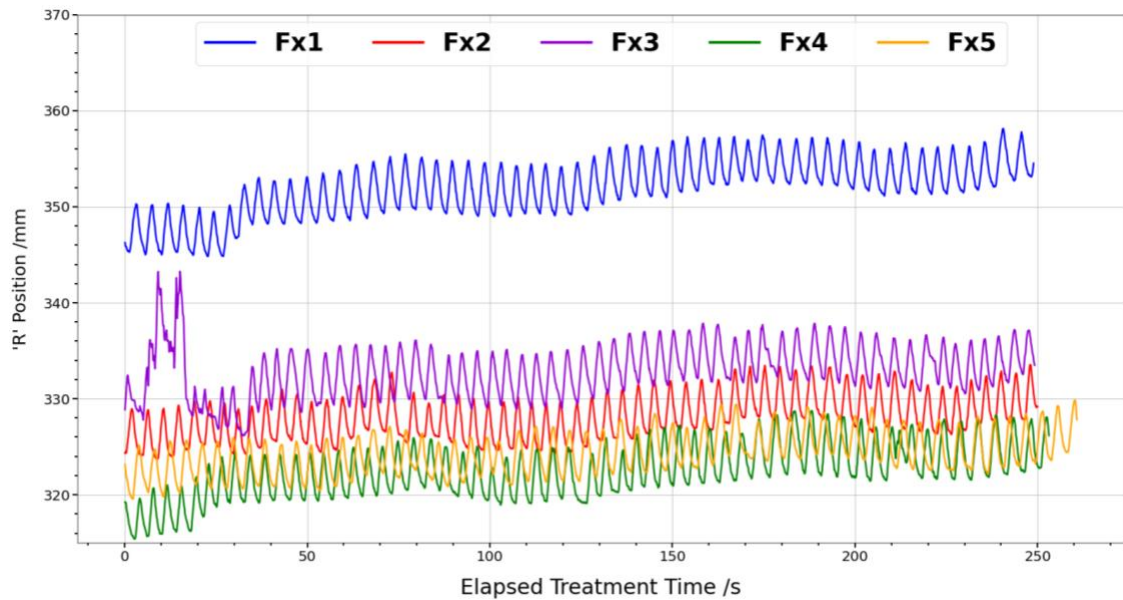


Figure 5.4: Measured 3D position of the abdominal RADPOS sensor during each of the 5 fractions measured for Patient 2. Inter-fractional differences in average minimum position of up to 29 mm are observed between fractions.

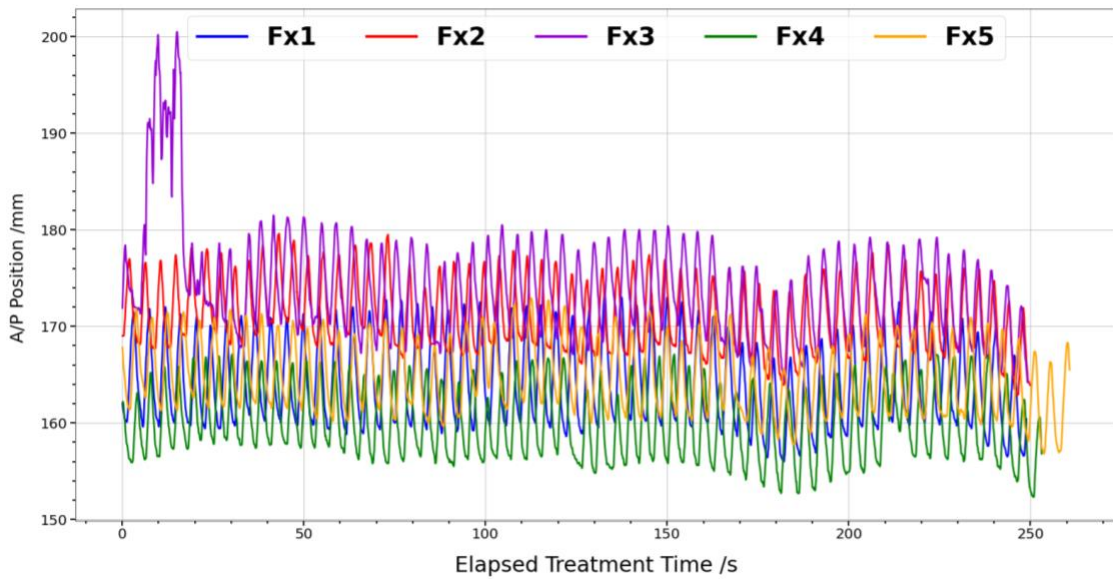


Figure 5.5: Measured A/P position of the abdominal RADPOS sensor during each of the 5 fractions measured for Patient 2. The average peak-peak displacement of all fractions was measured to be 10.0 \pm 1.2 mm.

Table 5.2: 3D and A/P position characteristics measured for Patient 2. The average 3D peak-peak displacement and average minimum position are presented, with the standard deviation, for each fraction.

Patient 2	Fx1	Fx2	Fx3	Fx4	Fx5	Average
Average 3D peak-peak displacement (mm)	5.3± 0.5	5.2±0.4	6.0±2.0	5.0±0.7	5.5±0.8	5.4 ± 0.4
Average minimum 3D position (mm)	349.8	326.0	330.1	322.1	320.2	329.6±11.9
Average A/P peak-peak displacement (mm)	11.8± 1.5	8.9±1.5	10.6±2.5	9.3±1.7	9.4±1.1	10.0±1.2
Average minimum A/P (mm)	159.2	167.5	169.2	156.0	160.6	162.5±5.6
A/P fiducial displacement measured from 4D CT images: 6.45 mm						

5.1.3 Patient 3

Patient 3 also showed large inter-fractional baseline position shifts as can be seen in Figure 5.6. Due to the abdominal compression used during measurements, the 3D motion amplitude was very small, under 1 mm displacement peak-peak for both fractions as shown in Figure 5.7A. The small amplitude of motion yielded a very noisy position trace because of a low signal-to-noise ratio. Additionally, there was a large shift in the baseline position near the end of treatment for both fractions. The motion traces for Patient 3 were deemed unsuitable for use in the 4D dose reconstructions because, when normalized to the peak-peak displacement, they resulted in unrealistically large scaling factors that caused discontinuities when applied to the deformation vectors. This lead to an unreasonably warped dose distribution, shown in Figure 5.7B, with large ‘hot-spots’

greater than 20 Gy. The prescribed dose for this fraction is 2 Gy, therefore maximum doses greater than 2.5 Gy are not physically possible. The cause of these hot-spots was determined to be discontinuities in the scaled deformation vectors which lead to errors in the transport of incident particles through the deformed geometry.

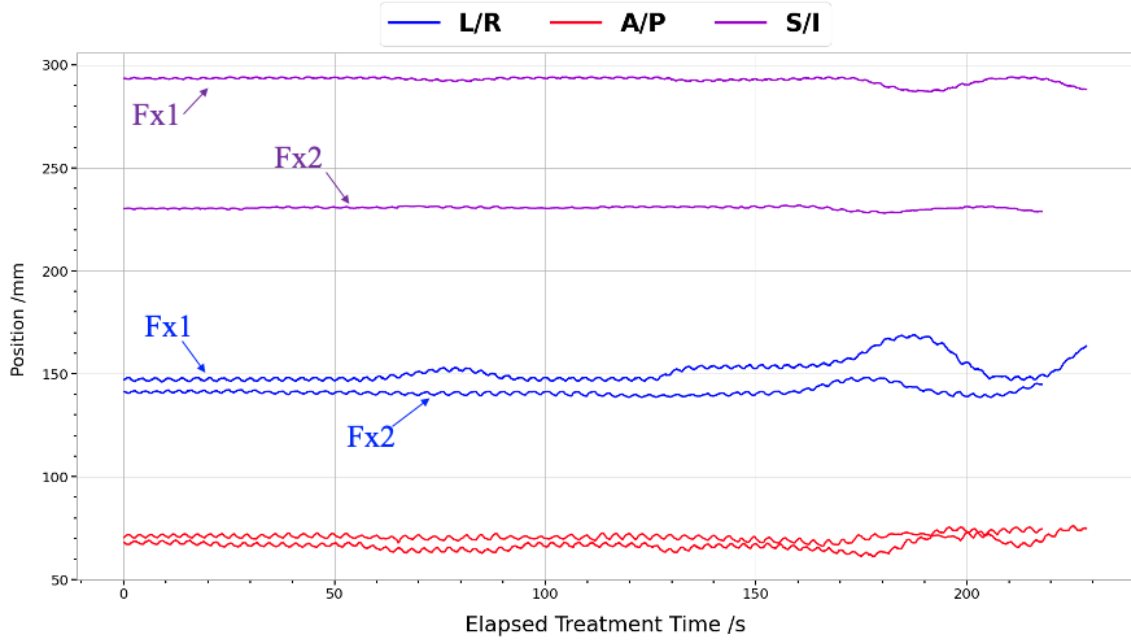
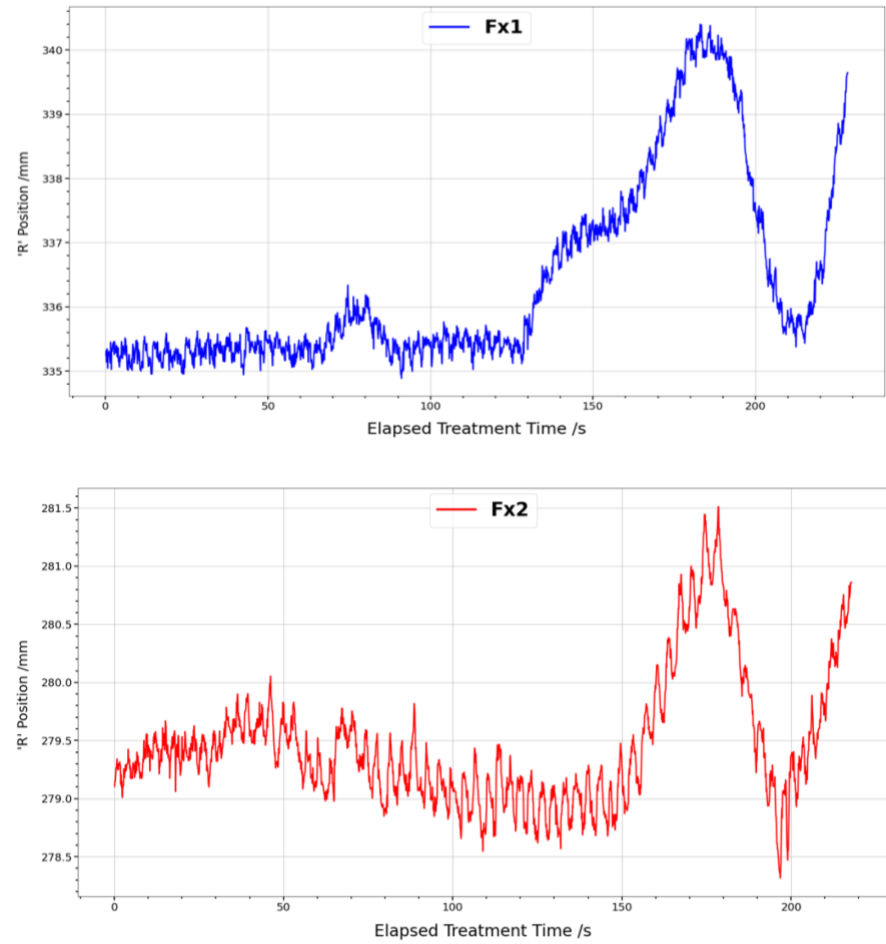


Figure 5.6: Motion components measured for all fractions for Patient 3, treated with abdominal compression. The fractions are labeled for the L/R and S/I position where notable position variations are observed.



A



B

Figure 5.7: A) Patient 3 ‘R’ position traces. B) Example of a 4D reconstructed dose distribution for Patient 3. The minimum threshold of the colorwash is set to 1 Gy, all doses above 20 Gy are shown in red. In such a treatment, the maximum dose would not typically exceed 2.5 Gy .

5.2 Motion trace normalization

The motion traces were normalized in two ways to investigate the sensitivity of the 4D simulations to the normalization scheme. In the first method (3D norm), the 3D motion traces were normalized to the average peak-peak displacement of the first treatment fraction. In the second normalization method (AP norm), applied only to Patient 2, the A/P motion traces were normalized to the A/P displacement measured between the inhale and exhale phases of the 4D-CT. The second normalization scheme was applied only to Patient 2 because the 4D-CT scan for Patient 1 did not span inferior enough to see the change in position of the abdomen at the location of the Bellows belt. Ideally, the normalization would relate back to the motion during 4D-CT, as this motion was used for the deformable registration.

An example of the 3D norm method applied to the second treatment fraction trace of Patient 1 is demonstrated in Figure 5.8. The set of normalized traces for all treatment fractions using the 3D norm method is shown in Figure 5.9 for Patient 1 and Figure 5.10a for Patient 2. The AP norm applied to the A/P traces for Patient 2 are shown together in Figure 5.10b.

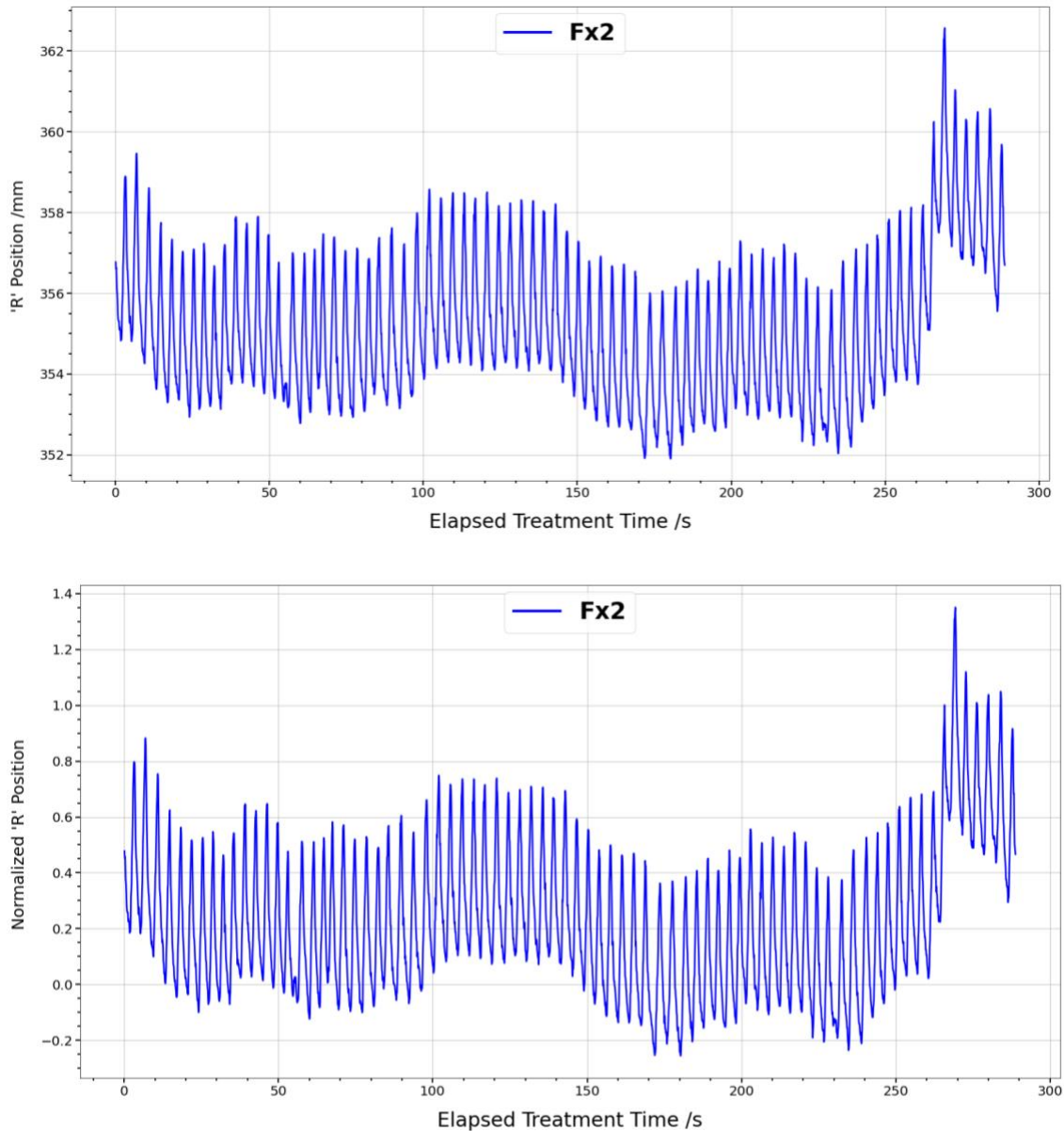


Figure 5.8: Example of the normalization of a single 3D motion trace, Fx 2. In the upper plot is the 3D position measured during treatment. The lower graph shows the same trace after baseline adjustment and normalization to the peak-peak displacement observed during the first treatment fraction

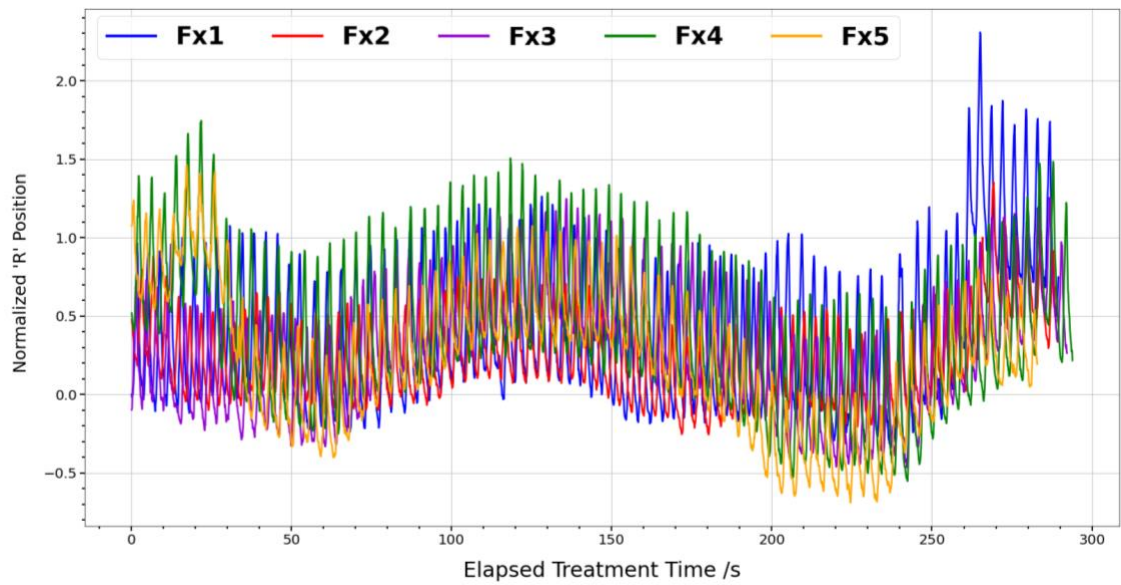


Figure 5.9 Normalized motion traces for all fractions for Patient 1 using the 3D norm. Traces were adjusted to their individual baseline and normalized to the peak-peak displacement observed during the first treatment fraction.

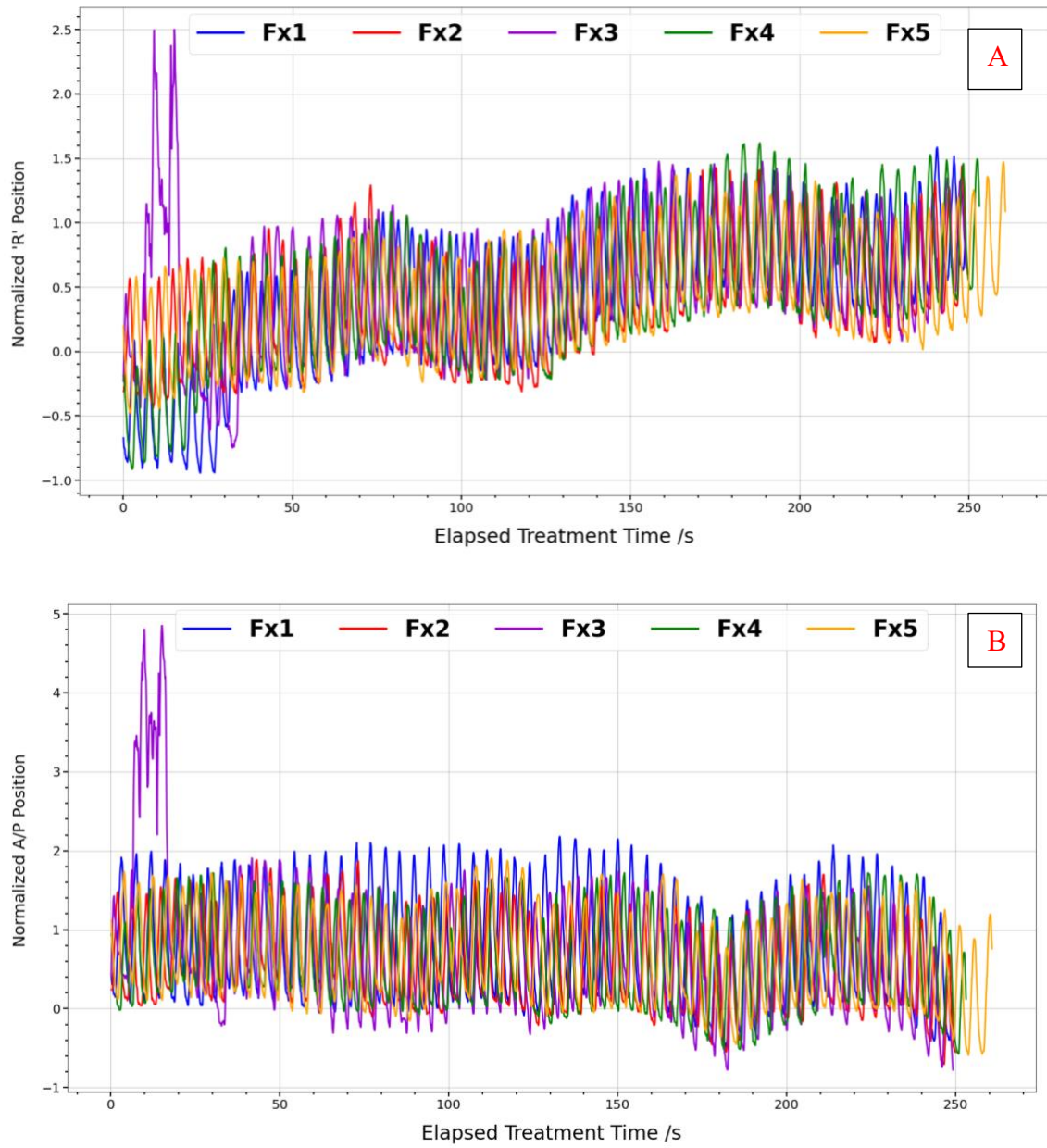


Figure 5.10: Demonstration of the different normalization schemes used for Patient 2. A) Using the 3D displacement, all motion traces were normalized to the peak-peak displacement measured during the first treatment fraction (3D norm). B) The A/P position traces were normalized to the motion amplitude measured from 4D-CT images (AP norm).

5.3 Comparison of DOSXYZnrc and Monaco TPS

5.3.1 Comparison of treatment plan dose calculations

Static dose calculations using the patient treatment plans were calculated in DOSXYZnrc on both the average and exhale CT. The DOSXYZnrc calculations on the average CT are compared to the plan calculated in the Monaco TPS. The DVHs showing the comparison of the plans calculated by Monaco and DOSXYZ are shown in Figure 5.12 and 5.14 for Patients 1 and 2, respectively. Monaco predicts a systematically lower dose to the patient compared to DOSXYZnrc. A comparison of the clinically relevant dose metrics is presented in Table 5.3. For Patient 1, the most significant differences between DOSXYZ and Monaco were in the V2 Gy (PTV) and the brachial plexus which had a percent difference of 8.3% and 12.6 % when comparing DOSXYZnrc and Monaco. For Patient 2, the largest differences were in the V2 Gy (PTV) and the D_{0.03cm³} for the heart, with percent differences of 7.25% and 6.11% respectively. A comparison of the isodose distributions between Monaco and DOSXYZnrc for the plans calculated on the AVG-CT for Patients 1 and 2 is shown in Figures 5.11 and 5.13. It can be seen that a greater portion of the GTV is covered by the 100% and 107% isodoses in the DOSXYZnrc calculated dose distribution.

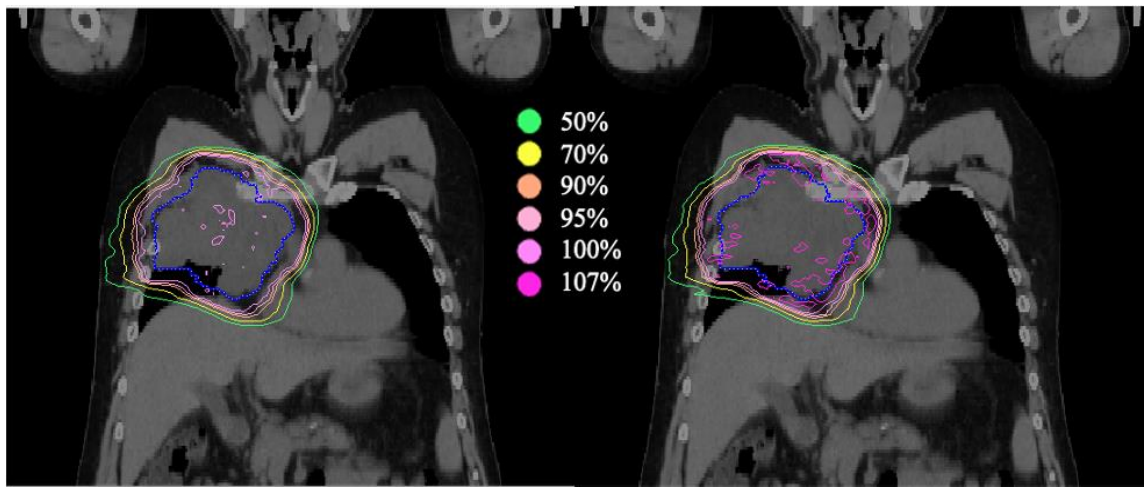


Figure 5.11: Isodose lines shown at isocenter for the prescription plan calculated on the AVG-CT, for Patient 1 calculated in Monaco (left) and DOSXYZnrc (right). Isodoses are given as a percentage of the prescription dose of 2 Gy. The GTV is shown outlined in blue.

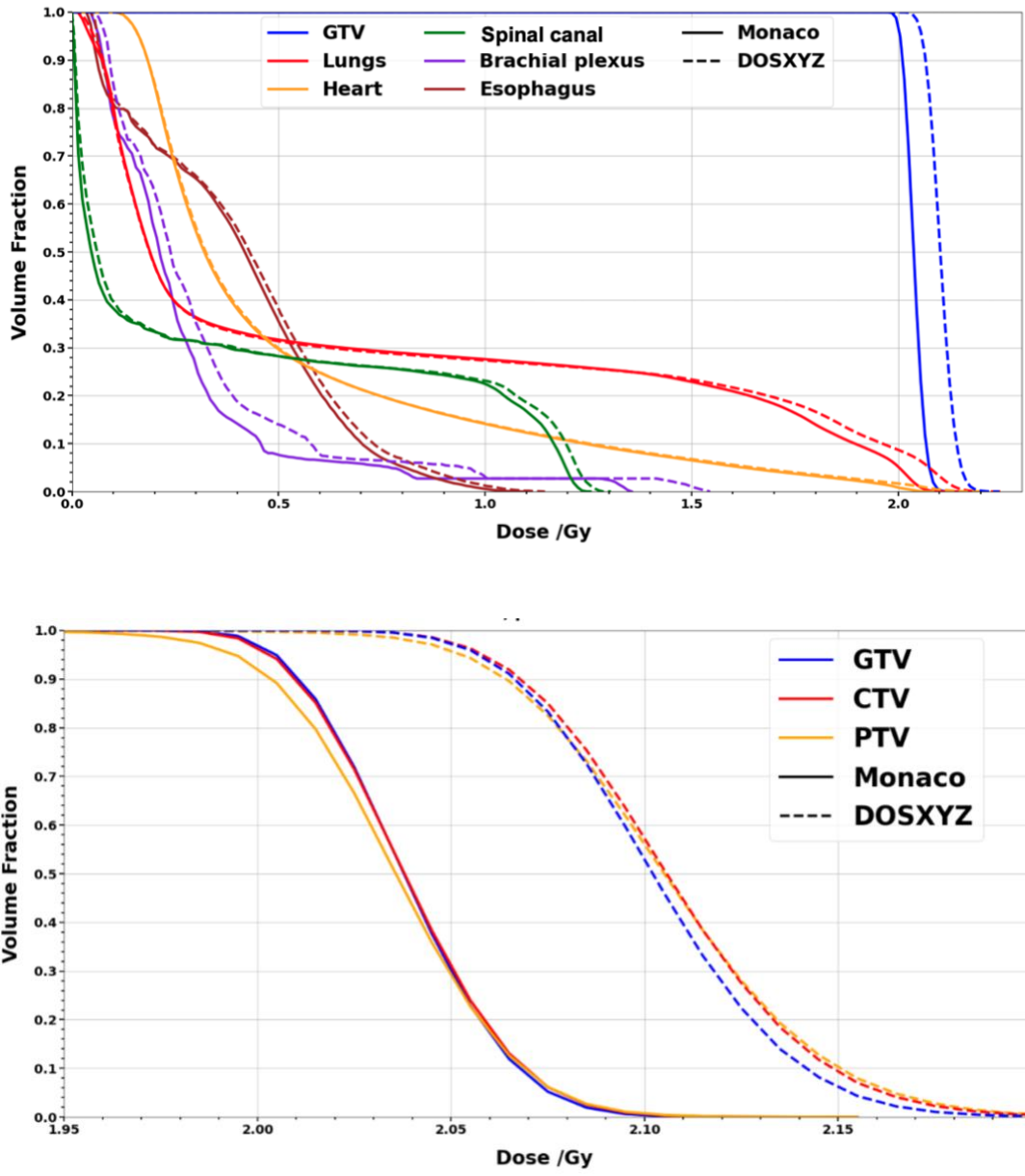


Figure 5.12: The upper plot shows a comparison of the DVH for the OAR, and GTV as calculated in Monaco (solid line) and DOSXYZnrc (dotted line) on the AVG-CT for Patient 1. The lower plot presents a detailed view of the differences in the DVHs for the tumour volumes between Monaco (solid line) and DOSXYZnrc (dashed line).

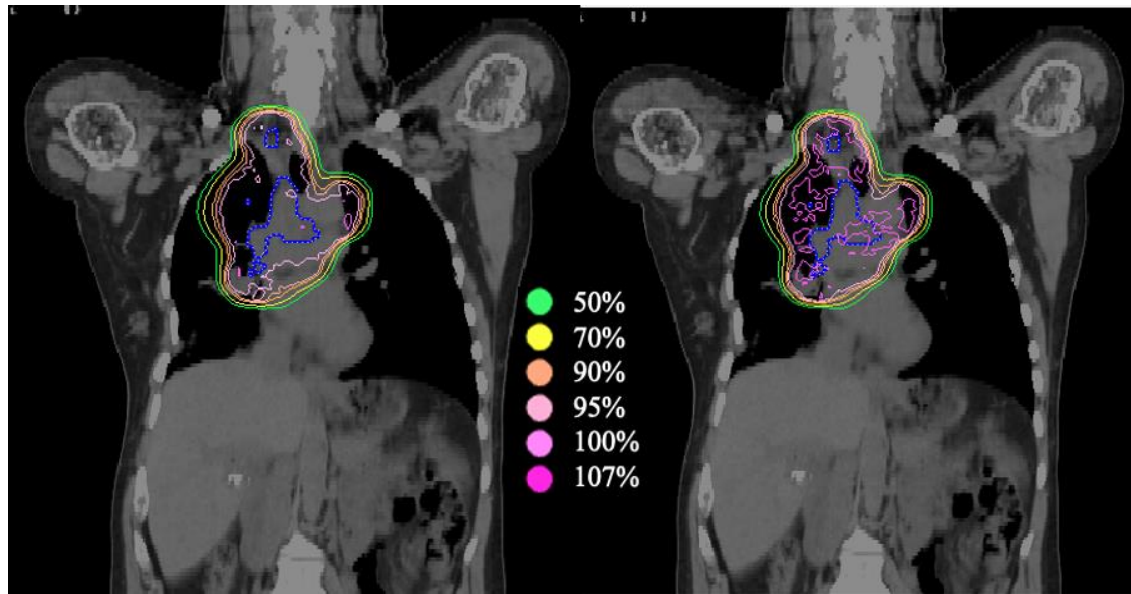


Figure 5.13: Isodose lines shown at isocenter for the prescription plan of Patient 2 calculated on the AVG-CT in Monaco (left) and DOSXYZnrc (right). Isodoses are given as a percentage of the prescription dose of 2 Gy. The GTV and GTVn are shown outlined in blue.

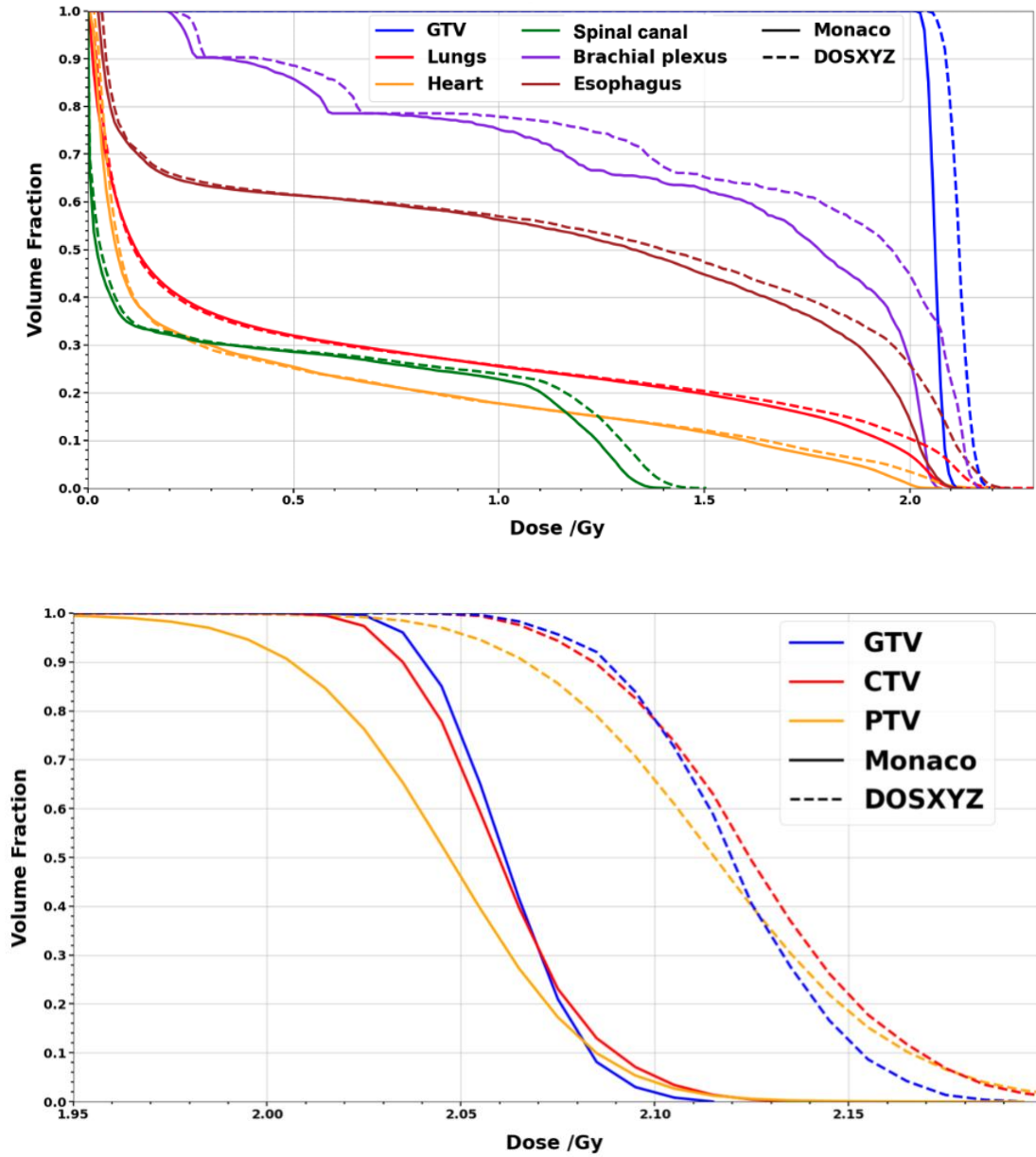


Figure 5.14: The upper plot shows a comparison of the DVH for the OAR, and GTV as calculated in Monaco (solid line) and DOSXYZnrc (dotted line) on the AVG-CT for Patient 2. The lower plot presents a detailed view of the differences in the DVHs for the tumour volumes between Monaco (solid line) and DOSXYZnrc (dashed line).

Table 5.3: Comparison of dose metrics calculated by the TPS and with DOSXYZnrc on the AVG-CT.
Volume dose metrics are scaled to the dose values per fraction, shown in brackets is the total treatment dose.

	Dose metric	Patient 1	Patient 2		
	Dose metric	Monaco	DOSXYZ (±1.0%)	Monaco	DOSXYZ (±1.0%)
PTV	D98% (Gy)	1.98	2.04	1.98	2.04
	D2% (Gy)	2.09	2.18	2.11	2.20
	V2/60 Gy* (%)	92	100	93	100
CTV	D98% (Gy)	2.00	2.05	2.02	2.07
	D2% (Gy)	2.09	2.18	2.11	2.19
	D50% (Gy)	2.04	2.11	2.06	2.12
	V2/60 Gy* (%)	96	100	100	100
GTV	D98% (Gy)	2.00	2.05	2.03	2.07
	D2% (Gy)	2.08	2.17	2.10	2.17
	D50% (Gy)	2.03	2.10	2.06	2.12
	V2/60 Gy* (%)	97	100	100	100
Brachial Plexus	D0.03 cm ³ (Gy)	1.34	1.52	2.06	2.16
Spinal Canal	D0.03 cm ³ (Gy)	1.24	1.28	1.39	1.47
Lungs	Dmean (Gy)	0.62	0.63	0.56	0.58
	V0.61/20 Gy* (%)	30	30	30	30
	V0.15/5 Gy* (%)	61	61	46	45
Heart	V0.91/30 Gy* (%)	16	16	19	19
	V1.36/45 Gy *(%)	8	8	14	14
	D0.03 cm ³ (Gy)	2.07	2.18	2.06	2.19
Esophagus	Dmean (Gy)	0.40	0.42	1.07	1.13
	V1.51/50 Gy* (%)	0	0	45	47
	V1.06/35 Gy* (%)	0	0	55	56

*Dose scaled to dose per fraction/Total dose

5.3.2 Verification of Beam model

Due to the differences in the doses calculated in DOSXYZnrc and Monaco, the accuracy of the BEAMnrc model of the Elekta Infinity linac was checked against measurements to ensure it was properly modelling the treatments fields. To determine the appropriate field size to check against measurements, the dominant field size in each patient's treatment was calculated by reading each leaf pair opening in the treatment plans and calculating the width of the pair opening at isocenter.

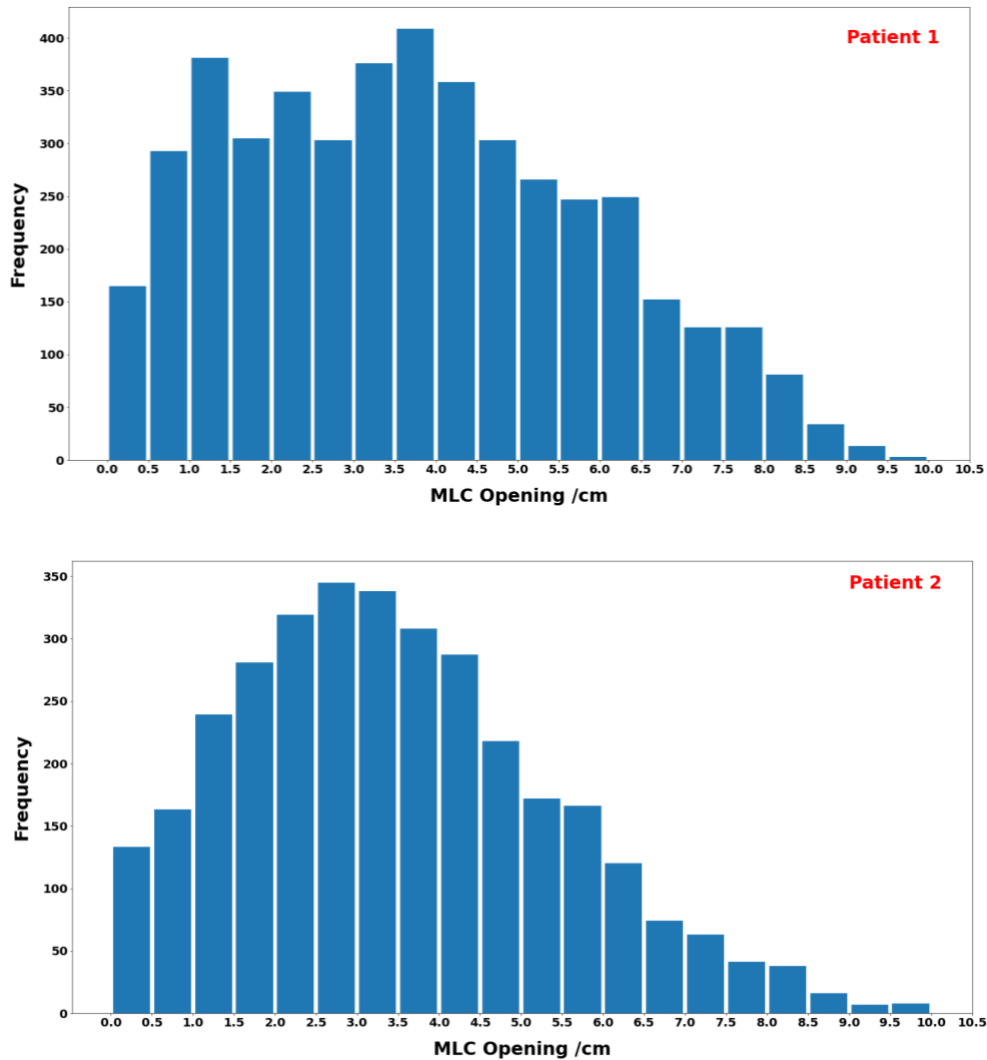


Figure 5.15: MLC opening width frequency in clinical patient plans. The openings are calculated at the treatment isocenter.

As can be seen in Figure 5.15, most MLC openings in the patient plans are below 5 cm. Therefore, a DOSXYZnrc simulation of a 2x2 cm² field, the smallest field size used for linac commissioning measurements, was compared to measurements taken at an SSD of 100 cm in a 60x60x60 cm³ water phantom. The field was delivered with a 0-degree collimator angle and the profiles were normalized to their own maximum according to the clinical protocol. A comparison was also made to Monaco, where a 2x2 cm² field was simulated on a cube of water of the same size as the water phantom. The profiles in the cross-line (corresponds to patient L/R, direction of MLC travel) and in-line (corresponds to patient S/I, direction of jaw travel) directions are shown in Figures 5.16 and 5.17. The DOSYXZ and the Monaco profiles both passed the 2%/2mm 1D gamma index¹⁵¹ when compared to measurements. However, in general, the Monaco simulations were showing an underdosing in the penumbra region when compared to both measurements and DOSXYZnrc. Also of note is the difference in field size in the central region of the in-line profiles. The Monaco profiles are narrower than both the DOSXYZnrc and measured profiles.

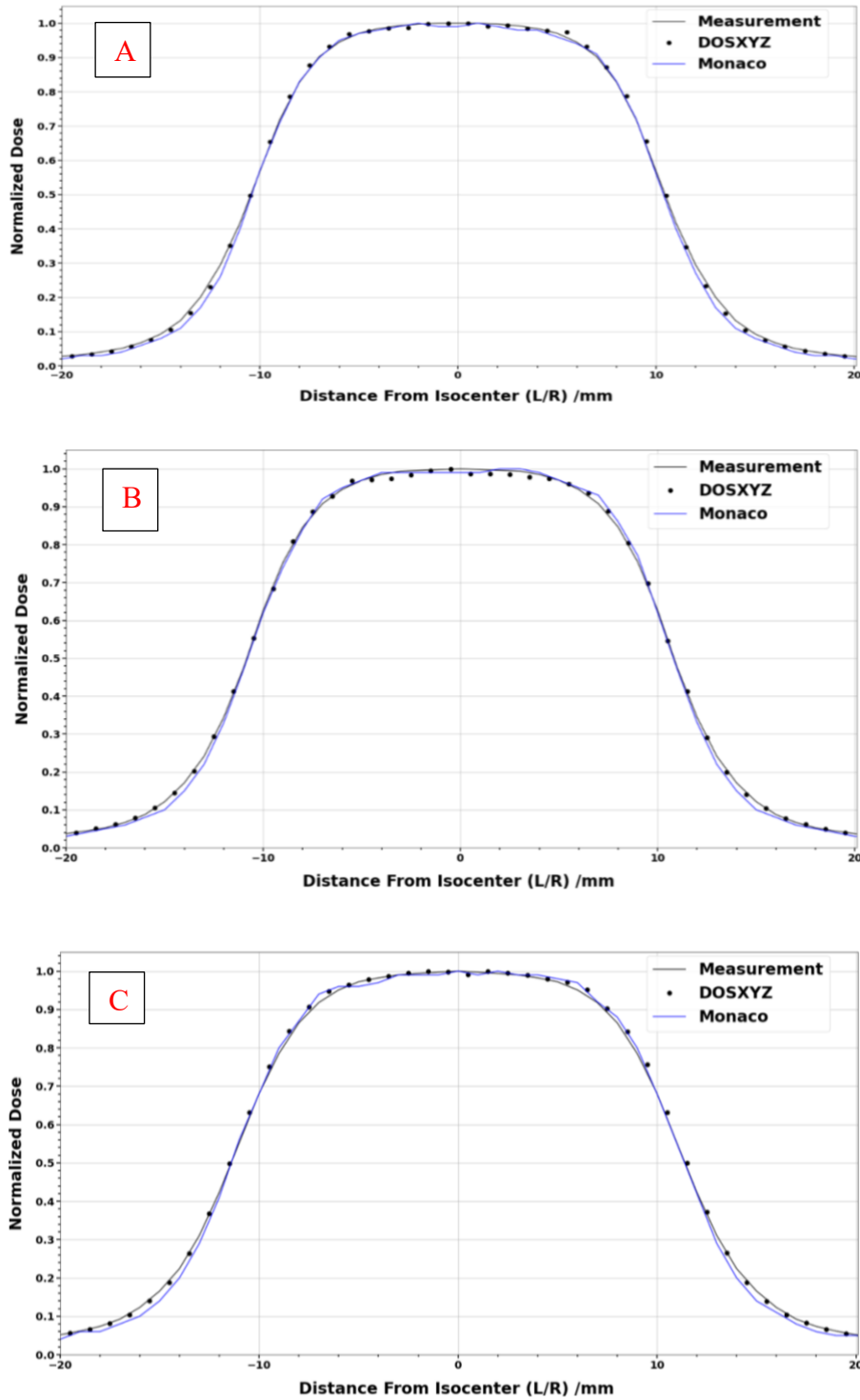


Figure 5.16: Comparison of profiles from measurements, DOSXYZnrc and Monaco in the cross-line direction (patient L/R) at depths of 1.6 cm (A), 5 cm (B) and 10 cm (C). The DOSXYZnrc and TPS simulations were completed with a 0.5% uncertainty.

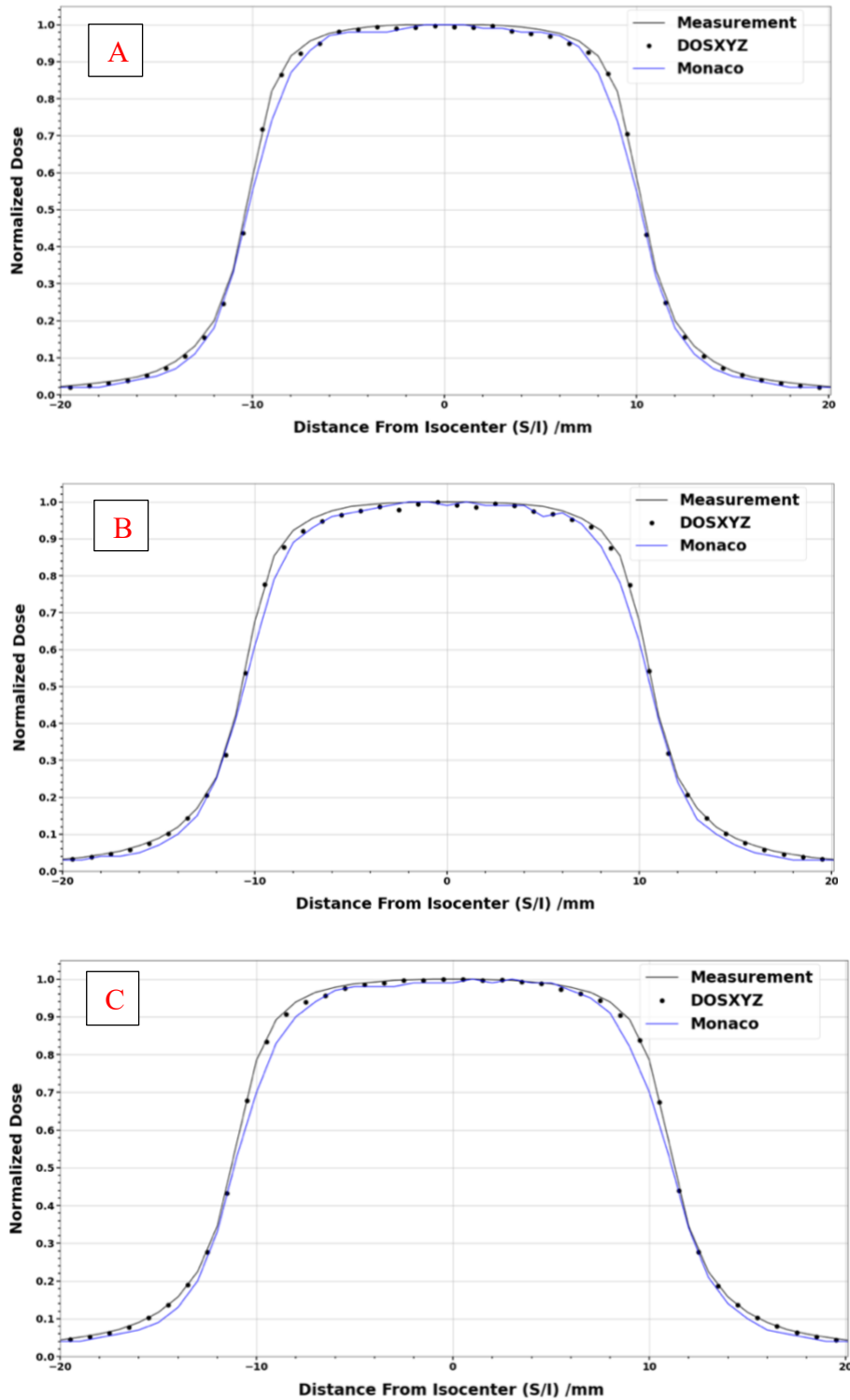


Figure 5.17: Comparison of profiles from measurements, DOSXYZnrc and Monaco in the in-line direction (patient S/I) at depths of 1.6 cm (A), 5 cm (B) and 10 cm (C). The DOSXYZnrc and TPS simulations were completed with a 0.5% uncertainty.

Given that small MLC openings dominate the field sizes in the patient plans, difference in the DVH and dose metrics when comparing both Monaco and DOSXYZnrc could be explained by the differences observed in these $2 \times 2 \text{ cm}^2$ dose profiles.

5.4 4D dose reconstructions

5.4.1 Patient 1

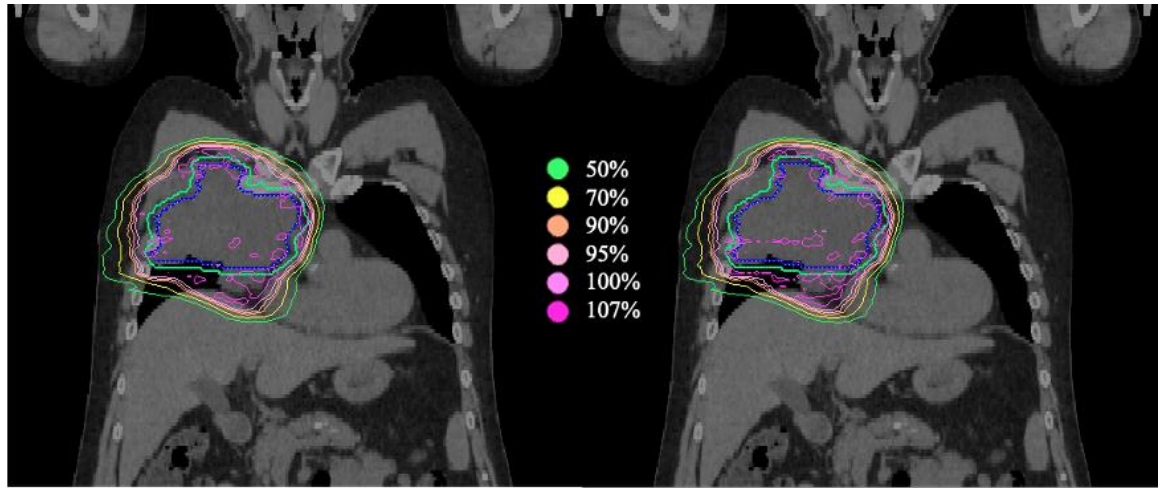


Figure 5.18: Isodose distributions calculated with the 4D reconstruction (accumulated on the exhale-CT) for Fx1 (right) compared to the DOSXYZnrc simulation on the exhale-CT (left), for Patient 1.

An example of the dose distribution from the 4D dose reconstruction compared to the DOSXYZnrc simulation is shown in Figure 5.18. The results of the 4D reconstructions for Patient 1, compared to Monaco and DOSXYZnrc calculations on exhale, are shown in the forms of DVH in Figure 5.19 and as dose metrics in Table 4. The 4D reconstructions are calculated on the exhale phase as the reference, and for this reason the exhale contours were used to evaluate the dose metrics. To mitigate differences in the dose metrics arising from inconsistencies in the contours between the AVG-CT and exhale-CT, the 4D reconstructed doses are compared to the clinical plan evaluated on the AVG-

CT and exhale-CT in both Monaco and DOSXYZnrc. The differences between Monaco and the reconstructed doses, can mostly be attributed to differences in calculation algorithms, as no significant differences were observed between the plans calculated on the exhale phase in DOSXYZnrc and the 4D reconstructions.

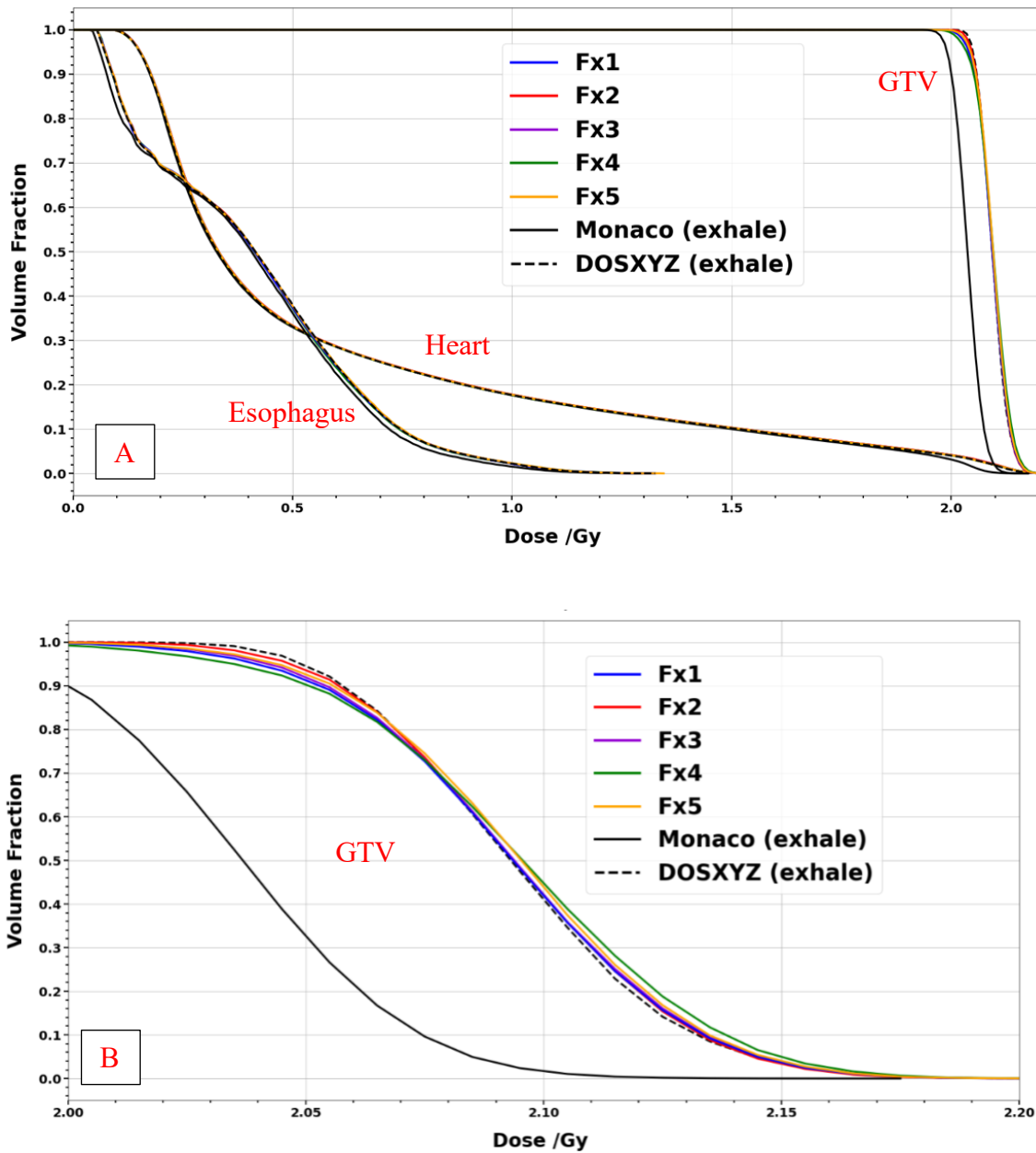


Figure 5.19: In A, DVHs for GTV, esophagus and heart are shown for Patient 1. The Monaco and DOSXYZnrc calculations of the plan on the exhale phase are compared to the 4D reconstructions for each fraction (3D norm). The 4D reconstructions are labeled by their fraction number (ex. Fx 1). In B, a detailed view of the DVH for the GTV is shown.

Table 5.4: Comparison of dose metrics for the GTV, heart and esophagus. The Monaco and DOSXYZnrc calculations of the plan are compared to the 4D reconstructions, with uncertainties between 0.9% and 1.0%, for Patient 1, using the 3D norm.

Structure	Dose metric	Monaco	DOSXYZ	Monaco	DOSXYZ	4DdefDOSXYZ				
		(Exhale-CT)	(Exhale-CT) (±1.0%)	(AVG-CT)	(AVG-CT) (±1.0%)	Fx 1	Fx 2	Fx 3	Fx 4	Fx 5
GTV	D98% (Gy)	1.98	2.04	2.00	2.05	2.02	2.04	2.03	2.02	2.03
	D2% (Gy)	2.10	2.16	2.08	2.17	2.16	2.16	2.16	2.16	2.16
	D50% (Gy)	2.04	2.09	2.03	2.10	2.10	2.10	2.10	2.10	2.09
	V2/60 Gy* (%)	90	100	97	100	100	100	100	100	100
Heart	V0.91/30 Gy* (%)	20	20	16	16	20	20	20	20	20
	V1.36/45 Gy* (%)	12	12	8	8	12	12	12	12	12
	D0.03 cm ³ (Gy)	2.15	2.22	2.07	2.18	2.24	2.23	2.22	2.22	2.22
Esophagus	Dmean (Gy)	0.40	0.42	0.40	0.42	0.42	0.42	0.42	0.42	0.42
	V1.51/50 Gy* (%)	0	0	0	0	0	0	0	0	0
	V1.06/35 Gy (%)	0	0	0	0	0	0	0	0	0

*Dose scaled to dose per fraction/Total dose

5.4.2 Patient 2

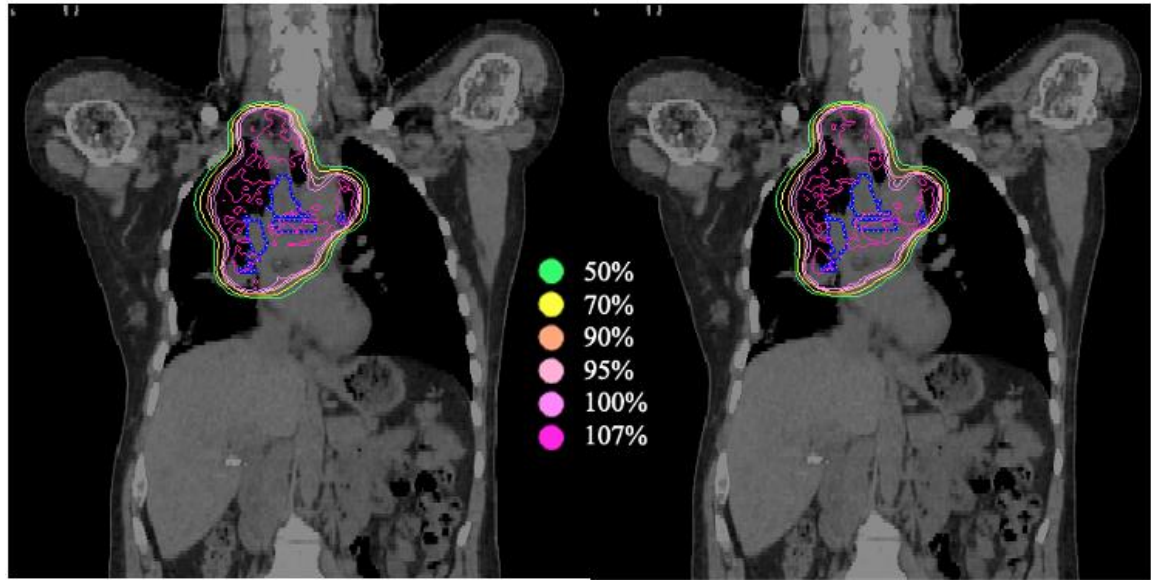


Figure 5.20: Isodose distributions for Patient 2, calculated with the 4D reconstruction for Fx1 (right) using the 3D norm compared to the DOSXYZnrc simulation on the exhale- CT (left).

The results for Patient 2 are shown as DVHs in Figure 5.21 and as dose metrics in Tables 5.5 and 5.6. An example of the isodose distribution obtained from the 4D reconstruction compared to that calculated in DOSXYZnrc is shown in Figure 5.20. While there are differences between the TPS and the reconstructed doses this can be attributed to differences in calculation algorithms as no significant differences were observed between the plan calculated on the exhale phase in DOSXYZnrc and the 4D reconstructions. There is no significant difference in the 4D reconstructions as compared to the plan calculated in DOSXYZnrc. This is also the case for the reconstructions calculated using both the 3D and A/P norm. A direct comparison in dose metrics for each fraction are

shown in Table 5.7. No significant differences for each fraction were noted between normalization schemes.

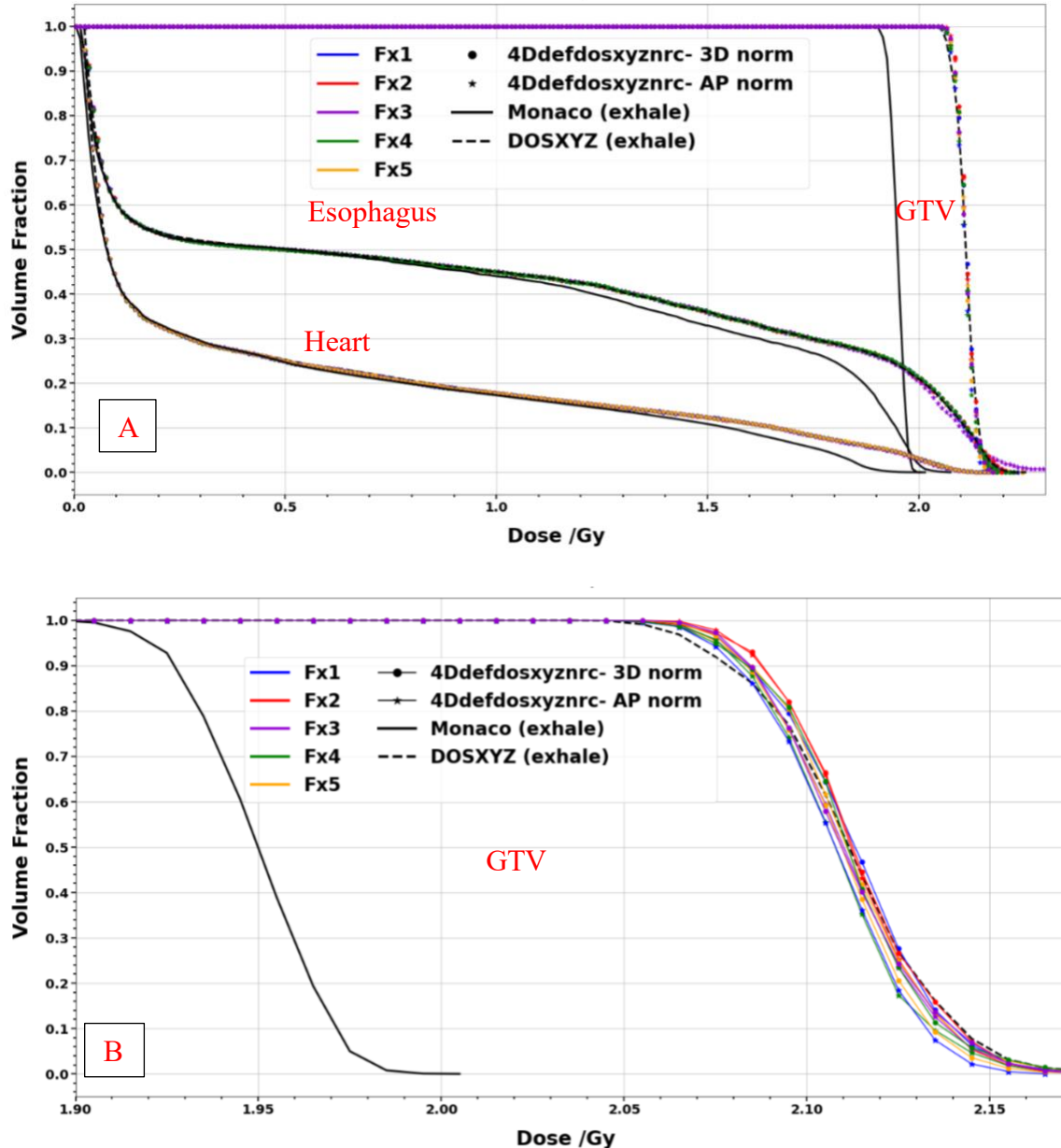


Figure 5.21: In A, DVHs for GTV, esophagus and heart are shown for Patient 2. The Monaco and DOSXYZnrc calculations of the plan on the exhale phase are compared to the 4D reconstructions for each fraction. Reconstructions using the 3D norm are shown with the round marker and A/P norm are shown with the star. The 4D reconstructions are labeled by their fraction number (ex. Fx1). In B, a detailed view of the DVH for the GTV is shown.

Table 5.5: Patient 2, 4D reconstructions using 3D norm. Average statistical uncertainty was 0.7% for the 4D reconstructions.

Structure	Dose metric	Monaco (Exhale -CT)	DOSXYZ (Exhale- CT) ($\pm 1.0\%$)	Monaco (AVG- CT)	DOSXYZ (AVG-CT) ($\pm 1.0\%$)	4DdefDOSXYZ				
						Fx 1	Fx 2	Fx 3	Fx 4	Fx 5
GTV	D98% (Gy)	1.91	2.06	2.03	2.07	2.07	2.07	2.07	2.07	2.07
	D2% (Gy)	1.98	2.16	2.10	2.17	2.16	2.16	2.16	2.16	2.15
	D50% (Gy)	1.95	2.11	2.06	2.12	2.11	2.11	2.11	2.11	2.11
	V2/60 Gy* (%)	0.3	100	100	100	100	100	100	100	100
Heart	V0.91/30 Gy* (%)	0.18	0.19	19	19	0.19	0.19	0.19	0.19	0.19
	V1.36/45 Gy* (%)	0.13	0.14	14	14	0.14	0.14	0.14	0.14	0.14
	D0.03 cm ³ (Gy)	2.0	2.17	2.06	2.19	2.16	2.16	2.16	2.16	2.17
Esophagus	Dmean (Gy)	0.98	0.91	1.07	1.13	0.91	0.91	0.91	0.91	0.91
	V1.51/50 Gy* (%)	33	36	45	47	36	36	36	36	36
	V1.06/35 Gy* (%)	43	44	55	56	44	44	44	44	44

*Dose scaled to dose per fraction/Total dose

Table 5.6: Patient 2, 4D reconstructions using AP norm. The average statistical uncertainty was 0.7% for the 4D reconstructions.

Structure	Dose metric	Monaco (Exhale -CT)	DOSXYZ (Exhale- CT) ($\pm 1.0\%$)	Monaco (AVG- CT)	DOSXYZ (AVG-CT) ($\pm 1.0\%$)	4DdefDOSXYZ				
						Fx 1	Fx 2	Fx 3	Fx 4	Fx 5
GTV	D98% (Gy)	1.91	2.06	2.03	2.07	2.07	2.07	2.07	2.07	2.07
	D2% (Gy)	1.98	2.16	2.10	2.17	2.15	2.15	2.16	2.15	2.16
	D50% (Gy)	1.95	2.11	2.06	2.12	2.10	2.11	2.11	2.11	2.11
	V2/60 Gy* (%)	0.3	100	100	100	100	100	100	100	100
Heart	V0.91/30 Gy* (%)	0.18	0.19	19	19	0.19	0.19	0.19	0.19	0.19
	V1.36/45 Gy* (%)	0.13	0.14	14	14	0.14	0.14	0.14	0.14	0.14
	D0.03 cm ³ (Gy)	2.0	2.17	2.06	2.19	2.17	2.16	2.16	2.16	2.16
Esophagus	Dmean (Gy)	0.98	0.91	1.07	1.13	0.91	0.91	0.91	0.91	0.91
	V1.51/50 Gy* (%)	33	36	45	47	36	36	36	36	36
	V1.06/35 Gy* (%)	43	44	55	56	44	44	44	44	44

*Dose scaled to dose per fraction/Total dose

Chapter 6: Discussion and Conclusions

6.1 Discussion

The framework developed in this work for 4D reconstructions was covered in detail in Chapter 4. Deformation vectors representing the change in anatomy between inhale and exhale were used in the 4D reconstruction to deform the patient anatomy at each point during treatment. The magnitude of these deformations was based on scaling factors derived from surface motion measurements acquired during patient treatments. The surface motion measurements, used as a surrogate for tumour motion, were collected with the electromagnetic position sensor of the RADPOS system. The reconstructions also used treatment log files to synchronize the patient motion to the real-time treatment delivery. In this way, both the dose blurring effect and interplay effect caused by respiratory motion during treatment could be modeled. For both patients, the 3D motion traces were used in the reconstructions and normalized to the average peak-peak amplitude measured during the first treatment fraction. For Patient 2, a second normalization scheme was tested which used the A/P motion normalized to the inhale-exhale motion amplitude measured from 4D-CT planning images. Normalizing to the peak-peak displacement exhibited during 4D-CT using the motion trace from Bellows belt would have been ideal. However, a calibration coefficient to convert the Bellows trace data to centimeters was not available at that time.

In Chapter 5, the results of the dose reconstructions were presented. Prior to the calculation of the 4D reconstructions, the static dose simulations of the treatment plans were calculated in DOSXYZnrc and compared to the TPS. There were disagreements in

the relevant clinical dose metrics between DOSXYZnrc and Monaco of up to 8.3% in the V2 Gy (PTV). To verify the BEAMnrc model used in these calculations, beam profiles calculated in DOSXYZnrc for a 2x2 cm² field were compared to commissioning measurements. These profiles agreed with measurements within the 2%/2mm Gamma index criteria. Furthermore, the Monaco calculations of the same field yielded narrower profiles and less dose in the penumbra region as compared to DOSXYZnrc and measurements. These differences could contribute to the differences in calculated planed dose between the two systems. When examining the results of the 4D reconstructions for the GTV, heart and esophagus, the measured motion did not result in significantly different calculated dose metrics between fractions. Additionally, no significant differences were found between the doses calculated with the two normalization schemes. When compared to the DOSXYZnrc calculated plan dose, there were no significant changes when motion was considered. The third patient recruited for this study was treated with abdominal compression which reduced their respiratory motion amplitude. The small magnitude of motion and sizeable position changes measured for this patient lead to discontinuities in the deformation vectors and resulted in an unrealistically warped dose distribution. Therefore, the reconstructions were not completed for this patient.

Both patients whose measurements were completely analyzed had upper or upper-mid lobe tumors. These tumours have been shown to move less than free, lower lobe, tumours. For this reason, it is not unexpected that there be very little difference between the planned and reconstructed doses. While the motion scaling factor assigned at any given moment in the reconstruction may indicate that the tumour is in full exhale or

inhale, the amount of displacement that this corresponds to depends on the deformation vectors which represent the actual tumour motion between the inhale and exhale.

Therefore, if the tumour experienced very little movement between the inhale and exhale phase, the reconstructed doses are not expected to vary significantly from the static calculation. Patient 3's tumour was a lower lobe tumour which experienced more motion during respiration. However, clinical protocol dictates that in this case, patients should be compressed during treatment to minimize the amplitude of their respiratory motion. If patients present for treatment with significant tumour motion that may compromise the dose to the tumour, they would likely be compressed during treatment.

There were some challenges to this study, including the small patient cohort, the unexplained shifts in the position measurements and the complications with the reconstructions when compression was used.

The complications that arose when reconstructing the dose delivered to Patient 3 represent a limitation of the reconstruction method that would need to be resolved for future use. The motion modeling would need to be refined so that large scaling factors which would unrealistically warp the calculated dose distribution could be avoided. It should be noted, however, that for patients with such small motion, on the order of the resolution of the calculations (and measurements), it may not be appropriate or necessary to perform a 4D dose reconstruction using this framework.

There were also several instances of 'hot-spots' in the dose distributions obtained with 4Ddefdosxyznrc. These were areas, usually a few voxels in size, of unrealistically high

dose. The dose was orders of magnitude larger than the maximum dose in the treatment plan and do not represent the actual dose delivered. These occurred for Patient 3 and also for Patient 2, in fraction 3 where a large position irregularity was observed at the beginning of the treatment. These hotspots are caused by discontinuities in the deformation vectors. The raw deformation vectors were tested for discontinuities, and none were found. However, when the deformation vectors are scaled with large scaling factors such as what occurred with Patient 3 discontinuities were detected. These discontinuities lead to errors in the particle tracking in 4Ddefdosxyznrc, when this happens the particle's energy is deposited at its location leading to these 'hot-spots' of high dose.

Several limitations of this study should be noted, firstly, the basis of the reconstruction was the use of surface motion measurements to uniformly scale the deformation vectors. This implies a perfect correlation between the internal motion and the external abdominal motion during respiration. This may not always be the case,^{27,34} and the correlation may be subject to change throughout the course of the patient's treatment.²⁹ Using surface motion as a surrogate is an inherent limitation of this method but other respiratory tracking methods are more invasive and may not be clinically feasible. A more accurate internal-external correlation model could be established by correlating surface motion measurements taken during 4D-CT to the deformation vector maps obtained from deformable registration of the 4D-CT images. Studies have been conducted in which principle component analysis (PCA) was performed to correlate the internal and external motion.^{152–154} Using PCA these models were able to correlate internal respiratory motion

to an external respiratory signal^{153,154} and to the diaphragm position imaged with respiratory correlated CT.¹⁵² In this work, such an analysis was not possible as there was no RADPOS data taken at the time of 4D-CT. Additionally, a PCA analysis of the tumour may have been difficult given the small amount of tumour motion (less than 5 mm).

Another limitation is that the deformation vectors, as well as the patient phantom, used in the 4D reconstructions were obtained from the 4D-CT, which is acquired during the treatment planning phase. Between treatment planning and delivery of a treatment fraction, it is possible for weeks to have passed. In that time, the tumour's size and shape may have changed. The manner in which the patient breathes may also have changed in that time. Because of this, both the reference geometry and the deformation vectors obtained from 4D-CT may no longer accurately represent the patient's anatomy and internal respiratory motion. One possible way to correct for this would be to acquire respiratory correlated cone-beam CT (4D CBCT) images using the imaging system onboarded to the linac, prior to each treatment fraction.¹⁵⁵ Using these images, a new patient motion model could be obtained for use in the reconstruction of that day's treatment. However, more image projections are required for these 4D CBCT images which increases the imaging time¹⁵⁶ as well as the dose¹⁵⁷ compared to a 3D CBCT. In a Monte Carlo study of the effective dose received by patients it was shown that the effective dose from 4D CBCT was twice that of 3D CBCT.¹⁵⁷ Therefore, acquisition of a 4D CBCT for each treatment fraction may not be clinically feasible.

6.2 Future work

In future work, a more detailed motion analysis could be completed. Firstly, the removal of the baseline drifts could be investigated, this. This could be done by the calculation of a moving average or the use of a high-pass filter to remove the low-frequency component of the signal. Secondly, methods to reduce instances of discontinuities and dose ‘hot-spots’ could be further researched. The use of an alternative deformable image registration algorithm could provide smoother deformations which may remain continuous even with large scaling factors. It is also possible that the large irregularities in the patient’s surface motion that caused these large scaling factors do not correspond to changes in the tumour position. A refinement of the motion modeling could be implemented to account for this by establishing a correlation model between each patient’s tumour and surface motion. In this way, the large position shifts might not lead to such a large scaling of the tumour motion.

Ideally, the motion measured during treatment would be normalized to the patient’s respiratory motion amplitude during 4D-CT. To do this, a calibration coefficient relating the motion measured by the Bellows belt (in arbitrary units) to mm would be required. Alternatively, the patient surface motion could be measured with RADPOS during 4D-CT.

A procedure should also be implemented to improve the reproducibility of the RADPOS sensor position between treatments. Large position variations were observed between fractions. While these were corrected in the normalization process, the measurement

process could be modified to reduce these changes. To start, a secondary position sensor should be used to reduce uncertainties in the setup of the transmitter relative to the primary position sensor on the patient's surface. The secondary sensor could be placed on the treatment couch and the position of the primary sensor could be taken relative to the secondary. This would account for changes in the transmitter position. Next, rather than averaging the minimum positions in the motion traces, prior to each treatment the position of the exhale should be established. If tolerable, with the RADPOS in place, the patient could be asked to exhale and hold their breath for a few seconds, the time of this could be recorded to be found later in the motion recording. The position during this time could then be used to offset the motion traces to the exhale position prior to normalization. Ideally, the shifts in position would have been investigated further and the position measurements would have been refined. Unfortunately, due to the COVID-19 pandemic, the study had to be halted and no further patient measurements could be taken.

It would also be of benefit to extend this study to include a larger number of patients with a variety of respiratory patterns and tumour locations. Additionally, the inclusion of SBRT patients with longer treatments would be important as their respiratory motion may display more variation over longer periods of times.

6.3 Conclusion

A framework was developed for the 4D reconstruction of patient doses with 4Ddefdosxyznrc using surface motion measurements and treatment delivery log files. To demonstrate the use of this framework, 3 patients receiving VMAT lung cancer

treatments were recruited and motion measurements were collected during their treatments for a total of 12 fractions. The average 3D motion amplitude measured during treatments for these patients were 5.5 ± 1.4 mm, 5.4 ± 0.4 mm, and 0.40 ± 0.03 mm, respectively. The reconstructions were completed for the two patients, the third was excluded due to complications in the reconstructions caused by the used of abdominal compression. The reconstructed doses did not show significant inter-fractional changes despite inter-fractional changes in surface respiratory motion amplitude. Target coverage as measured by the D98% to the target volume increased by a maximum of 2% in the reconstructed doses. These results are consistent with the small amount of tumour motion that would be expected of attached upper-lobe tumours. This is also demonstrative of the efficacy of the margins added to the GTV when planning to encompass tumour motion to ensure that adequate dose coverage is achieved even when the tumour moves due to respiration. It was most natural to apply this method to cases of lung cancer where tumour motion due to respiration is a prominent concern. In future work, this framework could be equally applied to other areas such as the liver where movement during respiration has also been noted.

Appendix



The Ottawa Hospital | L'Hôpital d'Ottawa



The Ottawa Hospital | L'Hôpital d'Ottawa

RESEARCH
INSTITUTE



Minimal Risk Informed Consent Form for Participation in a Research Study

Study Title: *Use of RADPOS system for 4D Monte Carlo dose calculations for lung patients*

OHSN-REB Number: 20190030-01H

Study Doctor: *Dr. Robert MacRae, Division of Radiation Oncology, tel. 613-737-7700 ex. 70205*

INTRODUCTION

You are being invited to participate in a research study. You are invited to participate in this study because you are receiving radiotherapy for lung cancer. This consent form provides you with information to help you make an informed choice. Please read this document carefully and ask any questions you may have. All your questions should be answered to your satisfaction before you decide whether to participate in this research study.

Please take your time in making your decision. You may find it helpful to discuss it with your friends and family. Taking part in this study is voluntary. You have the option to not participate at all or you may choose to leave the study at any time. Whatever you choose, it will not affect the usual medical care that you receive outside the study.

IS THERE A CONFLICT OF INTEREST?

There are no conflicts of interest to declare related to this study.

WHY IS THIS STUDY BEING DONE?

The purpose of this study is to evaluate a new method to analyze radiation therapy treatments for lung patients, which takes into account the patient breathing pattern during the treatment.

HOW MANY PEOPLE WILL TAKE PART IN THIS STUDY?

It is anticipated that about 10 people will take part in this study, from the cohort of lung cancer patients receiving radiation therapy at the Ottawa Hospital Cancer Centre.

This study should take 2 years to complete and the results should be known in about 3 years.

WHAT WILL HAPPEN DURING THIS STUDY?

Each study participant will receive their 4D CT scan and radiation therapy treatment, as any other lung cancer patient would.

In addition, in this study we will position the RADPOS probe on your skin. RADPOS, Radiation-Position measuring system, allows for simultaneous measurement of spatial position and verification of radiation dose. RADPOS probe will collect the information about the chest wall or abdomen movement related to your breathing. We will do it for the CT simulation and for each treatment fraction to see if your breathing pattern changes during the entire course of radiation therapy.

The study staff will then examine the results to determine how closely the RADPOS results compare to the 4D CT results and if the patient breathing pattern changes during the course of treatment and how significantly this affects the delivered treatment.

HOW LONG WILL PARTICIPANTS BE IN THE STUDY?

Your participation on this study will last for the duration of your radiotherapy treatment.

CAN PARTICIPANTS CHOOSE TO LEAVE THE STUDY?

You can choose to end your participation in this research (called withdrawal) at any time without having to provide a reason. If you choose to withdraw from the study, you are encouraged to contact the research team.

You may withdraw your permission to use information that was collected about you for this study at any time by letting the research team know. However, this would also mean that you withdraw from the study.

WHAT ARE THE RISKS OR HARMS OF PARTICIPATING IN THIS STUDY?

There are no anticipated risks or harms related to this study.

WHAT ARE THE BENEFITS OF PARTICIPATING IN THIS STUDY?

There are no benefits to you for taking part in this study.

HOW WILL PARTICIPANT INFORMATION BE KEPT CONFIDENTIAL?

If you decide to participate in this study, the research team will only collect the information they need for this study.

Records identifying you at this centre will be kept confidential and, to the extent permitted by the applicable laws, will not be disclosed or made publicly available, except as described in this consent document.

Authorized representatives of the following organizations may look at your original (identifiable) medical records at the site where these records are held, to check that the information collected for the study is correct and follows proper laws and guidelines.

- The Ottawa Health Science Network Research Ethics Board who oversees the ethical conduct of this study.
 - Ottawa Hospital Research Institute to oversee the conduct of research at this location.
- If the results of this study are published, your identity will remain confidential. It is expected that the information collected during this study will be used in analyses and will be published/presented to the

scientific community at meetings and in journals.

Your de-identified data from this study may be used for other research purposes. If your study data is shared with other researchers, information that links your study data directly to you will not be shared.

Even though the likelihood that someone may identify you from the study data is very small, it can never be completely eliminated.

A copy of the consent form that you sign to enter the study may be included in your health record/hospital chart.

WHAT IS THE COST TO PARTICIPANTS?

Participation in this study will not involve any additional costs to you or your private health care insurance.

ARE STUDY PARTICIPANTS PAID TO BE IN THIS STUDY?

You will not be paid for taking part in this study.

WHAT ARE THE RIGHTS OF PARTICIPANTS IN A RESEARCH STUDY?

You will be told, in a timely manner, about new information that may be relevant to your willingness to stay in this study.

You have the right to be informed of the results of this study once the entire study is complete. If you would like to be informed of the results of this study, please let the study doctor know.

Your rights to privacy are legally protected by federal and provincial laws that require safeguards to ensure that your privacy is respected.

By signing this form, you do not give up any of your legal rights against the researcher/study doctor, sponsor or involved institutions for compensation, nor does this form relieve the researcher/study doctor, sponsor or their agents of their legal and professional responsibilities.

You will be given a copy of this signed and dated consent form prior to participating in this study.

WHOM DO PARTICIPANTS CONTACT FOR QUESTIONS?

If you have questions about taking part in this study, or if you suffer a research-related injury, you can talk to your study doctor, or the doctor who oversees the study at this institution. That person is:

_____ Dr. Robert MacRae _____

Principal Investigator Name: Dr. Robert MacRae Telephone 613-737-7700 ext. 70205

If you have questions about your rights as a participant or about ethical issues related to this study, you can talk to someone who is not involved in the study at all. Please contact The Ottawa Health Science Network Research Ethics Board, Chairperson at 613-798-5555 extension 16719.



The Ottawa Hospital | L'Hôpital d'Ottawa



The Ottawa Hospital | L'Hôpital d'Ottawa
RESEARCH INSTITUTE
INSTITUT DE RECHERCHE



UNIVERSITY OF OTTAWA
HEART INSTITUTE
INSTITUT DE CARDIOLOGIE
DE L'UNIVERSITÉ D'OTTAWA

Study Title Use of RADPOS system for 4D Monte Carlo dose calculations for lung patients

SIGNATURES

- All my questions have been answered,
- I understand the information within this informed consent form,
- I allow access to medical records and related personal health information as explained in this consent form,
- I do not give up any of my legal rights by signing this consent form,
- I agree to take part in this study.

Signature of Participant

Printed Name

Date

Signature of Person Conducting
the Consent Discussion

Printed Name and Role

Date



The Ottawa Hospital
L'Hôpital d'Ottawa



The Ottawa Hospital
L'Hôpital d'Ottawa
RESEARCH INSTITUTE
INSTITUT DE RECHERCHE



UNIVERSITY OF OTTAWA
HEART INSTITUTE
INSTITUT DE CARDIOLOGIE
DE L'UNIVERSITÉ D'OTTAWA

Study Title: Use of RADPOS system for 4D Monte Carlo dose calculations for lung patients

Participant Assistance

Complete the following declaration only if the participant is unable to read:

- The consent form was read to the participant. The person signing below attests that the study as set out in this form was accurately explained to the participant and any questions have been answered.

Signature of Impartial Witness

Printed Name

Date

Relationship to Participant

Document version: March 19, 2019



The Ottawa Hospital | L'Hôpital d'Ottawa



The Ottawa Hospital | L'Hôpital d'Ottawa
RESEARCH INSTITUTE INSTITUT DE RECHERCHE



UNIVERSITY OF OTTAWA
HEART INSTITUTE
INSTITUT DE CARDIOLOGIE
DE L'UNIVERSITÉ D'OTTAWA

Complete the following declaration only if the participant has limited proficiency in the language in which the consent form is written and interpretation was provided as follows:

- The person signing below acted as an interpreter, and attests that this study as set out in the consent form is accurately sight translated and/or interpreted, and that interpretation was provided on questions, responses and in additional discussion arising from this process.

Signature of Interpreter

Printed Name

Date

Signature of Person Conducting
the Consent Discussion

Printed Name and Role

Date

Document version: March 19, 2019

Bibliography

1. Brenner DR, Weir HK, Demers AA, et al. Projected estimates of cancer in Canada in 2020. *Cmaj.* 2020;192(9):E199-E205.
2. Canadian Cancer Statistics Advisory Committee. *Canadian Cancer Statistics 2019.*; 2019.
3. Committee CCSA. *Canadian Cancer Statistics: A 2020 Special Report on Lung Cancer.*; 2020.
4. Galvin JM, De Neve W. Intensity Modulating and Other Radiation Therapy Devices for Dose Painting. *J Clin Oncol.* 2007;25(8):924-930.
5. Bedford JL, Thomas MDR, Smyth G. Beam modeling and VMAT performance with the Agility 160-leaf multileaf collimator. *J Appl Clin Med Phys.* 2013;14(2):172.
6. ICRU. *Prescribing, Recording and Reporting Photon Beam Therapy-ICRU Report 50.*; 1993.
7. ICRU. *Prescribing, Recording and Reporting Photon Beam Therapy-ICRU Report 62 (Supplement to ICRU Report 50).*; 1999.
8. Armstrong J, Burman C, Leibel S, et al. Three-dimensional conformal radiation therapy may improve the therapeutic ratio of high dose radiation therapy for lung cancer. *Int J Radiat Oncol Biol Phys.* 1993;26:685-689.
9. Rauschenbach BM, Mackowiak L, Malhotra HK. A dosimetric comparison of three-dimensional conformal radiotherapy, volumetric-modulated arc therapy, and dynamic conformal arc therapy in the treatment of non-small cell lung cancer using stereotactic body radiotherapy. *J Appl Clin Med Phys.* 2014;15(5):147-161.

10. Bortfeld T. IMRT: a review and preview . *Phys Med Biol.* 2006;51:363.
11. Teoh M, Clark CH, Wood K, Whitaker S, Nisbet A. Volumetric modulated arc therapy: a review of current literature and clinical use in practice. *Br J Radiol.* 2011;84:967-996.
12. Shepard DM, Earl MA, Li XA, Naqvi S, Yu C. Direct aperture optimization: A turnkey solution for step-and-shoot IMRT. *Med Phys.* 2002;29(6):1007-1018.
13. Otto K. Volumetric modulated arc therapy: IMRT in a single gantry arc; Volumetric modulated arc therapy: IMRT in a single gantry arc. *Med Phys.* 2007;35(1):310-317.
14. Storey CL, Hanna GG, Greystoke A. Practical implications to contemplate when considering radical therapy for stage III non-small-cell lung cancer. *Br J Cancer.* 2020;123:28-35.
15. Keall PJ, Mageras GS, Balter JM, et al. The management of respiratory motion in radiation oncology report of AAPM Task Group 76. *Med Phys.* 2006;33(10):3874-3900.
16. Cherpak AJ, Cygler JE, Andrusyk S, Pantarotto J, MacRae R, Perry G. Clinical use of a novel in vivo 4D monitoring system for simultaneous patient motion and dose measurements. *Radiother Oncol.* 2012;102(2):290-296.
17. Bortfeld T, Joviarski K, Goitein Michael, Kung J, Jiang SB. Effects of intra-fraction motion on IMRT dose delivery: statistical analysis and simulation. *Phys Med Biol.* 2002;47:2220.
18. Shirato H, Seppenwoolde Y, Kitamura K, Onimura R, Shimizu S. Intrafractional Tumor Motion: Lung and Liver. *Semin Radiat Oncol.* 2004;14(1).

19. Davies SC, Hill AL, Holmes RB, Halliwell M, Jackson PC. Ultrasound quantitation of respiratory organ motion in the upper abdomen. *Br J Radiol.* 1994;67(803):1096-1102.
20. Yoganathan SA, Das KJM, Agarwal A, Kumar S. Magnitude, Impact, and Management of Respiration-induced Target Motion in Radiotherapy Treatment: A Comprehensive Review. *J Med Phys.* 2017;42(3):101.
21. Seppenwoolde Y, Shirato H, Kitamura K, et al. Precise and real-time measurement of 3D tumor motion in lung due to breathing and heartbeat, measured during radiotherapy. *Int J Radiat Oncol.* 2002;53(4):822-834.
22. Hugo GD, Yan D, Liang J. Population and patient-specific target margins for 4D adaptive radiotherapy to account for intra- and inter-fraction variation in lung tumour position. *Phys Med Biol.* 2007;52(1):257-274.
23. Henry Yu Z, Lin SH, Balter P, Zhang L, Dong L. A comparison of tumor motion characteristics between early stage and locally advanced stage lung cancers. *Radiother Oncol.* 2012;104:33-38.
24. Hugo G, Vargas C, Liang J, Kestin L, Wong JW, Yan D. Changes in the respiratory pattern during radiotherapy for cancer in the lung. *Radiat Oncol.* 2006;78:326-331.
25. Juhler Nøttrup T, Sofia Korreman S, Navrsted Pedersen A, et al. Intra-and interfraction breathing variations during curative radiotherapy for lung cancer. *Radiother Oncol.* 2007;84:40-48.
26. Gierga DP, Brewer J, Sharp GC, Betke M, Willett CG, Chen GTY. The correlation between internal and external markers for abdominal tumors:

- Implications for respiratory gating. *Int J Radiat Oncol Biol Phys.* 2005;61(5):1551-1558.
27. Koch N, Liu HH, Starkschall G, et al. Evaluation of internal lung motion for respiratory-gated radiotherapy using MRI: Part I—correlating internal lung motion with skin fiducial motion. *Int J Radiat Oncol.* 2004;60(5):1459-1472.
 28. Chi PCM, Balter P, Luo D, Mohan R, Pan T. Relation of external surface to internal tumor motion studied with cine CT. *Med Phys.* 2006;33(9):3116-3123.
 29. Hoisak JDP, Sixel KE, Tirona R, Cheung PCF, Pignol JP. Correlation of lung tumor motion with external surrogate indicators of respiration. *Int J Radiat Oncol Biol Phys.* 2004;60(4):1298-1306.
 30. Vedam SS, Kini VR, Keall PJ, Ramakrishnan V, Mostafavi H, Mohan R. Quantifying the predictability of diaphragm motion during respiration with a noninvasive external marker. *Med Phys.* 2003;30(4):505-513.
 31. Tsunashima Y, Sakae T, Shioyama Y, et al. Correlation between the respiratory waveform measured using a respiratory sensor and 3D tumor motion in gated radiotherapy. *Int J Radiat Oncol.* 2004;60(3):951-958.
 32. Lee D, Greer PB, Paganelli C, Ludbrook JJ, Kim T, Keall P. Audiovisual biofeedback improves the correlation between internal/external surrogate motion and lung tumor motion: *Med Phys.* 2018;45(3):1009-1017.
 33. Chen QSS, Weinhous MS, Deibel FC, Ciezki JP, Macklis RM. Fluoroscopic study of tumor motion due to breathing: Facilitating precise radiation therapy for lung cancer patients. *Med Phys.* 2001;28(9):1850-1856.

34. Yan H, Zhu G, Yang J, et al. Investigation of the location effect of external markers in respiratory-gated radiotherapy. *J Appl Clin Med Phys.* 2008;9(2):57.
35. Liu HH, Koch N, Starkschall G, et al. Evaluation of internal lung motion for respiratory-gated radiotherapy using MRI: Part II-margin reduction of internal target volume. *Int J Radiat Oncol Biol Phys.* 2004;60(5):1473-1483.
36. Shirato H, Harada T, Harabayashi T, et al. Feasibility of insertion/implantation of 2.0-mm-diameter gold internal fiducial markers for precise setup and real-time tumor tracking in radiotherapy. *Int J Radiat Oncol.* 2003;56(1):240-247.
37. Willoughby TR, Forbes AR, Buchholz D, et al. Evaluation of an infrared camera and X-ray system using implanted fiducials in patients with lung tumors for gated radiation therapy. *Int J Radiat Oncol.* 2006;66(2):568-575.
38. Imura M, Yamazaki K, Shirato H, et al. Insertion and fixation of fiducial markers for setup and tracking of lung tumors in radiotherapy. *Int J Radiat Oncol Biol Phys.* 2005;63(5).
39. Nelson C, Starkschall G, Balter P, Morice RC, Stevens CW, Chang JY. Assessment of lung tumor motion and setup uncertainties using implanted fiducials. *Int J Radiat Oncol Biol Phys.* 2007;67(3):915-923.
40. Shirato H, Shimizu S, Kunieda T, et al. Physical aspects of a real-time tumor-tracking system for gated radiotherapy. *Int J Radiat Oncol Biol Phys.* 2000;48(4):1187-1195.
41. Harada T, Shirato H, Ogura S, et al. Real-time tumor-tracking radiation therapy for lung carcinoma by the aid of insertion of a gold marker using bronchofiberscopy. *Cancer.* 2002;95(8):1720-1727.

42. Roman NO, Shepherd W, Mukhopadhyay N, Hugo GD, Weiss E. Clinical Investigation: Thoracic Cancer Interfractional Positional Variability of Fiducial Markers and Primary Tumors in Locally Advanced Non-Small-Cell Lung Cancer During Audiovisual Biofeedback Radiotherapy Radiation Oncology. *Radiat Oncol Biol.* 2012;83(5):1566-1572.
43. Kupelian PA, Forbes A, Willoughby TR, et al. Implantation and Stability of Metallic Fiducials Within Pulmonary Lesions. *Int J Radiat Oncol.* 2007;69(3):777-785.
44. Siva S, Pham D, Gill S, et al. An analysis of respiratory induced kidney motion on four-dimensional computed tomography and its implications for stereotactic kidney radiotherapy. *Radiat Oncol.* 2013;8.
45. Glide-Hurst CK, Smith MS, Ajlouni M, Chetty IJ. Evaluation of two synchronized external surrogates for 4D CT sorting. *J Appl Clin Med Phys.* 2013;14(6):117-132.
46. Philips. Respiratory Motion Management for CT [White Paper]. 2013.
47. Wong JW, Sharpe MB, Jaffray DA, et al. The use of active breathing control (ABC) to reduce margin for breathing motion. *Int J Radiat Oncol Biol Phys.* 1999;44(4):911-919.
48. Rietzel E, Chen GTY, Choi NC, Willet CG. Four-dimensional image-based treatment planning: Target volume segmentation and dose calculation in the presence of respiratory motion. *Int J Radiat Oncol Biol Phys.* 2005;61(5):1535-1550.

49. Glide-Hurst CK, Chetty IJ. Improving radiotherapy planning, delivery accuracy, and normal tissue sparing using cutting edge technologies. *J Thorac Dis.* 2014;6(4):303.
50. Bert C, Metheany KG, Doppke K, Chen GTY. A phantom evaluation of a stereovision surface imaging system for radiotherapy patient setup. *Med Phys.* 2005;32(9):2753-2762.
51. Brahme A, Nyman P, Skatt B. 4D laser camera for accurate patient positioning, collision avoidance, image fusion and adaptive approaches during diagnostic and therapeutic procedures. *Med Phys.* 2008;35(5):1670-1681.
52. Franz AM, Schmitt D, Seitel A, et al. Standardized accuracy assessment of the calypso wireless transponder tracking system. *Phys Med Biol Phys Med Biol.* 2014;59:6797-6810.
53. Belanger M, Saleh Z, Volpe T, et al. Validation of the Calypso Surface Beacon Transponder; Validation of the Calypso Surface Beacon Transponder. *J Appl Clin Med Phys.* 2016;17(4).
54. Shah AP, Kupelian PA, Waghorn BJ, et al. Clinical Investigation: Thoracic Cancer Real-Time Tumor Tracking in the Lung Using an Electromagnetic Tracking System Radiation Oncology. *Int J Radiat Oncol Biol Phys.* 2013;86(3):477-483.
55. Dobelbower MC, Popple RA, Minnich DJ, et al. Anchored Transponder Guided Lung Radiation Therapy. *Pract Radiat Oncol.* 2020;10:e37-e44.

56. Jaccard M, Champion A, Dubouloz A, et al. Clinical experience with lung-specific electromagnetic transponders for real-time tumor tracking in lung stereotactic body radiotherapy. *Phys Imaging Radiat Oncol.* 2019;12:30.
57. Cherpak A, Ding W, Hallil A, Cygler JE. Evaluation of a novel 4D in vivo dosimetry system. *Med Phys.* 2009;36:1672-1679.
58. Hummel JB, Bax MR, Figl ML, et al. Design and application of an assessment protocol for electromagnetic tracking systems. *Med Phys.* 2005;32(7):2371-2379.
59. Rietzel E, Pan T, Chen GTY. Four-dimensional computed tomography: Image formation and clinical protocol. *Med Phys.* 2005;32(4):874-889.
60. Philips. Respiratory motion management for CT. Published online 2013.
61. Han K, Basran PS, Cheung P. Comparison of Helical and Average Computed Tomography for Stereotactic Body Radiation Treatment Planning and Normal Tissue Contouring in Lung Cancer. *Clin Oncol.* 2010;22(10):862-867.
62. Bradley JD, Nofal AN, El Naqa IM, et al. Comparison of helical, maximum intensity projection (MIP), and averaged intensity (AI) 4D CT imaging for stereotactic body radiation therapy (SBRT) planning in lung cancer. *Radiother Oncol.* 2006;81:264-268.
63. M Underberg RW, Lagerwaard FJ, Slotman BJ, Cuijpers JP, Senan S. Use of maximum intensity projections (MIP) for target volume generation in 4DCT scans for lung cancer. *Int J Radiati Oncol Biol Phys.* 2005;63(1):253-260.
64. Huang L, Park K, Boike T, et al. A study on the dosimetric accuracy of treatment planning for stereotactic body radiation therapy of lung cancer using average and maximum intensity projection images. *Radiother Oncol.* 2010;96(1):48-54.

65. Admiraal MA, Schuring D, Hurkmans CW. Dose calculations accounting for breathing motion in stereotactic lung radiotherapy based on 4D-CT and the internal target volume. *Radiother Oncol.* 2008;86(1):55-60.
66. Khamfongkhrua C, Thongsawad S, Tannanonta C, Chamchod S. Comparison of CT images with average intensity projection, free breathing, and mid-ventilation for dose calculation in lung cancer. *J Appl Clin Med Phys.* 2017;18(2):26-36.
67. Wolthaus JWH, Schneider C, Sonke JJ, et al. Mid-ventilation CT scan construction from four-dimensional respiration-correlated CT scans for radiotherapy planning of lung cancer patients. *Int J Radiat Oncol.* 2006;65(5):1560-1571.
68. Shimizu S, Shirato H, Ogura S, et al. Detection of lung tumor movement in real-time tumor-tracking radiotherapy. *Int J Radiat Oncol Biol Phys.* 2001;51(2):304-310.
69. Mageras GS, Yorke E. Deep Inspiration Breath Hold and Respiratory Gating Strategies for Reducing Organ Motion in Radiation Treatment. *Radiat Oncol.* 2004;14(1):65-75.
70. Keall P, Vedam S, George R, et al. The clinical implementation of respiratory-gated intensity-modulated radiotherapy. *Med Dosim.* 2006;31(2):152-162.
71. Berson AM, Emery R, Rodriguez L, et al. Clinical experience using respiratory gated radiation therapy: Comparison of free-breathing and breath-hold techniques. *Int J Radiat Oncol.* 2004;60(2):419-426.

72. Hanley J, Debois MM, Mah D, et al. Deep inspiration breath-hold technique for lung tumors: the potential value of target immobilization and reduced lung density in dose escalation. *Int J Radiat Oncol Biol Phys.* 1999;45(3):603-611.
73. Rosenzweig KE, Hanley J, Mah D, et al. The deep inspiration breath-hold technique in the treatment of inoperable non-small-cell lung cancer. *Int J Radiat Oncol Biol Phys.* 2000;48(1):81-87.
74. Mah D, Hanley J, Rosenzweig KE, et al. Technical aspects of the deep inspiration breath-hold technique in the treatment of thoracic cancer. *Int J Radiat Oncol Biol Phys.* 2000;48(4):1175-1185.
75. Cheung PC., Sixel KE, Tirona R, Ung YC. Reproducibility of lung tumor position and reduction of lung mass within the planning target volume using active breathing control (ABC). *Int J Radiat Oncol Biol Phys.* 2003;57(5):1437-1442.
76. Murray B, Forster K, Timmerman R. Frame-based immobilization and targeting for stereotactic body radiation therapy. *Med Dosim.* 2007;32(2):86-91.
77. Han K, Cheung P, Basran PS, Poon I, Yeung L, Lochray F. A comparison of two immobilization systems for stereotactic body radiation therapy of lung tumors. *Radiother Oncol.* 2010;95(1):103-108.
78. Negoro Y, Nagata Y, Aoki T, et al. The effectiveness of an immobilization device in conformal radiotherapy for lung tumor: reduction of respiratory tumor movement and evaluation of the daily setup accuracy. *Int J Radiat Oncol Biol Phys.* 2001;50(4):889-898.

79. Whyte RI, Crownover R, Murphy MJ, et al. Stereotactic Radiosurgery for Lung Tumors: Preliminary Report of a Phase I Trial. *Ann Thorac Surg.* 2003;75(4):1097-1101.
80. Seppenwoolde Y, Berbeco RI, Nishioka S, Shirato H, Heijmen B. Accuracy of tumor motion compensation algorithm from a robotic respiratory tracking system: A simulation study. *Med Phys.* 2007;34(7):2774-2784.
81. Schweikard A, Glosser G, Bodduluri M, Murphy MJ, Adler JR. Robotic Motion Compensation for Respiratory Movement during Radiosurgery. *Comput Aided Surg.* 2000;5(4):263-277.
82. Jin JY, Yin FF, Tenn SE, Medin PM, Solberg TD. Use of the BrainLAB ExacTrac X-Ray 6D System in Image-Guided Radiotherapy. *Med Dosim.* 2008;33(2):124-134.
83. Mukumoto N, Nakamura M, Sawada A, et al. Positional accuracy of novel x-ray-image-based dynamic tumor-tracking irradiation using a gimbaled MV x-ray head of a Vero4DRT (MHI-TM2000). *Med Phys.* 2012;39(10):6287-6296.
84. Kamino Y, Takayama K, Kokubo M, et al. Development of a four-dimensional image-guided radiotherapy system with a gimbaled X-ray head. *Int J Radiat Oncol Biol Phys.* 2006;66(1):271-278.
85. Smilowitz JB, Das IJ, Feygelman V, et al. AAPM Medical Physics Practice Guideline 5.a.: Commissioning and QA of Treatment Planning Dose Calculations — Megavoltage Photon and Electron Beams. *J Appl Clin Med Phys.* 2015;16(5):14-34.

86. Chetty IJ, Curran B, Cygler JE, et al. Report of the AAPM Task Group No. 105: Issues associated with clinical implementation of Monte Carlo-based photon and electron external beam treatment planning. *Med Phys.* 2007;34(12):4818-4853.
87. Gholampourkashi S, Cygler JE, Belec J, et al. Monte Carlo and analytic modeling of an Elekta Infinity linac with Agility MLC: Investigating the significance of accurate model parameters for small radiation fields. *Agility, analytic model, Elekta, Monaco, Monte Carlo, virtual source. J Appl Clin Med Phys.* 2019;20(1):55-67.
88. Esch A Van, Tillikainen L, Pyykkonen J, et al. Testing of the analytical anisotropic algorithm for photon dose calculation. *Med Phys.* 2006;33(11):4130-4148.
89. Fippel M, Haryanto F, Dohm O, Nüsslin F, Kriesen S. A virtual photon energy fluence model for Monte Carlo dose calculation. *Med Phys.* 2003;30(3):301-311.
90. Ahnesjo A, Aspradakis MM. Dose calculations for external photon beams in radiotherapy. *Phys Med Biol.* 1999;44:99-155.
91. Ahnesjö A, Andreo P, Brahme A. Calculation and Application of Point Spread Functions for Treatment Planning with High Energy Photon Beams. *Acta Oncol (Madr).* 1987;26(1):49-56.
92. De Martino F, Clemente S, Graeff C, Palma G, Celli L. Dose Calculation Algorithms for External Radiation Therapy: An Overview for Practitioners. *Appl Sci.* 2021;11(15):6806.
93. Ahnesjö A. Collapsed cone convolution of radiant energy for photon dose calculation in heterogeneous media. *Med Phys.* 1989;16(4):577-592.

94. Ahnesjö A, Saxner M, Trepp A. A pencil beam model for photon dose calculation. *Med Phys*. 1992;19(2):263-273.
95. Crammer-Sargison G, Beckham WA, Popescu IA. Modelling an extreme water-lung interface using a single pencil beam algorithm and the Monte Carlo method. *Phys Med Biol*. 2004;49:1567.
96. Schuring D, Hurkmans CW. Developing and evaluating stereotactic lung RT trials: what we should know about the influence of inhomogeneity corrections on dose. *Radiat Oncol*. 2008;3(1):21.
97. Schwarz M, Cattaneo GM, Marrazzo L. Geometrical and dosimetrical uncertainties in hypofractionated radiotherapy of the lung: A review. *Phys Medica*. 2017;36:126-139.
98. Chen H, Lohr F, Fritz P, et al. Stereotactic, single-dose irradiation of lung tumors: a comparison of absolute dose and dose distribution between pencil beam and monte carlo algorithms based on actual patient CT scans. *Int J Radiat Oncol Biol Phys*. 2010;79(3):955-963.
99. Vanderstraeten B, Reynaert N, Paelinck L, et al. Accuracy of patient dose calculation for lung IMRT: A comparison of Monte Carlo, convolution/superposition, and pencil beam computations. *Med Phys*. 2006;33(9):3149-3158.
100. Haedinger U, Krieger T, Flentje M, Wulf J. Influence of calculation model on dose distribution in stereotactic radiotherapy for pulmonary targets. *Int J Radiat Oncol*. 2005;61(1):239-249.

101. Bedford J. Calculation of absorbed dose in radiotherapy by solution of the linear Boltzmann transport equations. *Phys Med Biol* . 2019;64.
102. Kawrakow I. Accurate condensed history Monte Carlo simulation of electron transport. I. EGSnrc, the new EGS4 version. *Med Phys*. 2000;27(3):485-498.
103. Kawrakow I, Mainegra-Hing E, Rogers DWO, Tessier F, Walters BRB. *The EGSnrc Code System: Monte Carlo Simulation of Electron and Photon Transport.*; 2021.
104. Kawrakow I, Fippel M, Friedrich K. 3D electron dose calculation using a Voxel based Monte Carlo algorithm (VMC). *Med Phys*. 1996;23(4):445-457.
105. Fippel M. Fast Monte Carlo dose calculation for photon beams based on the VMC electron algorithm. *Med Phys*. 1999;26(8):1466-1475.
106. Elekta. Monaco Dose Calculation Technical Reference. Published online 2014.
107. Kawrakow I, Rogers D, Mainegra-Hing E, Tessier F, Townson R, Walters BRB. EGSnrc toolkit for Monte Carlo simulation of ionizing radiation transport (2002).
108. Baró J, Sempau J, Fernández-Varea JM, Salvat F. PENELOPE: An algorithm for Monte Carlo simulation of the penetration and energy loss of electrons and positrons in matter. *Nucl Instruments Methods Phys Res Sect B Beam Interact with Mater Atoms*. 1995;100(1):31-46.
109. Agostinelli S, Allison J, Amako K, et al. GEANT4 - A simulation toolkit. *Nucl Instruments Methods Phys Res*. 2003;506(3):250-303.
110. Los Alamos Laboratory. *MCNP- A General Monte Carlo N-Particle Transport Code, Version 5.*; 2003.

111. Rogers DWO, Faddegon BA, Ding GX, Ma CM, We J, Mackie TR. BEAM: A Monte Carlo code to simulate radiotherapy treatment units. *Med Phys.* 1995;22(5):503-524.
112. Walters B, Kawrakow I, Rogers DWO. *DOSXYZnrc Users Manual*. NRCC Report PIRS-794revB; 2020.
113. Kawrakow I, Walters BRB. Efficient photon beam dose calculations using DOSXYZnrc with BEAMnrc. *Med Phys.* 2006;33(8):3046-3056.
114. Lobo J, Popescu IA. Two new DOSXYZnrc sources for 4D Monte Carlo simulations of continuously variable beam configurations, with applications to RapidArc, VMAT, TomoTherapy and CyberKnife. *Phys Med Biol.* 2010;55(16):4431-4443.
115. Jelen U, Sohn M, Alber M. A finite size pencil beam for IMRT dose optimization. *Phys Med Biol.* 2005;50:1747.
116. Bortfeld T, Jiang SB, Rietzel E. Effects of Motion on the Total Dose Distribution. *Semin Radiat Oncol.* 2004;14(1):41-51.
117. Seco J, Verhaegen F, eds. *Monte Carlo Techniques in Radiation Therapy*. 1st ed. Taylor & Francis Group
118. Keall PJ, Siebers J V, Joshi S, Mohan R. Monte Carlo as a four-dimensional radiotherapy treatment-planning tool to account for respiratory motion. *Phys Med Biol.* 2004;49(16):3639-3648.
119. Rosu M, Balter JM, Chetty IJ, et al. How extensive of a 4D dataset is needed to estimate cumulative dose distribution plan evaluation metrics in conformal lung therapy? *Med Phys.* 2007;34(1):233-245.

120. Guckenberger M, Wilbert J, Krieger T, et al. Four-dimensional treatment planning for stereotactic body radiotherapy. *Int J Radiat Oncol Biol Phys.* 2007;69(1):276-285.
121. Flampouri S, Jiang SB, Sharp GC, Wolfgang J, Patel AA, Choi NC. Estimation of the delivered patient dose in lung IMRT treatment based on deformable registration of 4D-CT data and Monte Carlo simulations. *Phys Med Biol.* 2006;51(11):2763-2779.
122. Brock KK, McShan DL, Haken RK Ten, Hollister SJ, Dawson LA, Balter JM. Inclusion of organ deformation in dose calculations. *Med Phys.* 2003;30(3):290-295.
123. Chetty IJ, Rosu-Bubulac M. Deformable Registration for Dose Accumulation. *Semin Radiat Oncol.* 2019;29:198-208.
124. Rosu M, Chetty IJ, Balter JM, Kessler ML, McShan DL, Haken RK Ten. Dose reconstruction in deforming lung anatomy: Dose grid size effects and clinical implications. *Med Phys.* 2005;32(8):2487-2495.
125. Schaly B, Kempe JA, Bauman GS, Battista JJ, Van Dyk J. Tracking the dose distribution in radiation therapy by accounting for variable anatomy. *Med Biol Phys Med Biol.* 2004;49:791-805.
126. Heath E, Seuntjens J. A direct voxel tracking method for four-dimensional Monte Carlo dose calculations in deforming anatomy. *Med Phys.* 2006;33(2):434-445.
127. Zhong H, Siebers J V. Monte Carlo dose mapping on deforming anatomy. *Phys Med Biol.* 2009;54(19):5815-5830.

128. Siebers J V, Zhong H. An energy transfer method for 4D Monte Carlo dose calculation. *Med Phys*. 2008;35(9).
129. Heath E, Tessier F, Kawrakow I. Investigation of voxel warping and energy mapping approaches for fast 4D Monte Carlo dose calculations in deformed geometries using VMC++. *Med Biol Phys Med Biol*. 2011;56:5187-5202.
130. Litzenberg DW, Hadley SW, Tyagi N, Balter JM, Ten Haken RK, Chetty IJ. Synchronized dynamic dose reconstruction. *Med Phys*. 2007;34(August 2006):91-102.
131. Belec J, Clark BG. Monte Carlo calculation of VMAT and helical tomotherapy dose distributions for lung stereotactic treatments with intra-fraction motion. *Med Biol Phys Med Biol*. 2013;58:2807-2821.
132. Belec J, Ploquin N, Russa DJ La, Clark BG. Position-probability-sampled Monte Carlo calculation of VMAT, 3DCRT, step-shoot IMRT, and helical tomotherapy dose distributions using BEAMnrc/DOSXYZnrc. *Med Phys*. 2011;38(2):948-960.
133. Poulsen PR, Schmidt ML, Keall P, Worm ES, Fledelius W, Hoffmann L. A method of dose reconstruction for moving targets compatible with dynamic treatments. *Med Phys*. 2012;39(10):6237-6246.
134. Chan MKH, Kwong DLW, Ng SCY, Tam EKW, Tong ASM. Investigation of four-dimensional (4D) Monte Carlo dose calculation in real-time tumor tracking stereotactic body radiotherapy for lung cancers. *Med Phys*. 2012;39(9):5479-5487.
135. Rao M, Wu J, Cao D, et al. Impact of Breathing Motion in Lung Stereotactic Body Radiotherapy Treatment Using Image-Modulated Radiotherapy and

- Volumetric Modulated Arc Therapy Radiation Oncology. *Int J Radiat Oncol Biol Phys.* 2012;83(2):251-256.
136. Zou W, Yin L, Shen J, et al. Dynamic simulation of motion effects in IMAT lung SBRT. *Radiat Oncol.* 2014;9:1-9.
137. Freislederer P, von Münchow A, Kamp F, et al. Comparison of planned dose on different CT image sets to four-dimensional Monte Carlo dose recalculation using the patient's actual breathing trace for lung stereotactic body radiation therapy. *Med Phys.* 2019;46(7):3268-3277.
138. Heath E, Badragan I, Popescu I. TU-G-BRA-01: 4D Monte Carlo Simulations of Beam and Patient Motion Using EGSnrc/BEAMnrc. In: *Fifty-Fourth Annual Meeting of the American Association of Physicists in Medicine*. Vol 39. John Wiley & Sons, Ltd; 2012:3921-3921.
139. Gholampourkashi S, Vujicic M, Belec J, Cygler JE, Heath E. Experimental verification of 4D Monte Carlo simulations of dose delivery to a moving anatomy: *Med Phys.* 2017;44(1):299-310.
140. Gholampourkashi S, Cygler JE, Lavigne B, Heath E. Development of a deformable phantom for experimental verification of 4D Monte Carlo simulations in a deforming anatomy. *Phys Medica.* 2018;51(May):81-90.
141. Gholampourkashi S. *Experimental verification of 4D Monte Carlo simulations of dose delivery to a moving anatomy*. PhD thesis. Carleton University. 2018.
142. Kadoya N, Fujita Y, Katsuta Y, et al. Evaluation of various deformable image registration algorithms for thoracic images. *J Radiat Res.* 2014;55(1):175-182.

143. Lawson JD, Schreibmann E, Jani AB, Fox T. Quantitative evaluation of a cone-beam computed tomography-planning computed tomography deformable image registration method for adaptive radiation therapy. *J Appl Clin Med Phys.* 2007;8(4):96-113.
144. Heath E, Collins DL, Keall PJ, Dong L, Seuntjens J. Quantification of accuracy of the automated nonlinear image matching and anatomical labeling (ANIMAL) nonlinear registration algorithm for 4D CT images of lung. *Med Phys.* 2007;34(11):4409-4421.
145. Sutherland JG. *Monte Carlo dose calculations for breast and lung permanent implant brachytherapy*. PhD thesis. Carleton University. 2013.
146. White DR, Griffith R V, Wilson IJ. Photon, Electron, Proton and Neutron Interaction Data for Body Tissues-ICRU Report 46. *J Int Comm Radiat Units Meas.* 1992;24(1).
147. Zhan L, Jiang R, Osei EK. Beam coordinate transformations from DICOM to DOSXYZnrc. *Phys Med Biol.* 2012;57(24).
148. Chetty IJ, Curran B, Cygler JE, et al. Report of the AAPM Task Group No. 105: Issues associated with clinical implementation of Monte Carlo-based photon and electron external beam treatment planning. *Med Phys.* 2007;34(12):4818-4853.
149. Deasy JO, Blanco AI, Clark VH. CERR: A computational environment for radiotherapy research. *Med Phys.* 2003;30(5):979-985.
150. Takao S, Miyamoto N, Matsuura T, et al. Intrafractional Baseline Shift or Drift of Lung Tumor Motion During Gated Radiation Therapy With a Real-Time Tumor-Tracking System Radiation Oncology. *Radiat Oncol Biol.* 2016;94(1):172-180.

151. Low DA, Harms WB, Mutic S, Purdy JA. A technique for the quantitative evaluation of dose distributions. *Med Phys*. 1998;25(5):656-661.
152. Zhang Q, Pevsner A, Hertanto A, et al. A patient-specific respiratory model of anatomical motion for radiation treatment planning. *Med Phys*. 2007;34(12):4772-4781.
153. Hurwitz M, Williams CL, Mishra P, et al. Generation of fluoroscopic 3D images with a respiratory motion model based on an external surrogate signal. *Phys Med Biol*. 2015;60(2):521-535.
154. Fayad H, Pan T, Pradier O, Visvikis D. Patient specific respiratory motion modeling using a 3D patient's external surface. *Med Phys*. 2012;39(6):3386-3395.
155. Sonke JJ, Zijp L, Remeijer P, Van Herk M. Respiratory correlated cone beam CT. *Med Phys*. 2005;32(4):1176-1186.
156. Thengumpallil S, Smith K, Monnin P, Bourhis J, Bochud F, Moeckli R. Difference in performance between 3D and 4D CBCT for lung imaging: a dose and image quality analysis. *J Appl Clin Med Phys*. 2016;17(6):97.
157. Yuasa Y, Shiinoki T, Onizuka R, Fujimoto K. Estimation of effective imaging dose and excess absolute risk of secondary cancer incidence for four-dimensional cone-beam computed tomography acquisition. *J Appl Clin Med Phys*. 2019;20(11):57.